

Structural and Mechanistic Studies of Nickel–Borate Thin-Film Oxygen Evolving Electrocatalysts

by

Daniel Kwabena Bediako
B.S. Chemistry, Calvin College, 2008

Submitted to the Department of Chemistry
in partial fulfillment of the requirements for the degree of

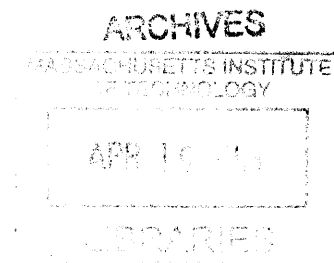
MASTER OF SCIENCE IN CHEMISTRY

at the

MASSACHUSETTS INSTITUTE OF TECHNOLOGY

February 2013

© Massachusetts Institute of Technology 2013. All rights reserved



Signature of Author: _____
Department of Chemistry
January 2013

Certified by: _____
Daniel G. Nocera
Henry Dreyfus Professor of Energy and Professor of Chemistry
Thesis Supervisor

Accepted by: _____
Robert W. Field
Haslam and Dewey Professor of Chemistry Chairman
Departmental Committee on Graduate Studies



*To Lisseth and my mom for their unwavering support
To my dad, a person full of of humility, selflessness, and compassion
May I endeavor to follow in his footsteps*



Structural and Mechanistic Studies of Nickel–Borate Thin-Film Oxygen Evolving Electrocatalysts

by

Daniel Kwabena Bediako

Submitted to the Department of Chemistry on January 18, 2013, in partial fulfillment of the requirements for the degree of Master of Science in Chemistry.

Abstract

Increases in global energy demand and rising levels of atmospheric carbon dioxide demand renewable alternatives to fossil fuels as the primary energy sources of the 21st century. Solar energy is by far the most abundant renewable energy resource, yet its widespread use has been hampered by a lack of suitable methods to store energy from sunlight in a cheap and efficient manner. Solar driven water splitting is a promising method of storing solar energy, but a critical bottleneck in developing efficient photoelectrochemical (PEC) water splitting systems lies in the kinetic sluggishness of the water splitting reactions, particularly the oxygen evolution reaction (OER).

In this thesis the structural and mechanistic underpinnings for the activity of a promising nickel-based oxygen evolving catalyst (OEC) are discussed. The catalyst is particularly attractive as a result of the simplicity of its preparation as a thin film from aqueous borate-buffered solutions of Ni²⁺. Electrochemical and *in situ* X-ray absorption near-edge structure (XANES) studies of this nickel-borate (Ni–B_i) catalyst indicate that upon initial electrodeposition, Ni centers in the film exist predominantly in the +3 oxidation state and the as-deposited material is largely inactive towards the OER. Catalytic activation is achieved by anodization of the as-deposited material in concentrated borate buffer, pH 9.2, a process which serves to oxidize the nickel centers to a mixed-valence Ni(III/IV) state. Extended X-ray absorption fine structure (EXAFS) spectroscopy studies indicate that Ni–B_i is comprised of nanometer-sized clusters of edge sharing NiO₆ octahedra. A structural transformation is observed during anodization that is akin to that observed in the β-NiOOH–γ-NiOOH transformation, challenging the long-held view that the phase that is the most catalytically active towards the OER is the all-Ni(III) β-NiOOH.

Electrokinetic studies indicate that the as-deposited Ni–B_i exhibits a Tafel slope close to $2.3 \times 2RT/F$, consistent with a turnover-limiting electron transfer (ET) from the geometrically distorted low-spin d⁷ Ni(III) state. Upon anodization to the mixed valence Ni(III/IV) state and elimination of geometric distortion, ET from the resting state becomes more facile resulting in a low Tafel slope of $2.3 \times RT/2F$, indicative of a rapid two-electron pre-equilibrium followed by a rate limiting chemical step, likely O₂ formation. Anodized Ni–B_i also exhibits an inverse third order dependence in proton activity and inverse first order dependence in borate anion.

This kinetically-relevant two-electron, three-proton proton-coupled electron transfer (PCET) equilibrium prior to rate limiting O₂ formation forms the mechanistic basis for the pH-dependent difference in activity between Ni–B_i and its cobalt-based analog, which contrarily mediates oxygen evolution via a kinetically-relevant one-electron, one-proton PCET transformation. The difference in catalytic O₂ evolution mechanism is a principal factor in the determination of the overall solar-to-fuels efficiency of PEC water splitting systems.

Thesis Supervisor: Daniel G. Nocera

Title: Henry Dreyfus Professor of Energy and Professor of Chemistry

Table of Contents

Title Page	1
Dedication	5
Abstract	7
Table of Contents	9
List of Figures	13
List of Tables	18
List of Abbreviations	20
Chapter 1 — Introduction	23
1.1 Challenges for Solar Water Splitting	24
1.2 The Centrality of Catalysis for Efficient Energy Storage	27
1.3 Electrodeposited Co- and Ni-based OECs	29
1.4 Scope of the Thesis	30
1.5 Concluding Remarks	31
1.6 References	32
Chapter 2 — Structure and Valency of Nickel–Borate Oxygen Evolving Catalysts	38
2.1 Introduction	39
2.2 Results	40
2.2.1 Catalyst Electrodeposition, Anodization and Electrochemistry.	40
2.2.2 <i>In situ</i> X-ray Absorption Spectroscopy	44

2.3 Discussion	53
2.3.1 Nickel Oxidation State Changes in Ni–B _i	54
2.3.2 Anodization-Induced Structural Changes in Ni–B _i .	55
2.4 Conclusion	57
2.5 Experimental Methods	58
2.6 References	63
Chapter 3 — Mechanistic Studies into Oxygen Evolution Mediated by Nickel–Borate Electrocatalyst Films	67
3.1 Introduction	68
3.2 Results	68
3.2.1 Catalyst Electrodeposition and Anodization	68
3.2.2 Tafel Slope Determination	69
3.2.3 Determination of Reaction Order in B _i	73
3.2.4 Determination of reaction order in H ⁺ activity	75
3.2.5 Tafel data in B _i -free electrolyte	79
3.3 Discussion	81
3.3.1 Steady-state Tafel data	81
3.3.2 OER of non-anodized Ni–B _i	82
3.3.3 OER of anodized Ni–B _i	84
3.3.4 OER in B _i -free electrolyte	90
3.3.5 Differences in mechanism and activity of Co–OECs and Ni–OECs	91

3.4 Conclusion	93
3.5 Experimental Methods	93
3.6 References	102
Chapter 4 — Interplay of oxygen evolution kinetics and photovoltaic power curves on the construction of artificial leaves	108
4.1 Introduction	109
4.2 Results	111
4.2.1 Catalyst Film Electrosynthesis	111
4.2.2 j - V Modeling of Buried-Junction Semiconductor–Catalyst Assemblies	112
4.3 Discussion	114
4.4 Conclusions	116
4.5 Experimental Methods	117
4.6 References	120
Biographical Note	124
Curriculum Vitae	126
Acknowledgements	129

List of Figures

- Figure 1.1.** Schematic band diagram of (a) dual band gap p/n-PEC and (b) double junction PV-PEC architectures depicting the thermodynamic potential separation for water splitting (dashed red lines) along with the quasi-Fermi level (dashed black lines) and band edge positions (solid black lines) at a water splitting current density, j . Productive carrier motion is illustrated with dark blue arrows. In (a), two possible e^-/h^+ recombination pathways are shown in grey: recombination in the bulk of the semiconductor, J_B , and recombination due to surface states, J_S . Both pathways may be affected by the presence of catalysts at the surface. In (b) the respective OER and HER activation overpotentials at j , η_{OER} and η_{HER} , are shown. Additional overpotentials arising due to contact or solution resistances are omitted for clarity. 25
- Figure 2.1.** Change in oxygen evolution current density as a function of anodization duration for a 1 mC/cm^2 Ni-B_i film on an FTO substrate, operated at (a) 1.1 V in 1.0 M KB_i pH 9.2 electrolyte, (b) 3.5 mA/cm² in 1.0 KB_i pH 9.2 electrolyte, and (c) 1.1 V in 0.1 M KB_i pH 9.2 electrolyte. 41
- Figure 2.2.** (a) Cyclic voltammograms (CVs) in 1.0 M KB_i (pH 9.2) electrolyte at 100 mV/s of 1 mC/cm^2 Ni-B_i catalyst films non-anodized (red —), 2 min (orange —), 5 min (yellow —), 15 min (green —), 30 min (light blue —), 2 h (blue —) and 4 h (black —) of anodization at 1.1 V (vs. NHE) in 1.0 M KB_i pH 9.2 electrolyte. The background CV of a blank FTO substrate is also displayed (grey * * *). The inset shows the ratio of the integrated charge under the cathodic wave observed in the first scan to lower potentials in the case of each film relative to that of the 4 h-anodized film. (b) Coulometric analysis of a fully anodized 1 mC/cm^2 Ni-B_i catalyst film. 42
- Figure 2.3.** (a) XANES spectra of model compounds: Ni(OH)₂ (blue — ■ — ■), β-NiOOH (green — ■ — ■), γ-NiOOH (red — ■ — ■), NiPPI (black ■ ■ ■ ■) and anodized Ni-B_i films at 0.4 (orange — —) and 1.0 V (dark blue —). (b) XANES spectra of a non-anodized Ni-B_i film poised at 1.0 V (purple ●●●), an anodized Ni-B_i film poised at 1.0 V (dark blue —), and β-NiOOH (green — ■ — ■). The inset shows the edge energy at half jump height as a function of applied potential for anodized (dark blue ●) and non-anodized (blue ▼) Ni-B_i. 45
- Figure 2.4.** (a) X-ray crystal structure of γ-NiOOH, showing nickel (green), oxygen (red) and sodium (blue) ions. Water molecules intercalated between the NiO₂ slabs been omitted for clarity. (b) Fragment of a general nickelate structure displaying the atoms (b, c, d, e) that lead to the relevant backscattering interactions from the absorbing atom, a. (c) k^3 -weighted EXAFS oscillations and (d) Fourier transforms of k -space oscillations for γ-NiOOH (red — —) and anodized Ni-B_i during catalysis at 1.05 V (blue —). 47
- Figure 2.5.** FT EXAFS spectra and k^3 -weighted EXAFS spectra (inset) of (a) an anodized Ni-B_i catalyst film maintained at 1.05 V (dark blue —) and 1.15 V (red — —) and (b) Ni(OH)₂ (blue — —) and an anodized Ni-B_i catalyst film held at 0.4 V (yellow —). 48
- Figure 2.6.** Fit (black — —) to EXAFS spectrum of γ-NiOOH (red —). The inset shows the corresponding k^3 -weighted oscillations. Fit parameters are indicated in Table 2.2. 48
- Figure 2.7.** Fit (black — —) to EXAFS spectrum of anodized Ni-B_i at 1.05 V (blue —). The inset shows the corresponding k^3 -weighted oscillations. Fit parameters are indicated in Table 2.3. 49

- Figure 2.8.** EXAFS FT spectra for non-anodized Ni-B_i poised at 1.0 V (blue —), anodized Ni-B_i poised at 1.05 V (dark blue — —), and β-NiOOH (green — ■ — ■). The inset shows the corresponding k^3 -weighted oscillations. 50
- Figure 2.9.** Models of the first and second shell scattering paths in (a) a structure where all Ni-O (lime green) and Ni-Ni (black) paths are equivalent, such as that found in γ-NiOOH and (b) a Jahn-Teller distorted structure where there exists two sets of non-equivalent Ni-O (lime green) and Ni-Ni (black) distances, such as that found in β-NiOOH or NaNiO₂. 52
- Figure 2.10.** Fit (black — —) to EXAFS spectrum of non-anodized Ni-B_i poised at 1.0 V (blue —). The inset shows the corresponding k^3 -weighted oscillations. Fit parameters are indicated in Table 2.6. 52
- Figure 2.11.** Lower-limit structural model for the average domain size of Ni-B_i. The Ni ions are shown in green, bridging oxo/hydroxo ligands are shown in red, and non-bridging oxygen ligands, which may include water, hydroxide, phosphate, or borate, are shown in pale green. 57
- Figure 3.1.** Tafel plots, $E = (E_{appl} - iR)$, $\eta = (E - E^\circ)$, for anodized catalyst films deposited onto FTO by passage of 1.0 (■), 0.40 (●), and 0.083 (▲) mC cm⁻² and operated in 0.5 M KB_i 1.75 M KNO₃ pH 9.2 electrolyte. Tafel slopes are 31, 32 and 29 mV/decade, respectively. 70
- Figure 3.2.** (a) Tafel plots, $E = (E_{applied} - iR)$, $\eta = (E - E^\circ)$, for a 1.0 mC cm⁻² anodized catalyst film deposited onto a Pt RDE and operated in 0.5 M KB_i 1.75 M KNO₃, pH 9.2 electrolyte at 2000 (▲), 600 (●), and 0 rpm with a magnetic stirrer as the sole source of solution convection (×). The Tafel slope of each plot is 28 mV/decade. (b) Tafel plots, $E = (E_{applied} - iR)$, $\eta = (E - E^\circ)$, for a 1.0 mC cm⁻² anodized catalyst film deposited onto FTO and operated in 0.5 M KB_i 1.75 M KNO₃, pH 9.2 electrolyte in decreasing (▲), followed immediately by increasing (●) order of changing potentials. Tafel slopes are 30 and 31 mV/decade respectively. 71
- Figure 3.3.** Open circuit potential, E_{OC} , and overpotential, $\eta_{OC} = (E_{OC} - E^\circ)$, transients for non-anodized (green — —) and anodized (dark blue —) 1.0 mC cm⁻² NiB_i films immediately following a 10 s bias at 1.1 V in 0.5 M KB_i 1.75 M KNO₃ pH 9.2 electrolyte. The red lines represent fits to eq 1. Tafel slopes are 100 before anodization and 33 mV/decade after anodization. The inset shows the corresponding Tafel plots determined from the E_{OC} transients by calculating $\log j$ at each time point using eq 3.2. 72
- Figure 3.4.** B_i concentration dependence of steady state catalytic current density at constant potential ($E = 1.04$ V (◆), 1.05 V (●), 1.06 V (■)) for an anodized catalyst film deposited onto a Pt RDE by passage of 1.0 mC cm⁻² and operated in B_i electrolyte, pH 9.2. Sufficient KNO₃ was added to maintain a constant total ionic strength of 2 M in all electrolytes. Koutecký-Levich analysis was used to extract activation-controlled current densities in weakly-buffered electrolyte, where the measured current was dependent on rotation rate. The experimental reaction orders (slopes of the red linear fits) in B_i are (from top to bottom) -0.95, -1.04 and -0.95. 73
- Figure 3.5.** (a) Tafel plots, $E = (E_{applied} - iR)$, $\eta = (E - E^\circ)$, for a 1.0 mC cm⁻² anodized catalyst film deposited onto FTO and operated in 1.0 (●), 0.5 (■), 0.2 (▲), and 0.1 (◊) M KB_i without any added supporting electrolyte. Tafel Slopes are 34, 35, 38, and 41 mV/decade, respectively. (b) Dependence of steady state electrode potential, $E = (E_{applied} - iR)$ and overpotential, $\eta = (E - E^\circ)$ for a 1.0 mC cm⁻² catalyst film operated at

- 0.4 mA cm⁻² in 0.1 M KB_i electrolyte with varying concentrations of KNO₃ as supporting electrolyte. 74
- Figure 3.6.** Steady state Koutecký–Levich plots of a 1.0 mC cm⁻² catalyst film prepared onto a Pt RDE and operated at $E = 1.04$ V at 2500, 1600, 900, and 625 rpm in 40 (●), 25 (■), 16 (▲), 10 (▼), and 6.3 (◐) mM KB_i electrolyte, with added KNO₃ to preserve an ionic strength of 2 M. 75
- Figure 3.7.** pH dependence of steady-state electrode potential at constant current density ($j_{anodic} = 10 \mu\text{A cm}^{-2}$) for an anodized 1.0 mC cm⁻² catalyst film on FTO operated in 0.1 M B_i 2 M KNO₃ electrolyte. Slopes equal -64 (—) and -96 (—) mV/pH unit. 76
- Figure 3.8.** (a) Tafel plots, $E = (E_{appl} - iR)$ for anodized NiB_i catalyst films deposited on a Pt rotating disk electrode by passing 1.0 mC cm⁻², and operated in 0.60 M B_i pH 8.5 (◆), 0.20 M B_i pH 9.2 (▲), 0.11 M B_i pH 10.2 (■), 0.10 M B_i pH 11.2 (●), and 0.10 M B_i pH 12.0 (▼). Each electrolyte contained an additional 0.9 M KNO₃ as supporting electrolyte to maintain an ionic strength of about 1 M. Koutecký–Levich plots were constructed to extract activation-controlled current densities where necessary. (b) Interpolation of Tafel plots at 2.5 mA cm⁻² (+), 0.25 mA cm⁻² (*), and 0.025 mA cm⁻² (×). Slopes are -90, -89, and -88 mV/pH unit respectively. 77
- Figure 3.9.** Plot of the pH dependence of steady-state electrode overpotential (■), at constant current density ($j_{anodic} = 10 > \mu\text{A cm}^{-2}$) for an anodized 1.0 mC cm⁻² catalyst film deposited onto FTO and operated in 0.1 M B_i 2 M KNO₃ electrolyte. The change in slope at pH 12.2 is consistent with the elevation of the bulk pH above the pK_a of an active site moiety. The inset shows Tafel plots, $\eta = (E - iR - E^\circ)$, for anodized catalyst films deposited onto a Pt RDE by passage of 1.0 mC cm⁻² and operated at 2000 rpm in 0.1 M KOH 1.9 M KNO₃ pH 12.9 (○) and 1.0 M KOH 1.0 M KNO₃ pH 13.8 (Δ) electrolyte. Tafel slopes are 28 and 30 mV/decade, respectively. 78
- Figure 3.10.** (a) Tafel plots, $E = (E_{appl} - iR)$, $\eta = (E - E^\circ)$, for anodized catalyst films deposited onto a Pt RDE by passage of 1.0 mC cm⁻² and operated in 1 M NaClO₄ pH 8.5 electrolyte (●). Koutecký–Levich analysis of steady state current densities at various rotation rates was used to eliminate mass transport limitations through solution. The data shown is the average of three consecutive runs. A Tafel plot of an identical catalyst film in 0.6 M KB_i 0.9 M KNO₃ pH 8.5 (0.1 M B_i⁻, total ionic strength = 1 M) electrolyte (▲), displaying a 32 mV/decade Tafel slope (—), is shown for comparison. (b) Activity profile of a 1.0 mC cm⁻² catalyst film deposited onto a Pt RDE and operated in 0.5 M KB_i 1.75 M KNO₃ pH 9.2 electrolyte after operation in 1.0 M NaClO₄, pH 8.5 electrolyte (▲), compared to the activity profile of a freshly prepared catalyst film (■). 80
- Figure 3.11.** Proposed pathway for O₂ evolution by Ni–B_i in B_i ([B(OH)₄⁻] > 20 mM) electrolyte, pH 8.5–14. The reversible dissociation of borate anion and an overall two-electron, three-proton equilibrium followed by a rate limiting chemical step, is consistent with the experimental electrochemical rate law. A μ-OH site possessing a pK_a of 12.2 is fully deprotonated in the resting state under highly alkaline conditions. Oxidation state assignments are approximate; oxidizing equivalents are likely extracted from orbitals with predominantly O 2p character, particularly for the pre-TLS intermediate. 89
- Figure 3.12.** Comparison of ultrathin Co–B_i and Ni–B_i OEC films with identical catalyst loadings of 6 nmol metal ions/cm². (a) Tafel plots of Co–B_i (●) and Ni–B_i (▲) in 0.5 M KB_i 1.75 M KNO₃ pH 9.2 electrolyte. Tafel slopes equal 55 and 31 mV/decade,

respectively (b) Schematic of the pH dependence of the current density and lower-limit turnover frequency of Co-B_i at a constant overpotential of 400 mV (blue, — —) and 300 mV (light blue, — · —) compared to that of Ni-B_i at 400 mV (light green, — —) and 300 mV (green, — · · —) overpotential. Curves were calculated using the appropriate experimentally-determined electrochemical rate laws. Ni-based films display a much higher *apparent* specific activity (since the true number of active sites cannot be known) than Co-based films above pH 8. However, due to their disparate electrochemical rate laws, a crossover is expected to occur around neutral pH, at which point Co-based films would yield higher activity anodes. The precise pH at which crossover occurs depends on the overpotential applied due to the different Tafel slopes.

92

Figure 4.1. Qualitative band diagram of a double junction PV-PEC water splitting cell depicting the thermodynamic potential separation of the OER and HER (•••), and the quasi-Fermi level (•••) and bend edge positions (—) throughout the cell under illumination with sustained water splitting at current density, j . The potential at each solution interface is given by the OER, η_{OER} , and HER, η_{HER} , overpotentials required to sustain the operating current density, j . For clarity of representation, solution and contact resistance losses are omitted.

109

Figure 4.2. Tafel plot, $\eta = (V_{\text{appl}} - iR - E^0)$, of a Ni-B_i catalyst film operated in 0.5 M B_i, pH 9.2 (▲), and a Co-B_i catalyst film operated in 1 M B_i, pH 9.2 (■). E^0 is the thermodynamic potential water splitting the under the conditions of the experiment, η is the overpotential, iR accounts for the uncompensated cell resistance. The slopes of the linear fits to the data are 52 mV/decade and 29 mV/decade for Co-B_i and Ni-B_i, respectively.

111

Figure 4.3. Electrochemical load of water splitting utilizing Co-B_i (— — —), Ni-B_i (· — ·), RuO₂ (— — ·), and LaMnO₃ (· · —) oxygen evolution catalysts and the j - V curve of an idealized model of an a-Si|nc-Si|nc-Si triple junction photovoltaic displaying $V_{\text{oc}} = 1.94$ V, $j_{\text{sc}} = 8.96$ mA cm⁻² (—) and an idealized hypothetical cell possessing $V_{\text{oc}} = 2.13$ V, $j_{\text{sc}} = 8.15$ mA cm⁻² (— — —). Open circles indicate operating current densities for the high V_{oc} cell and correspond to 10% SFE for all catalysts. Close circles indicate operating current densities for the low V_{oc} cell for which SFE is sensitive to catalyst performance.

113

Figure 4.4. Low SFE (red, — — with green, —) and high SFE PEC cells (red, — — with blue, — or purple, —). The j - V curves of a PV (red, — —) for a typical metal oxide semiconductor operating ($V_{\text{oc}} > 3.0$ V) and a PV (red, —) operating near the region of thermodynamic potential for water splitting (gray bar) at arbitrary current density j overlaid with Tafel curves of catalysts exhibiting increasing slope, i.e. increasing catalyst performance (green, — — to blue, — — to purple, —). Note the sensitivity of the overall SFE to catalyst performance for PVs operating near thermodynamic potential.

116

List of Tables

Table 2.1. Coulometric Titration of Ni–B _i catalyst films	44
Table 2.2. γ -NiOOH EXAFS Fitting Parameters	49
Table 2.3. Anodized Ni–B _i Catalyst EXAFS Fitting Parameters	50
Table 2.4. NaNiO ₂ EXAFS Curve Fitting Parameters	51
Table 2.5. β -NiOOH EXAFS Curve Fitting Parameters	51
Table 2.6. Non-Anodized Ni–B _i Curve Fitting Parameters	53

List of Abbreviations

a-Si	amorphous silicon
α	transfer coefficient
a_x	activity of species X
b	Tafel slope
β	symmetry factor
B_i	borate buffer
B_i^-	borate anion
C	capacitance
Co–OEC	cobalt-based catalyst deposited from weak-base electrolytes
Co–P _i	cobalt-based catalyst deposited from phosphate electrolytes
CV	cyclic Voltammogram
ΔG^\ddagger	Gibbs free energy of activation
E	potential at electrode surface
E^0	thermodynamic potential under standard conditions
E_{OC}	open-circuit potential of an electrode
ET	electron transfer
EXAFS	extended X-ray absorption fine structure
F	Faraday constant
FT	Fourier transform
FTO	fluorine-tin-oxide
Γ_{max}	total surface concentration of active sites
Γ_X	surface concentration of active sites existing in state X
η	overpotential
η'	overpotential at time zero in an open circuit decay experiment
HEC	hydrogen evolving catalyst
HER	hydrogen evolution reaction
η_{HER}	overpotential penalty associated with the hydrogen evolution reaction
η_{iR}	overpotential penalty associated with ohmic losses
η_{OER}	overpotential penalty associated with the oxygen evolution reaction
i	current
j	current density
J–T	Jahn–Teller
j_0	exchange current density
j_{sc}	short-circuit current density of a photovoltaic
k	angular wavenumber
K–L	Koutecký–Levich
k_{ET}	electron transfer rate constant
k_{ET}^0	electron transfer rate constant at zero overpotential for the OER

List of Abbreviations

N	number of absorber–backscatterer pairs in EXAFS
nc-Si	nanocrystalline silicon
NHE	normal hydrogen electrode
Ni–B _i	nickel-based catalyst deposited from borate electrolyte
NiPPI	potassium nickel(IV)paraperiodate
OEC	oxygen evolving catalyst
OER	oxygen evolution reaction
PCET	proton-coupled electron transfer
PEC	photoelectrochemical cell
PEM	proton exchange membrane
P _i	phosphate buffer
PT	proton transfer
PV	photovoltaic
Q	charge passed
R	in the context of electrochemistry: the solution/series resistance in the context of EXAFS: the real distance between absorber–backscatterer pairs
R'	in the context of EXAFS: the apparent distance between absorber–backscatterer pairs
RDE	rotating disk electrode
R_f	goodness-of-fit parameter in EXAFS
σ^2	EXAFS dampening factor due to thermal and static disorder
SFE	solar-to-fuels efficiency
τ	time constant of the open circuit decay transient of an electrode
θ_x	surface coverage of species X
TLS	turnover-limiting step
TOF	turnover frequency
TOFmin	lower-limit turnover frequency
v	reaction velocity
V_{OC}	open circuit voltage of a photovoltaic
V_{OP}	operating (net) voltage of a water splitting device
XANES	X-ray absorption near-edge structure
XAS	X-ray absorption spectroscopy

Chapter 1 — Introduction

1.1 Challenges for Solar Water Splitting

Global energy consumption is projected to roughly double by mid-century and triple by 2100.¹⁻⁴ This demand is driven by a growing world population that is projected to hit the 10 billion mark by 2050, in conjunction with an additional 3 billion people in the developing world who seek an improved standard of living.^{5,6} Even though this demand can be met by combustion of coal, oil, and/or natural gas, the rising cost of fossil fuels, energy security considerations, and the environmental ramifications of the continued reliance on the fossil resource base are cause for great concern. Atmospheric carbon dioxide concentrations are likely to triple if we attempt to satiate our energy appetite with coal, oil, or gas,⁷ and the current atmospheric CO₂ concentration is already the highest it has been in the last 650,000 years.⁸ It is indisputable that the ecology of earth is and will continue to be perturbed on an unprecedented and potentially catastrophic scale unless renewable carbon-neutral energy sources are swiftly developed and implemented.

Of all renewable energy sources, sunlight is the most abundant, possessing a resource base that far exceeds all other renewable energy sources combined;^{9,10} the solar energy that strikes the earth in one hour is enough to meet humanity's global energy demands for an entire year.² However, the highly mutable flux of sunlight necessitates a cheap and efficient storage scheme. Since such a process is currently unavailable, our utilization of solar energy still amounts to a minuscule fraction of the energy available.^{2,11} An attractive method to surmount this problem is to use sunlight to drive the energetically uphill "water splitting" reaction and store the energy in the energy-dense chemical bonds of molecular oxygen and hydrogen.^{2,12-14} These fuels will then be recombined to liberate the stored energy, regenerating water, and closing a zero-carbon energy cycle. This solar-to-fuels scheme mimics the essential steps in photosynthesis in which green plants store energy from sunlight in the bonds of glucose and oxygen.^{10,15} However, accomplishing this transformation efficiently and at sufficiently low-cost to penetrate global markets is a daunting challenge.^{9,16} Sunlight must be captured and directed to catalysts that can rearrange the bonds of water in a highly complex reaction involving the

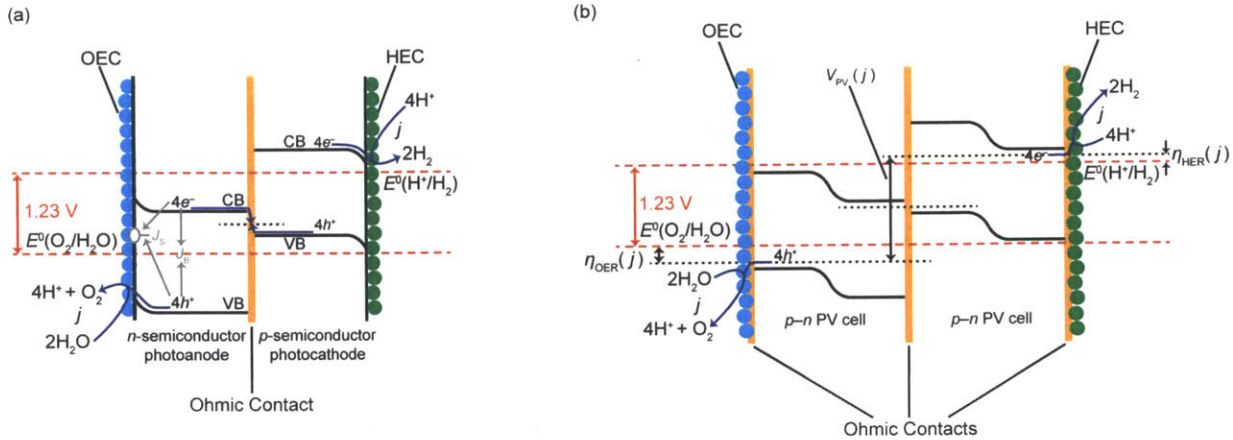


Figure 1.1. Schematic band diagram of (a) dual band gap p/n-PEC and (b) double junction PV-PEC architectures depicting the thermodynamic potential separation for water splitting (dashed red lines) along with the quasi-Fermi level (dashed black lines) and band edge positions (solid black lines) at a water splitting current density, j . Productive carrier motion is illustrated with dark blue arrows. In (a), two possible e^-/h^+ recombination pathways are shown in grey: recombination in the bulk of the semiconductor, J_B , and recombination due to surface states, J_S . Both pathways may be affected by the presence of catalysts at the surface. In (b) the respective OER and HER activation overpotentials at j , η_{OER} and η_{HER} , are shown. Additional overpotentials arising due to contact or solution resistances are omitted for clarity.

transfer of four electrons and four protons using cheap terrestrially-abundant materials, preferably under environmentally benign conditions.

One route to couple renewable sources such as solar energy to water splitting is to use a photovoltaic (PV) assembly to convert sunlight into an electric current, which is wired to a separate electrolyzer module. Although current commercial PV + electrolyzer technologies in this *indirect* configuration are capable of generating hydrogen from solar energy with efficiencies exceeding 20%,^{13,17} such technologies are presently too expensive to be feasible on a large-scale due to high costs of both PV and electrolyzer.^{16,18} The primary methods currently used to split water commercially involve the use proton-exchange membrane (PEM) electrolyzers that operate in acidic electrolytes, alkaline electrolyzers that operate in concentrated base, and solid oxide electrolyzers that operate at temperatures approaching 1000 °C.¹⁴ All three approaches are saddled with high balance of systems costs due to the heavily engineered

conditions required to operate under these harsh conditions. Furthermore, the PEM electrolyzer cost is compounded by the requisite precious metal catalysts and expensive membranes.¹⁴ To reduce the cost of solar-derived fuels, water splitting catalysts and electrolysis systems that can operate with high efficiency under more benign conditions must be developed. Even further reduction of costs for H₂ generation may be gained by developing oxygen evolving catalysts (OECs) and hydrogen evolving catalysts (HECs) that can be *directly* integrated with semiconducting materials to construct a monolithic solar-fuels device.^{15,19}

The various device configurations that have been proposed for direct solar-driven water splitting can be broadly categorized into photoelectrochemical systems that employ one or more solution-junctions (PEC) *versus* photovoltaic-photoelectrochemical (PV-PEC) devices, which contain only buried solid-state junctions (Figure 1).^{19,20} In solution-junction PEC devices, one or more semiconductor electrodes are exposed to an electrolyte solution such that the photo-generated carriers (electrons or holes) can be directed to the semiconductor-electrolyte interface to execute the water splitting reactions (Figure 1a). Since the semiconductor-solution interface is the critical determinant of the photovoltage generated and overall behavior of a PEC system, water splitting kinetics are not necessarily the pre-eminent factors to consider in device design. Thus, the appropriate catalyst for this application is not necessarily identical to that which is most efficient in an electrolyzer configuration.²¹ Instead, the target catalysts for such systems must be amenable to conformal coatings to accommodate the various electrode shapes and nanostructured textures commonly found for photoelectrode materials,^{22,23} and must also be capable of rapidly scavenging photogenerated carriers away from the photoanode/catalyst interface towards active sites in order to minimize electron/hole recombination either in the bulk or via surface trap states (J_B and J_S , respectively in Figure 1a). Furthermore, it is conceivable that coating the semiconductor surface with the catalyst could significantly impact the energetics of the solution-junction, which could impact PEC efficiency. Thus, these considerations present critical basic science challenges for the design of OECs and HECs that are compatible with the

desired photoanode or photocathode, respectively, and that can be integrated in a highly conformal fashion.

In contrast, typical PV-PEC architectures employ a multi-junction stack of light absorbers that are connected in series using thin-film ohmic contacts or tunnel junctions to generate open circuit voltages that are large enough to drive water splitting (Figure 1b). Thin-film ohmic contacts are then applied to each terminus of this stack to both protect the semiconductor from corrosion and enable efficient charge transfer to catalyst overlayers, which mediate the water splitting reactions.^{19,20} PV-PEC architectures distribute the burden of current rectification, charge separation, and photovoltage generation on the buried junctions while requiring only that the *total* cell photopotential is large enough (irrespective of the valence and conduction band edge positions of the constituent semiconductors themselves) to drive the water splitting reactions and overcome the ohmic losses due to cell resistance. Thus, efficient catalysis and photostability at the ohmic contact-catalyst-solution interfaces are among the preeminent prerequisites in these systems.

1.2 The Centrality of Catalysis for Efficient Energy Storage

Irrespective of the design chosen for the solar-fuels conversion process, the overpotential required to drive the water splitting reactions at the desired rate is a crucial determinant of the efficiency of the overall system. The water splitting reaction can be described by the electrochemical half-reactions, the oxygen evolution reaction (OER) and hydrogen evolution reaction (HER):



The velocity of the electrochemical reaction, v , is directly related to the measured current density at the electrode, j ($v = 4Fv$, where F is the Faraday constant). The overall voltage required to drive water splitting at any desired current density is given by:

$$V_{\text{overall}} = E^{\circ} + \eta_{\text{OER}} + |\eta_{\text{HER}}| + \eta_{\text{iR}} \quad (1.3)$$

E° is the thermodynamic potential for water splitting (1.23 V under standard conditions), which defines the energy content of the chemical fuel formed during water splitting, and the additional *overpotential* ($\eta_{\text{OER}} + |\eta_{\text{HER}}| + \eta_{\text{iR}}$) indicates the amount of energy lost as heat. η_{OER} and η_{HER} are the *activation* overpotentials for the OER and HER, respectively, and η_{iR} is the overpotential associated with ohmic losses in the device, including solution and contact resistances. Whereas η_{iR} can be reduced by appropriate engineering and device design, the activation overpotentials relate directly to the chemical complexity of the water splitting reactions and the kinetic facility with which the oxygen evolving catalysts (OECs) and hydrogen evolving catalysts (HECs) mediate the half reactions. That is, η_{OER} and η_{HER} are directly related to the magnitude of the activation barrier(s) that must be surmounted for the reaction to proceed at any appreciable rate. The relationship between the activation overpotential and current density at an electrode is expressed in the Tafel law:

$$\eta = b \log (j / j_0) \quad (1.4)$$

The extrapolated current density at zero driving force for the overall reaction ($\eta = 0$) is known as the exchange current density, j_0 . Thus, j_0 is a descriptor of the intrinsic activity of the electrode towards the reaction at the thermodynamic potential. The parameter b , the Tafel slope, determines the extent to which changes in driving force influence the rate of the reaction, and therefore this parameter depends on the mechanism by which the reaction proceeds via the catalyst surface. The ideal catalyst should possess a high exchange current density and low Tafel slope in order to require a low overpotential for sustaining a high current density. Since a full description of any electrocatalyst must take into account both parameters, the most useful method of describing the activity of an electrocatalyst is by plotting the overpotential as a function of the logarithm of steady state current densities (Tafel plot).

Along these lines, catalysis lies at the nexus of the light and dark chemistries of photoelectrochemical water splitting as it provides the conduit through which the one electron-

hole generation attendant to light capture and conversion is aggregated and discharged towards fuel formation. Of the two half reactions, the OER is the most kinetically demanding, since it requires the distribution of four redox processes over a narrow potential range (redox leveling), the coupling of multiple proton and electron transfers, and the formation of two oxygen–oxygen bonds.^{24–26} Consequently, the majority of the activation overpotential in water splitting tends to arise due to kinetic barriers associated with the OER.²⁷ Transition metal oxides are known to meet the requirements for highly active oxygen evolution catalysts,^{28–30} with nickel oxides being the most attractive anode materials under alkaline conditions because of their low cost, high catalytic activity, and stability to corrosion.³⁰ Catalysis development for the OER has historically focused on addressing challenges associated with electrolyzer development—operation at high current density at pH extremes—without consideration of the problems concerning light management or stability of fragile semiconductors. We have emphasized the development of catalysts targeted to PEC and PV–PEC device applications. Accordingly we have focused on investigations across a wide pH range, since the stability manifold of the optimal semiconductor(s) remains unknown.

1.3 Electrodeposited Co- and Ni-based OECs

Researchers in our group serendipitously discovered that OECs self-assemble as thin films upon electrolysis of aqueous solutions of $\text{Co}^{2+}(\text{aq})$ containing a good proton acceptor, like phosphate (P_i) or borate (B_i), pH 7–9.^{31–33} As amorphous oxidic^{34–36} catalysts based on first row transition metals that progress through low-valent, labile intermediate states during O_2 evolution,³⁷ these materials possess a predilection for degradation back to their soluble $\text{Co}^{2+}(\text{aq})$ precursors. However, a unique feature of these catalyst films is their capacity to self-heal,^{38,39} which ensures their indefinite functional stability notwithstanding their inherent structural fragility. These features also establish the functional integrity of these catalyst systems in impure water sources,⁴⁰ making them potential targets for future cheap, distributed energy storage systems in impoverished regions. Owing to the terrestrial abundance of the starting

materials for these Co–OECs and the simple conditions required for their electrosynthesis, they have emerged as prime candidates for integration with a myriad of inorganic, and organic-inorganic hybrid light absorbers in solution-junction PEC systems (Figure 1a)^{41–55} as well as buried-junction PV–PEC water splitters (Figure 1b).^{56–58}

We sought to explore the synthesis of catalyst films based on other first-row transition metals with the goal of identifying the mechanistic basis for any differences in catalytic activity and stability. We found that controlled potential electrolysis of borate-buffered solutions of nickel salts at pH 9.2 also afforded the deposition of an OEC as a thin film.⁵⁹ These nickel-borate (Ni–B_i) catalyst films were shown to mediate the OER with 100% faradaic efficiency with modest overpotentials of ~0.4 V required for current densities of 1 mA/cm².⁵⁹ In contrast to Co–P_i and Co–B_i catalysts, the potentials sufficient for initiating catalyst formation were not as well-separated from those required for driving oxygen evolution, suggesting disparate kinetics of catalyst formation and/or water oxidation compared to those of the Co–OECs. Intriguingly, Ni–B_i films required extensive (12 h) pre-electrolysis treatments in order to establish reproducible steady state behavior,⁵⁹ unlike Co–OEC films that displayed unchanging steady state OER activity immediately following film deposition. However, Ni–B_i films shared a common characteristic with Co–OEC films in that they also appeared amorphous,⁵⁹ obstructing a molecular-level understanding of catalyst structure, and by extension formation and function.

1.4 Scope of the Thesis

The ostensibly amorphous nature of the Ni–B_i catalyst made it recalcitrant to structural characterization by conventional X-ray and electron diffraction techniques. Thus a pre-eminent question that remained was: what structural motifs are present in Ni–B_i films? We also considered: what transformations in film structure accompanied the aforementioned electrochemical treatment and how do they correlate with any activity changes that may be observed over the course of the pre-electrolysis? Chapter 2 addresses these two critical questions and shows that as-deposited catalyst films are comprised of metal oxido clusters populated by

Ni(III) centers that are subsequently transformed to a mixed-valence Ni(III/IV) state during anodization, which correlates with drastic improvements in catalytic activity. These results which indicate that Ni(IV) character in the resting state is paramount to high catalytic activity stand at odds with the prevailing dogma for OER at Ni-based anodes. Chapter 3 addresses the following questions: What is the mechanism of oxygen evolution at Ni-B_i? What is the kinetic importance of the buffer in the water oxidation mechanism? How does the OER kinetic profile of Ni-B_i compare with that of Co-P_i/B_i over a wide pH range? Electrokinetic studies reveal a novel mechanism of oxygen evolution and show that activity trends among OECs at pH extremes may be reversed at intermediate pH. Chapter 4 discusses the significance of the disparate OER mechanisms of Co-P_i/B_i and Ni-B_i for the development of PV-PEC devices with high solar-to-fuels efficiencies (SFEs).

1.5 Concluding Remarks

A critical challenge to the development of solar-driven water splitting systems that can meet global demands for energy is the development of catalysts that can mediate the OER efficiently and are properly matched to light harvesting/charge separating manifolds. HEC and OEC development thus far has focused primarily on materials that are capable of operating at the pH extremes, however such systems are not suited for the unique requirements of solar-driven water splitting and have therefore failed to challenge the status quo of our heavy reliance on fossil fuels. New technologies are needed to meet this urgent 21st century demand. These novel systems will be based on explorations into the fundamental science of water splitting under benign conditions (particularly at intermediate pH) where the structural stability of oxidic materials is not guaranteed. Thus a new class of dynamic, self-healing catalyst materials is required. The nickel-borate catalyst presented here is a promising material for solar water splitting, and the following chapters examine our initial forays into understanding the structural and mechanistic basis of its catalytic behavior.

1.6 References

- (1) Energy Information Association; U.S. Department of Energy: Washington DC; www.eia.doe.gov (accessed September 2012).
- (2) Lewis, N. S.; Nocera, D. G. *Proc. Natl. Acad. Sci. U.S.A.* **2006**, *103*, 15729.
- (3) Hoffert, M. I.; Caldeira, K.; Jain, A. K.; Haites, E. F.; Harvey, L. D. D.; Potter, S. D.; Schlesinger, M. E.; Schneider, S. H.; Watts, R. G. Wigley, T. M. L.; Wuebbles, D. J. *Nature* **1998**, *395*, 881.
- (4) Chu, S.; Majumdar, A. *Nature* **2012**, *488*, 294.
- (5) *2012 World Population Data Sheet*; Population Reference Bureau: Washington, DC, 2012; www.prb.org (accessed September 2012).
- (6) Lee, R. *Science* **2011**, *333*, 569.
- (7) *Climate Change 2007: Mitigation of Climate Change*; IPCC Working Group III Fourth Assessment Report; Intergovernmental Panel on Climate Change: Geneva, 2007.
- (8) Siegenthaler, U.; Stocker T. F.; Lüthi, D.; Monnin, E.; Schwander, J.; Stauffer, B.; Raynaud, D.; Barnola, J.-M.; Fischer, H.; Masson-Delmotte, V.; Jouzel, J. *Science* **2005**, *310*, 1313.
- (9) Cook, T. R.; Dogutan, D. K.; Reece, S. Y.; Surendranath, Y.; Teets, T. S.; Nocera, D. G. *Chem. Rev.* **2010**, *110*, 6474.
- (10) Barber, J. *Chem. Soc. Rev.* **2009**, *38*, 185.
- (11) United Nations Development Program *World Energy Assessment: Overview 2004 Update*; United Nations: New York, 2004.
- (12) Nocera, D. G. *Inorg. Chem.* **2009**, *48*, 10001.
- (13) Khaselev, O.; Turner, J. A. *Science* **1998**, *280*, 425.
- (14) Grimes, C. A.; Varghese, O. K.; Ranjan, S. *Light, Water, Hydrogen: The Solar Generation of Hydrogen by Water Photoelectrolysis*; Springer: New York, 2008.

- (15) Nocera, D. G. *Acc. Chem. Res.* **2012**, *45*, 767.
- (16) Lewis, N. S. *Science* **2007**, *315*, 798.
- (17) Turner, J. A. *Science* **2004**, *305*, 972.
- (18) Turner, J. A. *Science* **1999**, *285*, 687.
- (19) Walter, M. G.; Warren, E. L.; McKone, J. R.; Boettcher, S. W.; Mi, X.; Santori, E. A.; Lewis, N. S. *Chem. Rev.* **2010**, *110*, 6446.
- (20) Hanna, M. C.; Nozik, A. J. *J. Appl. Phys.* **2006**, *100*, 074510.
- (21) Ye, H.; Park, H. S.; Bard, A. J. *J. Phys. Chem. C* **2011**, *115*, 12464.
- (22) Kay, A.; Cesar, I.; Grätzel, M. *J. Am. Chem. Soc.*, **2006**, *128*, 15714.
- (23) Maiolo, J. R.; Kayes, B. M.; Filler, M. A.; Putnam, M. C.; Kelzenberg, M. D.; Atwater, H. A.; Lewis, N. S. *J. Am. Chem. Soc.* **2007**, *129*, 12346.
- (24) Eisenberg, R.; Gray, H. B. *Inorg. Chem.* **2008**, *47*, 1697.
- (25) Liu, F.; Concepcion, J. J.; Jurss, J. W.; Cardolaccia, T.; Templeton, J. L.; Meyer, T. J. *Inorg. Chem.* **2008**, *47*, 1727.
- (26) Betley, T. A.; Surendranath, Y.; Childress, M. V.; Alliger, G. E.; Fu, R.; Cummins, C. C.; Nocera, D. G. *Phil. Trans. Royal Soc. B-Biol. Sci.* **2008**, *363*, 1293.
- (27) Surendranath, Y.; Nocera, D. G. *Prog. Inorg. Chem.* **2011**, *57*, 505.
- (28) Tarasevich, M. R.; Efremov, B. N. In *Electrodes of Conductive Metal Oxides, Part A*; Trasatti, S., Ed.; Elsevier: Amsterdam, 1980; Ch. 5.
- (29) Trasatti, S. In *Electrochemistry of Novel Materials*; Lipkowsky, J., Ross, P. N., Eds.; VCH: New York, 1994; Ch. 5.
- (30) Kinoshita, K. *Electrochemical Oxygen Technology*; Wiley-Interscience: New York, 1992; Ch. 2.

- (31) Kanan, M. W.; Nocera, D. G. *Science* **2008**, *321*, 1072.
- (32) Kanan, M. W.; Surendranath, Y.; Nocera, D. G. *Chem. Soc. Rev.* **2009**, *38*, 109.
- (33) Surendranath, Y.; Dincă, M.; Nocera, D. G. *J. Am. Chem. Soc.* **2009**, *131*, 2615.
- (34) Risch, M.; Khare, V.; Zaharieva, I.; Gerencser, L.; Chernev, P.; Dau, H. *J. Am. Chem. Soc.* **2009**, *131*, 6936.
- (35) Kanan, M. W.; Yano, J.; Surendranath, Y.; Dincă, M.; Yachandra, V. K.; Nocera, D. G. *J. Am. Chem. Soc.* **2010**, *132*, 13692.
- (36) Du, P.; Kokhan, O.; Chapman, K. W.; Chupas, P. J.; Tiede, D. M. *J. Am. Chem. Soc.* **2012**, *134*, 11096.
- (37) Surendranath, Y.; Kanan, M. W.; Nocera, D. G. *J. Am. Chem. Soc.* **2010**, *132*, 16501.
- (38) Lutterman, D. A.; Surendranath, Y.; Nocera, D. G. *J. Am. Chem. Soc.* **2009**, *131*, 3838.
- (39) Surendranath, Y.; Lutterman, D. A.; Liu, Y.; Nocera, D. G. *J. Am. Chem. Soc.* **2012**, *134*, 6326.
- (40) Esswein, A. J.; Surendranath, Y.; Reece, S. Y.; Nocera, D. G. *Energy Environ. Sci.* **2011**, *4*, 499.
- (41) Ye, H.; Park, H. S.; Bard, A. J. *J. Phys. Chem. C* **2011**, *115*, 12464.
- (42) Zhong, D. K.; Sun, J.; Inumaru, H.; Gamelin, D. R. *J. Am. Chem. Soc.* **2009**, *131*, 6086.
- (43) Steinmiller, E. M. P.; Choi, K.-S. *Proc. Natl. Acad. Sci. USA* **2009**, *106*, 20633.
- (44) Zhong, D. K.; Gamelin, D. R. *J. Am. Chem. Soc.* **2010**, *132*, 4202.

- (45) Klahr, B.; Gimenez, S.; Fabregat-Santiago, F.; Bisquert, J.; Hamann, T. W. *J. Am. Chem. Soc.* **2012**, *134*, 16693.
- (46) McDonald, K. J.; Choi, K.-S. *Chem. Mater.* **2011**, *23*, 1686.
- (47) Zhong, D. K.; Cornuz, M.; Sivula, K.; Grätzel, M.; Gamelin, D. R. *Energy Environ. Sci.* **2011**, *4*, 1757.
- (48) Seabold, J. A.; Choi, K.-S. *Chem. Mater.* **2011**, *23*, 1105.
- (49) Pilli, S. K.; Furtak, T. E.; Brown, L. D.; Deutsch, T. G.; Turner, J. A.; Herring, A. M. *Energy Environ. Sci.* **2011**, *4*, 5028.
- (50) Zhong, D. K.; Choi, S.; Gamelin, D. R. *J. Am. Chem. Soc.* **2011**, *133*, 18370.
- (51) Jeon, T. H.; Choi, W.; Park, H. *Phys. Chem. Chem. Phys.* **2011**, *13*, 21392.
- (52) Wang, D.; Li, R.; Zhu, J.; Shi, J.; Han, J.; Zong, X.; Li, C. *J. Phys. Chem. C* **2012**, *116*, 5082.
- (53) Pilli, S. K.; Deutsch, T. G.; Furtak, T. E.; Turner, J. A.; Brown, L. D.; Herring, A. M. *Phys. Chem. Chem. Phys.* **2012**, *14*, 7032.
- (54) Higashi, M.; Domen, K.; Abe, R. *J. Am. Chem. Soc.* **2012**, *134*, 6968.
- (55) Bledowski, M.; Wang, L.; Ramakrishnan, A.; Bétard, A.; Khavryuchenko, O. V.; Beranek, R. *ChemPhysChem* **2012**, *13*, 3018.
- (56) Young, E. R.; Costi, R.; Paydavosi, S.; Nocera, D. G.; Bulović, V. *Energy Environ. Sci.* **2011**, *4*, 2058.
- (57) Pijpers, J. J. H.; Winkler, M. T.; Surendranath, Y.; Buonassisi, T.; Nocera, D. G. *Proc. Natl. Acad. Sci. U.S.A.* **2011**, *108*, 10056.

(58) Reece, S. Y. ; Hamel, J. A.; Sung, K.; Jarvi, T. D.; Esswein, A. J.; Pijpers, J. J. H.; Nocera, D. G. *Science* **2011**, *334*, 645.

(59) Dincă, M.; Surendranath, Y.; Nocera, D. G. *Proc. Natl. Acad. Sci. U.S.A.* **2010**, *107*, 10337.

Chapter 2 — Structure and Valency of Nickel–Borate Oxygen Evolving Catalysts

Portions of this chapter have been published:

Bediako, D. K.; Lassalle-Kaiser, B.; Surendranath, Y.; Yano, J.; Yachandra, V. K.; Nocera, D.

G. J. Am. Chem. Soc. **2012**, *134*, 6801. – Reproduced with permission. Copyright 2012

American Chemical Society

2.1 Introduction

In Chapter 1 the importance of highly active oxygen evolving catalysts (OECs) for solar energy storage by water splitting was underscored. In particular, we highlighted the development of OEC systems that are capable of operating under intermediate pH conditions as a critical component for the development of cheap, distributed solar-driven water splitting devices. Within the context of water splitting catalysts designed for operation at intermediate pH, we introduced amorphous nickel-based¹ and cobalt-based²⁻⁴ OECs formed as thin films upon electrolyzing solutions of Ni²⁺(aq) and Co²⁺(aq), respectively, in the presence of a proton-accepting electrolyte such as phosphate (P_i) or borate (B_i) (pH 7–9). These catalysts perform OER under mild conditions and at high activity,⁵ and accordingly they lend themselves to the construction of novel direct solar-to-fuels architectures such as the artificial leaf.⁶⁻⁹

Continued development of improved catalysts requires an understanding of how catalyst structure correlates with catalytic activity. However, a challenge with constructing OER structure-function relations for solid-state materials is to observe active sites relative to the bulk.¹⁰⁻¹³ To this end, our recent discovery of such heterogeneous OEC films composed of molecular-like metal-oxido clusters¹⁴⁻¹⁶ offers the opportunity to begin defining OER structure-function relations because of a higher density of active site species. Nickel-borate (Ni–B_i) and cobalt-phosphate/borate (Co–P_i/Co–B_i) catalyst films may be self-assembled under nearly identical potential and pH conditions.^{1,3} Yet the Ni–B_i films are unique because they require a subsequent oxidative pretreatment or anodization in order to attain a well-defined OER activity.¹ In contrast, maximal OER activity of Co–P_i/Co–B_i is observed immediately following electrodeposition and remains unchanged indefinitely.¹⁷ The requirement for anodic pretreatment in the case of Ni–B_i leads us to postulate that an underlying structure and/or valency change was accompanying the marked increase in catalytic activity during the anodization process. This observation permits a structure-function correlation of OER activity to be undertaken with unprecedented fidelity. Because Ni–B_i is composed of small nanosized domains

of NiOOH,¹⁶ a much larger fraction of nickel centers are surface exposed in Ni-B_i relative to its extended solid congeners, suggesting that its OER activity is far more sensitive to changes in average structure and nickel valency than extended NiOOH materials.

We now report *in situ* X-ray absorption spectroscopy (XAS) studies which track changes in nickel oxidation state and catalyst structure that accompany a greater than two order of magnitude increase in OER activity during catalyst anodization. Correlation of coulometric measurements to *in situ* XANES spectra reveal that anodization increases the average oxidation state of Ni-B_i films during catalysis, with fully activated films possessing a mean resting state nickel oxidation state of +3.6, in contrast to a mean resting state nickel oxidation state of about +3.16 for non-activated films maintained at the same potential. Based on the structural parameters extracted from fitting EXAFS data of anodized Ni-B_i films, we propose that the *in situ* catalyst attains a Ni(IV) oxidation state within sheets of edge-sharing NiO₆ octahedra with ordered domain sizes no smaller than 2 nm. The changes in oxidation state and short-range structure that accompany Ni-B_i anodization are evocative of the transformation of β-NiOOH to γ-NiOOH, challenging the long-held view^{18,19} that the β-NiOOH phase effects more efficient OER catalysis.

2.2 Results

2.2.1 Catalyst Electrodeposition, Anodization and Electrochemistry.

Catalyst films were prepared by controlled potential electrolysis of 0.1 M KB_i, pH 9.2, electrolyte (0.1-B_i) containing 0.40 mM Ni(aq)²⁺. In our initial communication,¹ we reported that catalyst films were prepared by subjecting stirred 1 mM Ni(aq)²⁺ solutions in 0.1-B_i to bulk electrolysis at 1.3 V with the passage of 0.3–10 C/cm². Similarly, the *ex situ* XAS study of Ni-B_i¹⁶ followed the same basic procedure to prepare the catalyst. Whereas catalyst films deposit rapidly under these conditions, such films suffer from poor adhesion to the substrate and heterogeneity in thickness over the electrode surface, in part due to the non-uniform rate of mass

transport to different parts of the electrode under these conditions. For the purpose of the studies reported here, much thinner and more uniform films were desired. Films were prepared therefore from less concentrated $\text{Ni}(\text{aq})^{2+}$ solutions and at an applied potential of 1.15 V without stirring. The passage of $1.0 \text{ mC}/\text{cm}^2$ during deposition required a period of 60–80 s. Because oxygen evolution is coincident with film formation at these potentials, the charge passed is not expected to be strictly representative of the number of nickel centers in the film. But this value does allow for an initial upper-limit estimate of catalyst loading for these brief deposition times. Such films therefore contain $<10 \text{ nmol}/\text{cm}^2$ and are $<7 \text{ nm}$ thick (see section 3.5).

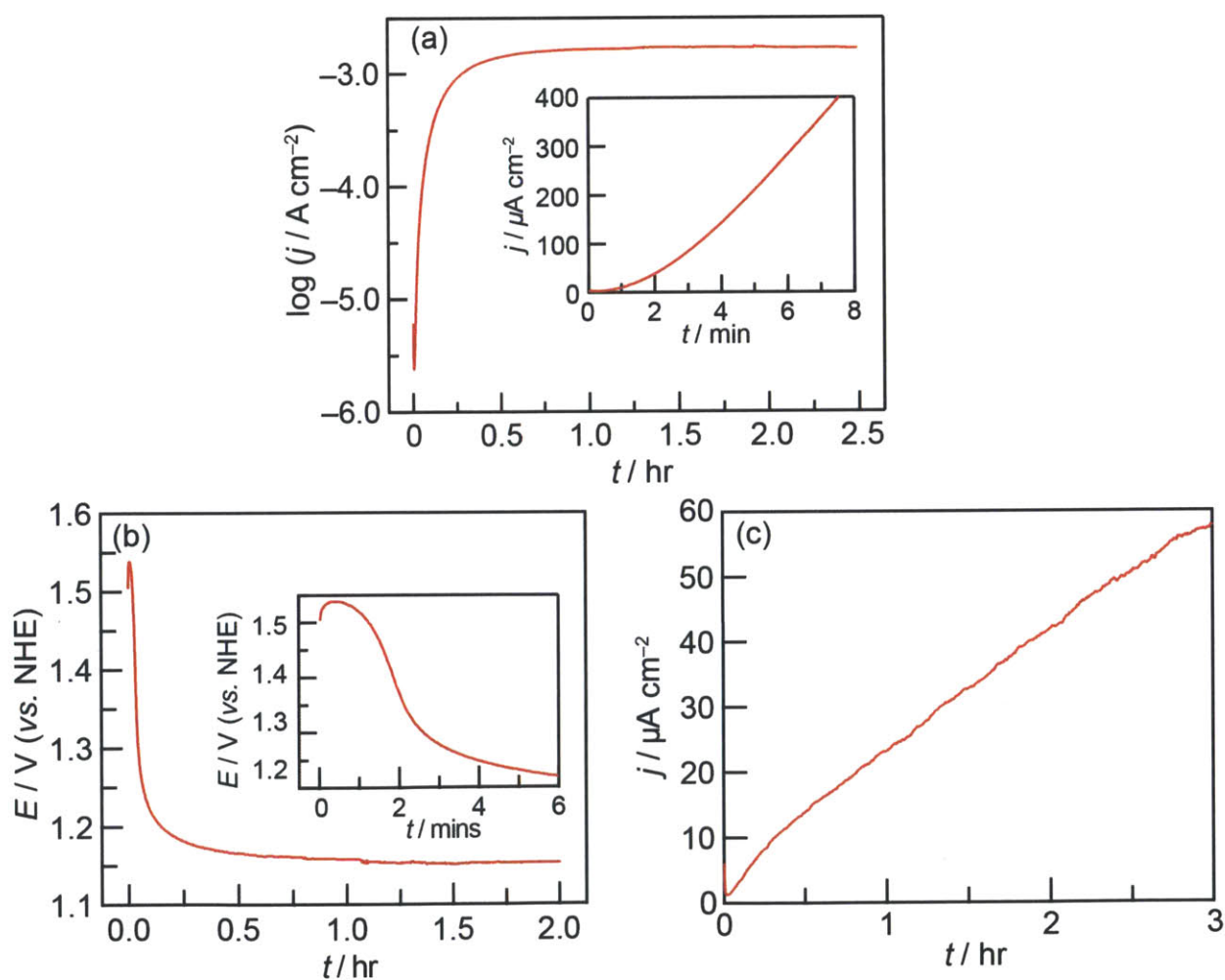


Figure 2.1. Change in oxygen evolution current density as a function of anodization duration for a $1 \text{ mC}/\text{cm}^2$ Ni-Bi film on an FTO substrate, operated at (a) 1.1 V in 1.0 M KBi pH 9.2 electrolyte, (b) $3.5 \text{ mA}/\text{cm}^2$ in 1.0 M KBi pH 9.2 electrolyte, and (c) 1.1 V in 0.1 M KBi pH 9.2 electrolyte.

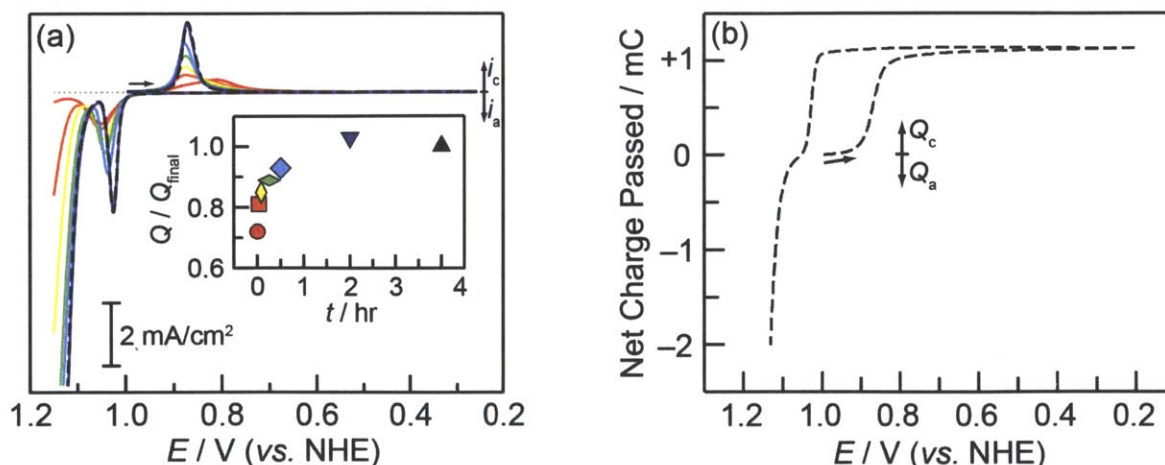


Figure 2.2. (a) Cyclic voltammograms (CVs) in 1.0 M KBi (pH 9.2) electrolyte at 100 mV/s of 1 mC/cm^2 Ni-B_i catalyst films non-anodized (red —), and after 2 min (orange —), 5 min (yellow —), 15 min (green —), 30 min (light blue —), 2 h (blue —) and 4 h (black —) of anodization at 1.1 V (vs. NHE) in 1.0 M KBi pH 9.2 electrolyte. The background CV of a blank FTO substrate is also displayed (grey - -). The inset shows the ratio of the integrated charge under the cathodic wave observed in the first scan to lower potentials in the case of each film relative to that of the 4 h-anodized film. (b) Coulometric analysis of a fully anodized 1 mC/cm^2 Ni-B_i catalyst film.

Following electrodeposition, films were anodized in stirred 1.0 M KBi , pH 9.2, electrolyte (1.0-B_i) by application of 1.1 V (with correction for ohmic potential losses) for 2.5 h. Over the course of anodization, the current density increased by greater than two orders of magnitude (Figure 2.1a). Alternatively, films could be anodized by passing 3.5 mA/cm^2 over a similar duration, resulting in a decrease of about 300 mV in measured potential (Figure 2.1b). Operation of the catalyst at 1.1 V in 0.1-B_i, with compensation for ohmic losses, results in a very gradual increase in the current density over time (Figure 2.1c), with no plateau in activity observed after 3 h. These results demonstrate that the rate of anodization is dependent on electrolyte concentration.

Figure 2.2a displays cyclic voltammograms (CVs) for independently prepared films (1.0 mC/cm^2) subject to anodization for varying times. For freshly-deposited non-anodized films, the initial sweep from 1.0 V to more negative potentials results in a broad and asymmetric cathodic wave with a shoulder at 0.87 V and a peak at $E_{p,c} = 0.81$ V, corresponding to reduction of the

surface-adsorbed species. The return scan to more positive potentials displays an anodically shifted oxidation wave centered at $E_{p,c} = 1.05$ V; onset of a catalytic wave is not observed until ~ 1.13 V. With anodization, the cathodic and anodic waves of the surface-adsorbed species become sharper and more symmetric, and the catalytic wave shifts to lower potential and becomes more pronounced. There is no difference in the voltammetric features of films anodized after 2 h; both 2-h and 4-h anodized films display cathodic and anodic waves centered at $E_{p,c} = 0.87$ V and $E_{p,a} = 1.025$ V respectively. The inset of Figure 2.2a shows the ratio of the charge passed in the reductive sweep for films at different times of anodization (Q) to that of the 4-h anodized film (Q_{final}).

Quantitative determination of the average oxidation state of nickel in anodized Ni-B_i catalyst films at 1.0 V was obtained by determining the charge required to discharge such films to the reduced Ni(II) state. Following anodization, films were held at 1.0 V for 300 s to allow the current density to attain a steady-state value ($\sim 1 \mu\text{A}/\text{cm}^2$). At 300 s, the potential was swept at 100 mV/s without pause to 0.2 V and back to 1.2 V. A background subtraction was employed to eliminate any excess charge caused by miscellaneous faradaic processes occurring at the FTO substrate alone. Such charges accounted for less than 2% of the total charge passed. Determination of the cumulative charge passed during each sweep segment (Figure 2.2b), permits calculation of the mean number of electrons consumed per nickel center, provided the amount of nickel on the electrode can be accurately determined. Catalyst loading was quantified by digestion of films in a known volume of dilute acid immediately after the electrochemical experiment. CVs of the FTO substrates in 1.0-B_i electrolyte after film dissolution were indistinguishable from background CVs collected before electrodeposition, indicating that dissolution was quantitative. Digests were analyzed for nickel concentration by ICP-MS. The results of such measurements on three independent films and the computed number of electrons discharged per nickel center (about 1.6 in each case) are listed in Table 2.1. These coulometric

Table 2.1. Coulometric Titration of Ni–B_i catalyst films

Charge / mC ^a	Ni loading / nmol ^b	No. e ⁻ consumed per Ni
1.14	7.5 (0.2)	1.63 (0.04)
1.13	7.2 (0.2)	1.62 (0.04)
1.08	7.1 (0.2)	1.58 (0.04)

^a Total charge passed upon reduction of anodized Ni–B_i catalyst films at 0.2 V.

^b Determined by quadrupole ICP-MS.

experiments establish an average nickel oxidation state of +3.61(7) for anodized Ni–B_i films biased at 1.0 V.

This coulometric measurement also allows us to determine the average oxidation state of nickel centers in non-anodized films. As shown in the inset of Figure 2, the electrochemical reduction of non-anodized films to their Ni(II) state consumes 72% of the charge required to reduce anodized films. This implies an average number of electrons discharged per nickel center of about 1.16, and defines an average oxidation state of +3.16(5) for films prior to anodization.

2.2.2 *In situ* X-Ray Absorption Spectroscopy.

Nickel K-edge X-ray absorption spectra (XAS) were collected on Ni–B_i films deposited on an ITO electrode. The precise deposition sequence for the non-anodized and anodized films is described in section 2.5. In both cases, XAS spectra were collected 5 min after applying a potential to ensure that the system had reached steady state.

Figure 2.3a presents the XANES spectra of an anodized Ni–B_i film poised at 1.0 and 0.4 V, together with model compounds Ni(OH)₂, β-NiOOH, γ-NiOOH and K₂Ni(H₂IO₆)₂ (potassium nickel(IV) paraperiodate, NiPPI) possessing formal nickel oxidation states of +2, +3, +3.6 and +4 respectively. The edge position of each model compound shifts to higher energies with increasing formal oxidation state. The edge position of the crystalline γ-NiOOH compound used in this study, which is an off-stoichiometric compound with a formal nickel oxidation state of about +3.6,³⁴ is approximately halfway (8345.0 eV, measured at half height F/I₀ = 0.5) between

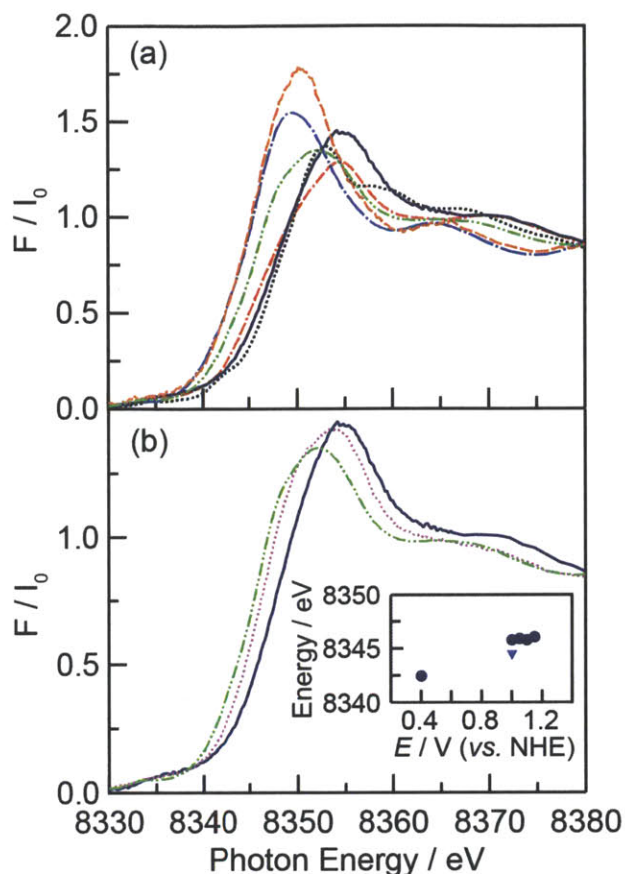


Figure 2.3. (a) XANES spectra of model compounds: Ni(OH)₂ (blue — ■ — ■), β-NiOOH (green — · · · — · · ·), γ-NiOOH (red — · — ·), NiPPI (black · · · · ·) and anodized Ni-B_i films at 0.4 V (orange — — —) and 1.0 V (dark blue — — —). (b) XANES spectra of a non-anodized Ni-B_i film poised at 1.0 V (purple · · · · ·), an anodized Ni-B_i film poised at 1.0 V (dark blue — — —), and β-NiOOH (green — · · · — · · ·). The inset shows the edge energy at half jump height as a function of applied potential for anodized (dark blue ●) and non-anodized (blue ▼) Ni-B_i.

the stoichiometric Ni(III) compound β-NiOOH (8343.7 eV) and stoichiometric Ni(IV) compound NiPPI (8346.4 eV). The edge shape and position of the anodized film in its fully oxidized state (poised at 1.0 V) (8345.8 eV) is similar to that of γ-NiOOH (8345.0 eV) whereas, in its fully reduced state (poised at 0.4 V), the edge shape and position of the anodized film (8342.5 eV) matches that of Ni(OH)₂ (8342.4 eV), indicating a mean oxidation state of +2. Although the edge position of a XANES spectrum is not a straightforward indicator of the oxidation state of metals owing to the several parameters that contribute to the XANES spectra (i.e. charge density, ligand symmetry, and spin density),²⁰ the trend observed here indicates that

anodized Ni-B_i films poised at 1.0 V possess significant Ni(IV) content, with a mean oxidation state of nickel centers near +3.6, consistent with the coulometric measurements. For anodized Ni-B_i films poised at potentials of 1.15, 1.10, 1.05 and 1.00 V (Figure 2.3b inset), there was essentially no shift in the XANES edge energy. We therefore surmise that over this potential range anodized Ni-B_i films do not display any changes in average nickel oxidation state despite the three orders of magnitude change¹ in the rate of catalytic turnover.

XANES spectra were also collected on a non-anodized Ni-B_i film under 1.0 V applied potential in 0.1-B_i. Because anodization is not pronounced under these conditions (Figure 2.1c), XAS spectra of such films are expected to be mostly representative of films prior to anodization with low catalytic activity. As shown in Figure 2.3b, the XANES spectrum of a non-anodized Ni-B_i film poised at 1.0 V displays an edge energy of 8344.5 eV (at F/I₀ = 0.5), which lies 0.8 eV positive of that of the stoichiometric Ni(III) compound β-NiOOH (8343.7 eV) and 1.3 eV below the edge position of anodized films held at the same potential (8345.8 eV). This edge position suggests a formal nickel oxidation state for the non-anodized films between +3 and +3.6.

EXAFS data collected on anodized Ni-B_i films *in operando* were found to be comparable to that of γ-NiOOH. The crystal structure^{21,34} of γ-NiOOH is shown in Figure 2.4a, and a fragment of the edge-sharing NiO₆ octahedra that comprise the layered material is presented in Figure 2.4b. Figure 2.4c presents the *k*³-weighted EXAFS spectra of γ-NiOOH along with that of an anodized Ni-B_i catalyst film poised at 1.05 V. The corresponding Fourier transform (FT) EXAFS spectra are shown in Figure 2.4d. The abscissa in the FT spectra is the apparent distance (*R'*), which is shorter than the actual distance between the absorber-backscatterer atom pairs due to a phase shift. The EXAFS spectra display two main peaks: peak I reflects the presence of Ni-O interactions (path a-b in Figure 2.4b), and peak II manifests Ni-Ni interactions (path a-c), as demonstrated by the EXAFS fits (*vide infra*). The positions of peaks in the FT EXAFS spectra of anodized Ni-B_i films are similar to those of γ-NiOOH but there are differences in peak intensity.

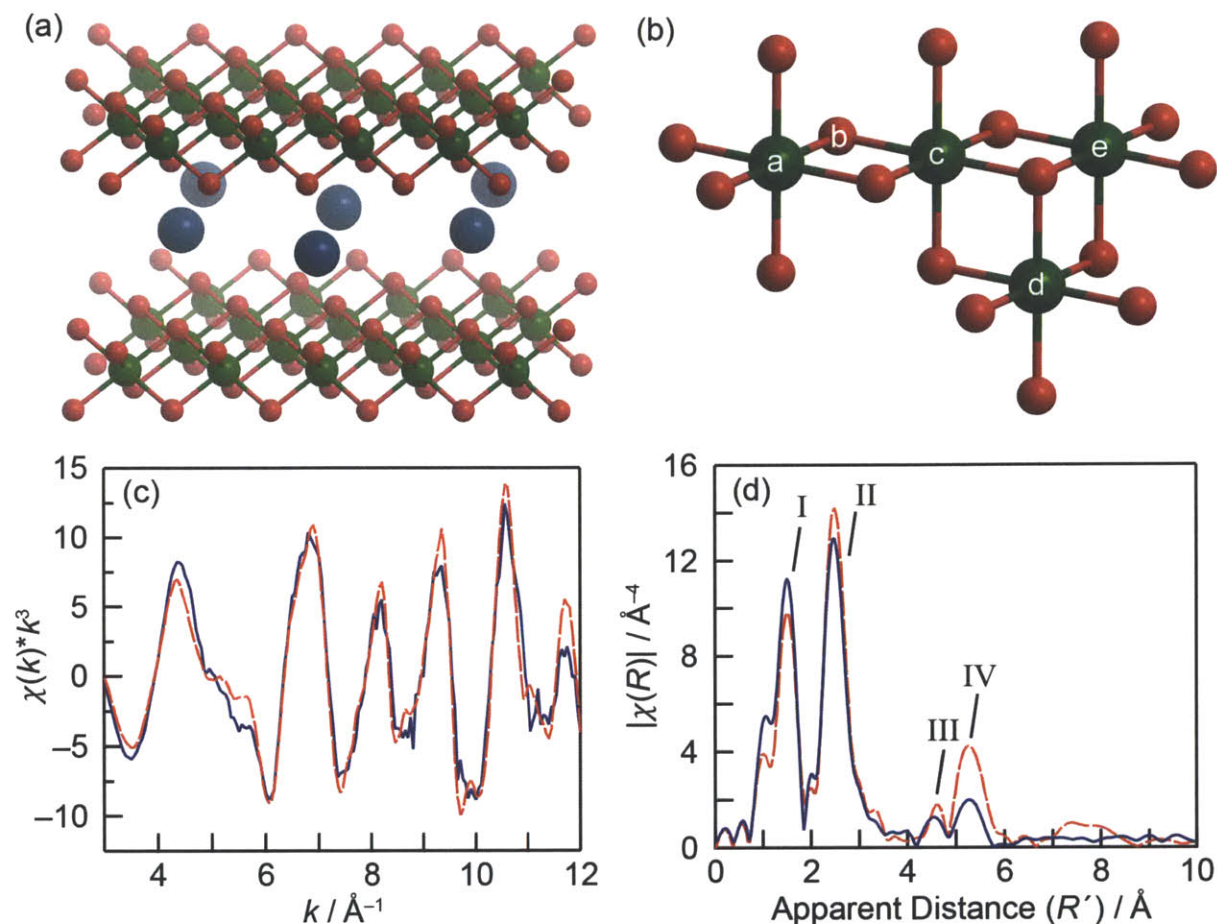


Figure 2.4. (a) X-ray crystal structure of γ -NiOOH, showing nickel (green), oxygen (red) and sodium (blue) ions. Water molecules intercalated between the NiO₂ slabs been omitted for clarity. (b) Fragment of a general nickelate structure displaying the atoms (b, c, d, e) that lead to the relevant backscattering interactions from the absorbing atom, a. (c) k^3 -weighted EXAFS oscillations and (d) Fourier transforms of k -space oscillations for γ -NiOOH (red $---$) and anodized Ni-B_i during catalysis at 1.05 V (blue $—$).

In particular, peak IV, corresponding to longer range interactions (path a–e) is suppressed significantly in the FT EXAFS spectrum of the catalyst film as compared to what is found in the case of the crystalline γ -NiOOH. Spectra of the anodized catalyst films held at 1.05 and 1.15 V displayed marginal differences, with slightly higher overall EXAFS intensities observed when the film is polarized at higher potential (Figure 2.5a). When an anodized catalyst film is reduced to Ni(II) by maintaining the potential at 0.4 V, the EXAFS spectrum becomes similar to that of the Ni(OH)₂ with longer Ni–O and Ni–Ni distances (Figure 2.5b).

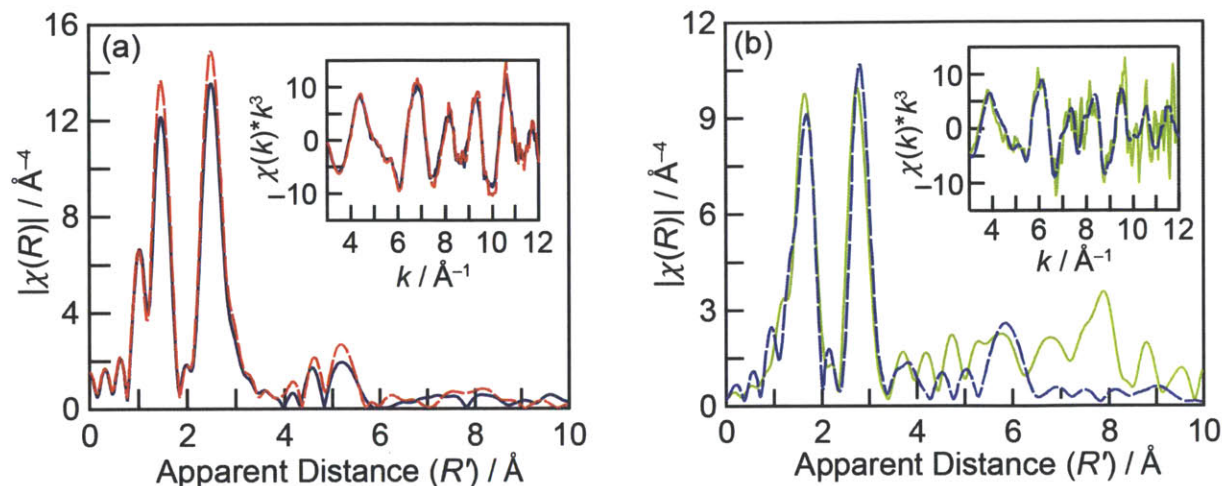


Figure 2.5. FT EXAFS spectra and k^3 -weighted EXAFS spectra (inset) of (a) an anodized Ni-B_i catalyst film maintained at 1.05 V (dark blue —) and 1.15 V (red —) and (b) Ni(OH)₂ (blue —) and an anodized Ni-B_i catalyst film held at 0.4 V (yellow —).

The EXAFS curve fitting was first carried out for γ -NiOOH based on its known crystal structure, by including absorber-backscatterer vectors ≤ 5.8 Å in length and fixing the number of neighbors in each shell (N values) to values determined from the crystal structure (6.0 in each case).^{21,34} Figure 2.6 shows the k -space and FT spectra of the best fit, and Table 2.2 summarizes the fitting parameters. The actual distances (R) of the EXAFS fits are in good correspondence with the crystallographic distances of γ -NiOOH. With these results in hand for the model compound, the fit of the experimental spectrum of anodized Ni-B_i was produced (Figure 2.7). In

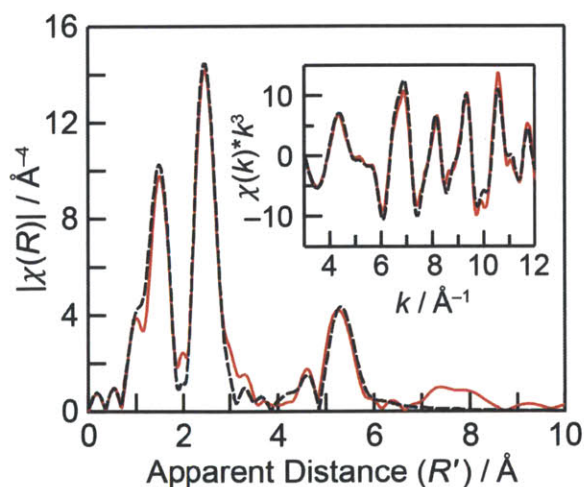


Figure 2.6. Fit (black —) to EXAFS spectrum of γ -NiOOH (red —). The inset shows the corresponding k^3 -weighted oscillations. Fit parameters are indicated in Table 2.2.

Table 2.2. γ -NiOOH EXAFS Fitting Parameters^a

Path	$R / \text{\AA}$		N^b	$\sigma^2 / \text{\AA}^{-2}$	$\Delta E^0 / \text{eV}$	$R_f / \%$
	XRD	EXAFS				
Ni–O	1.90	1.88 (0.01)	6.0	0.007 (0.001)	2.3	3.4
Ni–Ni	2.83	2.82 (0.01)	6.0	0.006 (0.001)		
Ni–Ni	4.90	4.88 (0.04)	6.0	0.012 (0.005)		
Ni–Ni ^c	5.66	5.70 (0.01)	6.0	0.004 (0.001)		

^a Fitting region $1 \leq R / \text{\AA} \leq 6$, $2.9 \leq k / \text{\AA}^{-1} \leq 11.9$. Values in parentheses indicate uncertainties. See Supporting Information for details. ^b Fixed values. ^c Multiple scattering path (a–e; Ni–Ni–Ni)

order to estimate a lower-limit domain size, the Debye-Waller factors (σ^2), were fixed to the values obtained from γ -NiOOH EXAFS curve fitting (Table 2.2), and the N values were optimized for the best fit. We consider these σ^2 values to be a reasonable lower-limit because static disorder is expected to be lower in the crystalline γ -NiOOH compound relative to Ni–B_i. The resulting fit, which is displayed in Figure 2.7, returns an N value for the Ni–Ni vector (with $R = 2.82 \text{\AA}$) of ~ 5 . Much weaker peaks arising from interactions at distances $> 3 \text{\AA}$ (peaks III and IV) also suggests a less-ordered structure or smaller cluster size in the Ni–B_i film compared to the crystalline γ -NiOOH compound. A *lower-limit* domain size consisting of ~ 40 Ni ions for the seemingly amorphous catalyst film is estimated from this Ni–Ni N value.

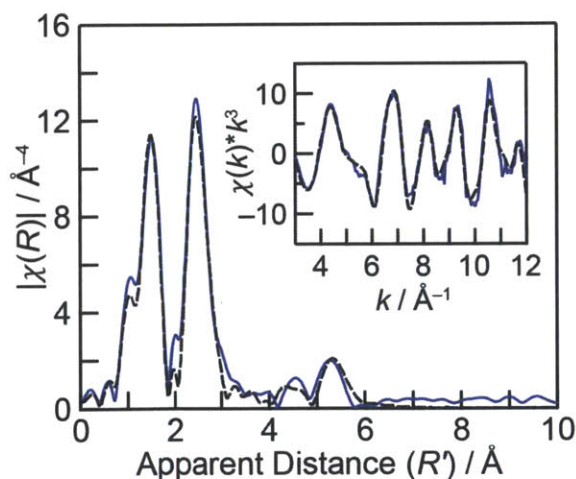


Figure 2.7. Fit (black —) to EXAFS spectrum of anodized Ni–B_i at 1.05 V (blue —). The inset shows the corresponding k^3 -weighted oscillations. Fit parameters are indicated in Table 2.3.

Table 2.3. Anodized Ni–B_i Catalyst EXAFS Fitting Parameters^a

Path	$R / \text{\AA}$	N	$\sigma^2 / \text{\AA}^{-2}{}^b$	$\Delta E^0 / \text{eV}$	$R_f / \%$
Ni–O	1.89 (0.01)	5.9 (0.)	0.007	3.3	3.1
Ni–Ni	2.82 (0.01)	5.1 (0.3)	0.006		
Ni–Ni	4.86 (0.07)	4.1 (3.2)	0.012		
Ni–Ni ^c	5.70 (0.03)	2.7 (1.1)	0.004		

^a Fitting region $1 \leq R / \text{\AA} \leq 6$, $2.8 \leq k / \text{\AA}^{-1} \leq 11.8$. Values in parentheses indicate uncertainties. See Supporting Information for details. ^b The σ^2 values were set to the values obtained from γ -NiOOH curve fitting. ^c Multiple scattering path (a–e; Ni–Ni–Ni).

EXAFS data were collected on a non-anodized Ni–B_i film poised at 1.0 V to provide insight into the local structure of the catalyst film in its initially-deposited, less catalytically active state. β -NiOOH was considered a preliminary model compound for such films, since it displayed the closest mean Ni oxidation state (Figures 2.2 and 2.3b). Figure 2.8 compares the EXAFS spectrum of a non-anodized Ni–B_i film to that of its anodized congener and β -NiOOH. The EXAFS FT of a non-anodized Ni–B_i film presents peaks at distances similar to those of anodized films; yet with much lower intensities (Figure 2.8). The peak intensities for β -NiOOH are lower than those of either Ni–B_i film. For both NaNiO_2 and β -NiOOH, the best fits (Tables

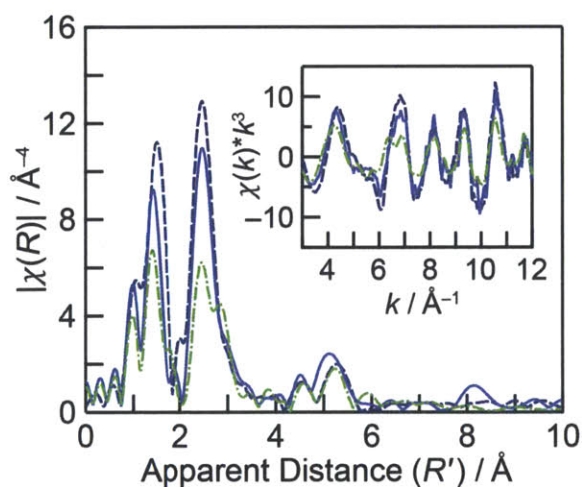


Figure 2.8. EXAFS FT spectra for non-anodized Ni–B_i poised at 1.0 V (blue —), anodized Ni–B_i poised at 1.05 V (dark blue - -), and β -NiOOH (green - · - ·). The inset shows the corresponding k^3 -weighted oscillations.

2.4 and 2.5) were obtained by considering two distinct sets of distances for the first and second shell vectors that reflect a Jahn–Teller distortion (Figure 2.9).^{22,23}

With β -NiOOH, the best fit to the EXAFS spectrum yields a ratio of long and short Ni–O interaction numbers of 3.9 to 2.1, which is similar to the 4:2 ratio expected from the Jahn-Teller

Table 2.4. NaNiO₂ EXAFS Curve Fitting Parameters^a

Fit No.	Path	R / Å	N	$\sigma^2 / \text{Å}^{-2c}$	$\Delta E^0 / \text{eV}$	$R_f / \%$
1	Ni–O	1.90 (0.02)	6.0 ^b	0.015 (0.002)	1.8	6.6
	Ni–Ni	2.87 (0.02)	6.0 ^b	0.013 (0.001)		
2	Ni–O	1.92 (0.01)	4.0 (0.4) ^c	0.008 (0.002) ^e	6.1	1.0
	Ni–O	2.19 (0.04)	2.0 (0.4) ^c	0.008 (0.002) ^e		
	Ni–Ni	2.90 (0.01)	4.4 (0.4) ^d	0.008 (0.001) ^f		
	Ni–Ni	3.15 (0.03)	1.6 (0.4) ^d	0.008 (0.001) ^f		

^a Fitting region $1.2 \leq R / \text{Å} \leq 3.2$, $2.69 \leq k / \text{Å}^{-1} \leq 12.60$. Values in parentheses indicate uncertainties (see page S2). ^b fixed values. ^{c,d} Sum of the N values for the short and long interactions were fixed to 6. ^{e,f} σ^2 values were set to be equal for the short and long interactions.

Table 2.5. β -NiOOH EXAFS Curve Fitting Parameters^a

Fit	Path	R / Å	N	$\sigma^2 / \text{Å}^{-2}$	$\Delta E^0 / \text{eV}$	$R_f / \%$
1	Ni–O	1.92 (0.03)	6.0 ^b	0.013 (0.002)	–0.3	17.7
	Ni–Ni	2.82 (0.04)	6.0 ^b	0.017 (0.003)		
2	Ni–O	1.92 (0.05)	3.9 (0.5) ^c	0.007 (0.002) ^d	5.1	2.6
	Ni–O	2.12 (0.05)	2.1 (0.5) ^c	0.007 (0.002) ^d		
	Ni–Ni	2.86 (0.02)	3.3 (0.2) ^c	0.006 (0.001) ^d		
	Ni–Ni	3.09 (0.02)	2.7 (0.2) ^c	0.006 (0.001) ^d		

^a Fitting region $1.0 \leq R / \text{Å} \leq 3.6$, $2.55 \leq k / \text{Å}^{-1} \leq 12.52$. Values in parentheses indicate uncertainties (see page S2). ^b fixed values. ^c Sum of the N values for the short and long interactions were fixed to 6. ^d σ^2 values were set to be equal for the short and long interactions.

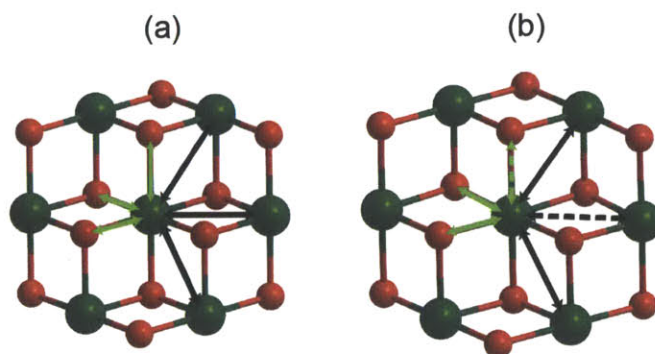


Figure 2.9. Models of the first and second shell scattering paths in (a) a structure where all Ni–O (lime green) and Ni–Ni (black) paths are equivalent, such as that found in γ -NiOOH and (b) a Jahn-Teller distorted structure where there exists two sets of non-equivalent Ni–O (lime green) and Ni–Ni (black) distances, such as that found in β -NiOOH or NaNiO_2 .

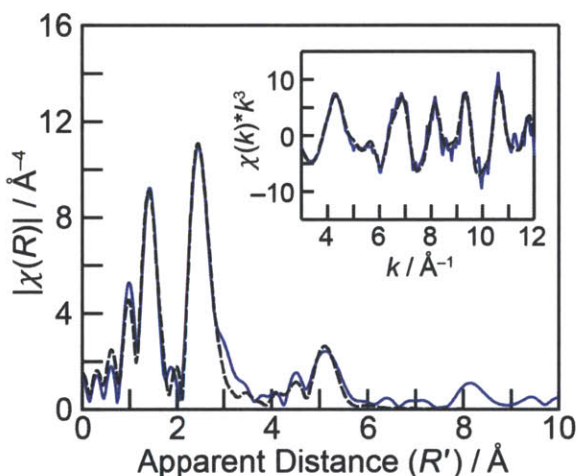


Figure 2.10. Fit (black —) to EXAFS spectrum of non-anodized Ni–Bi poised at 1.0 V (blue —). The inset shows the corresponding k^3 -weighted oscillations. Fit parameters are indicated in Table 2.6.

distortion. An excellent fit was obtained for the non-anodized film (Figure 2.10) with a ratio of long and short Jahn–Teller distorted vectors of about 4:2 (Table 2.6: Fit 1). Importantly, the fit quality suffers appreciably ($R_f = 7.1$ vs. 2.0 %) when only a single path is considered for the first and second shell vectors (Table 2.6: Fit 2). These fitting results point to a distortion in the local coordination geometry about Ni centers in non-anodized Ni–Bi films, as found in β -NiOOH and NaNiO_2 .

Table 2.6. Non-Anodized Ni–B_i Curve Fitting Parameters^a

Fit	Path	$R / \text{\AA}$	N	$\sigma^2 / \text{\AA}^{-2}$	$\Delta E^0 / \text{eV}$	$R_f / \%$
1	Ni–O	1.90 (0.01)	4.0 (0.4) ^c	0.003 (0.001) ^d	5.7	2.0
	Ni–O	2.10 (0.03)	2.0 (0.4) ^c	0.003 (0.001) ^d		
	Ni–Ni	2.83 (0.01)	4.6 (0.35) ^c	0.005 (0.001) ^d		
	Ni–Ni ^d	3.05 (0.03)	1.4 (0.35) ^c	0.005 (0.001) ^d		
2	Ni–O	1.92 (0.01)	6.0 ^b	0.001 (0.001)	2.5	7.1
	Ni–Ni	2.81 (0.01)	6.0 ^b	0.008 (0.001)		

^a Fitting region $1.0 \leq R / \text{\AA} \leq 3.6$, $2.55 \leq k / \text{\AA}^{-1} \leq 12.52$. Values in parentheses indicate uncertainties (see page S2). ^b fixed values. ^c Sum of the N values for the short and long interactions were fixed to 6. ^d σ^2 values were set to be equal for the short and long interactions.

2.3. Discussion

A Ni–B_i catalyst film requires a pre-electrolysis regimen following electrodeposition to obtain high OER activities. Over the course of this anodization, the efficiency of Ni–B_i films in mediating the OER is enhanced by greater than 2 orders of magnitude as indicated by Figure 2.1. This drastic improvement in catalytic activity is reflected in the prominence of the catalytic wave in CVs of anodized films compared to the diminished catalytic wave at identical potentials in non-anodized films (Figure 2.2). Narrower and more symmetric voltammetric peak shapes for CVs of anodized catalyst films indicate that the anodization process results in greater homogeneity in the nickel oxidation potential. The rate of anodization is sensitive to the electrolyte concentration (Figure 2.1a vs. Figure 2.1c). By using low electrolyte concentrations, we have been able to retard anodization to the extent that over the time course of XAS data collection, we are able to monitor, *in situ*, the structural and oxidation state changes that accompany anodization and the attendant increase in catalytic activity.

2.3.1 Nickel Oxidation State Changes in Ni-B_i

Coulometric and XANES studies corroborate the average oxidation state of nickel in Ni-B_i for anodized and non-anodized films subjected to various potentials. For both anodized and non-anodized films, polarization at potentials well below the onset potential for water oxidation catalysis (0.4 V) induces complete reduction of the nickel centers to the +2 oxidation state (Figure 2.2). Conversely, anodized films polarized at 1.0 V, a potential at which oxygen evolution catalysis occurs, exhibit a mean oxidation state of +3.6 (Figures 2.2 and 2.3a, Table 2.1), whereas non-anodized films, held at the same potential, exhibit a mean oxidation state of +3.16 (Figures 2.2 and 2.3b). Thus the process of anodization increases the fraction of Ni(IV) centers in the film by at least a factor of 3 (from 20% to 60%) over the course of 4 h (Figure 2.2). Coulometric studies establish that the vast majority of this oxidation state change occurs within the first hour of anodization (Figure 2.2). This time window corresponds qualitatively to the time scale over which the vast majority of increase in OER activity is observed (Figure 2.1a). The similar time course observed for activity and oxidation state increases points to a strong correlation between the two properties.

The increase in nickel oxidation state from +3.16 to +3.6 is concordant with the oxidation state change observed for phase conversion of β -NiOOH to γ -NiOOH. Importantly, polarization of the anodized Ni-B_i films beyond 1.0 V, up to a potential of 1.15 V, does not engender any further increase in the average formal oxidation state of nickel centers despite the fact that this same increase in potential corresponds to a three order of magnitude increase in the rate of OER catalysis.¹ Together, these results establish that an increase in the Ni(IV) population in the catalyst resting state is correlated with an increase in overall activity. Moreover, because there is no detectable change in the XANES edge shift of anodized films (Figure 2.3b inset) between 1.0 and 1.15 V, the mechanism of action of catalytically active sites in the anodized film likely involves a further minor-equilibrium, possibly from Ni(III) resting states to Ni(IV) catalytic intermediates.

2.3.2 Anodization-Induced Structural Changes in Ni-B_i

The similarities between crystalline γ -NiOOH and anodized Ni-B_i catalyst films in terms of XANES edge position, formal nickel oxidation state and EXAFS spectra indicate that γ -NiOOH is an appropriate model compound for the structure of anodized Ni-B_i catalyst films. In γ -NiOOH, edge-sharing NiO₆ octahedra are arranged into higher-order layers, which are interstratified with alkali cations and water molecules (Figure 2.4a). EXAFS spectra of anodized Ni-B_i catalyst films exhibit a first shell Ni-O vector at 1.89 Å and a nearest-neighbor Ni-Ni vector at 2.82 Å associated with the presence of Ni-oxo/hydroxo structural units similar to those found in γ -NiOOH (Figure 2.4b-d). The γ -NiOOH structure is differentiated from β -NiOOH (and NaNiO₂) by a Jahn-Teller distortion of the low-spin d⁷ Ni(III) centers of the latter, which gives rise to an axial elongation and equatorial contraction of the oxygen ion ligand field producing a 2:1 ratio of Ni-O scattering vectors of 1.87 and 2.03 Å, respectively (Figure 2.9, Table 2.5).²³ This Jahn-Teller distortion in β -NiOOH results in two effects that distinguish its EXAFS spectrum from γ -NiOOH (and anodized Ni-B_i): (i) a drastic diminution in the intensity and (ii) broadening of the first and second shell scattering peaks arising from their poorly resolved splitting into two separate sets of peaks corresponding to a ~4:2 ratio of short equatorial and long axial vectors respectively about each Ni(III) center. The sharp peaks observed for the first and second shell of Ni-Ni and Ni-O scattering vectors in the experimental spectrum of anodized Ni-B_i are similar to the peak profiles of γ -NiOOH, and thus the local coordination geometry of anodized Ni-B_i is akin to γ -NiOOH and not a Jahn-Teller distorted Ni(III) phase, such as β -NiOOH or NaNiO₂.

Whereas anodized Ni-B_i is structurally analogous to γ -NiOOH, non-anodized Ni-B_i has an EXAFS spectrum that is more similar to a Jahn-Teller distorted Ni(III) phase. A good fit to the non-anodized Ni-B_i spectrum (Figure 2.10) is obtained with a long to short axis ratio of 4.0 to 2.0 for the Ni-O vectors (Table 2.6), the ratio we expect for a Ni(III) compound. A slightly greater formal nickel oxidation state (+3.16) was determined from coulometric measurements,

and correspondingly the XANES edge position is 0.8 eV higher relative to that of β -NiOOH (Figure 2.3b). These EXAFS results point to a local structural change upon anodization of Ni-B_i that resembles phase conversion of β -NiOOH to γ -NiOOH.

While the nickelate layers of β -NiOOH and γ -NiOOH stack preferentially, we were unable to identify any interactions due to interlayer backscattering in either model compound or catalyst film. However, given the large intersheet distance (~ 7 Å) in γ -NiOOH³⁴ such interactions are expected to be too weak to resolve in EXAFS spectra, and would be anticipated to be even weaker in the case of the more disordered catalyst material. Despite the inability to detect any interlayer scattering interactions by EXAFS some degree of stacking of the sheet-like domains of Ni-B_i is evident. The electrolyte concentration dependence of the rate of anodization (Figure 2.1a vs. 2.1c) provides experimental evidence in support of this contention. Cation intercalation is a critical requirement for the formation of γ -NiOOH from the alkali cation-free β -NiOOH.²⁴ The intercalation of K⁺ ions between the NiO₂ sheets in Ni-B_i films during anodization, may explain the observed electrolyte-dependence. Thus, increasing the buffer strength, and correspondingly the K⁺ ion activity, would be expected to enhance the rate of activation, provided that the domains of Ni-B_i are stacked to some degree.

The size of the ordered domains in anodized Ni-B_i may be estimated from the N values obtained from curve fitting (Figure 2.7, Table 2.3) of EXAFS spectra. The diminished longer-range interactions (at distances >3 Å) in FT EXAFS spectra, compared to an extended solid (Figure 5b, — — vs. —), suggests a nanocrystallite model as does the inability to detect crystallites by X-ray diffraction methods. From the N -value for the Ni-Ni vector of ~ 5.1 (Table 2.3), we estimate that the smallest ordered domains in catalyst films are 2–3 nm in diameter. Thus, a simplified hexagonal cluster model is constructed with ordered domains of ~ 40 Ni centers (Figure 2.11) as a reasonable lower-limit average structural model for Ni-B_i catalyst films. We, therefore, rationalize that our Ni-B_i electrosynthesis method is giving us access to such nanocrystalline oxides as uniform ultrathin films at intermediate pH.

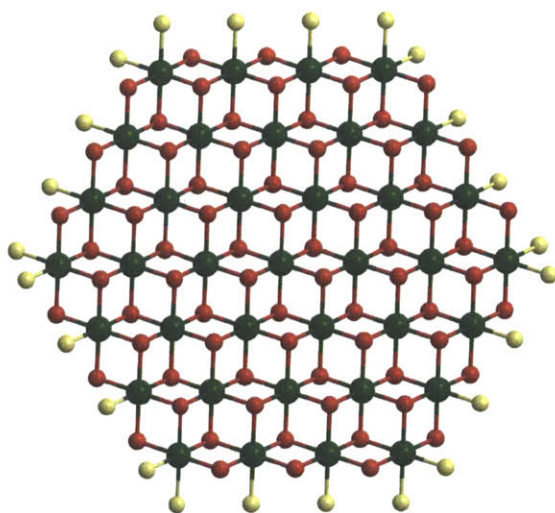


Figure 2.11. Lower-limit structural model for the average domain size of Ni-B_i. The Ni ions are shown in green, bridging oxo/hydroxo ligands are shown in red, and non-bridging oxygen ligands, which may include water, hydroxide, phosphate, or borate, are shown in pale green.

2.4 Conclusion

Anodization of electrodeposited films, which results in an almost three orders of magnitude improvement in catalyst activity, is accompanied by an increase in average nickel oxidation state to Ni(IV) and alteration of the structure of the nickel centers of electrodeposited ultrathin Ni-B_i catalyst films. A significant positive shift in the XANES edge to a position indicative of substantial formal Ni(IV) valency is observed, and EXAFS spectra indicate the presence of μ -oxo/hydroxo nickel centers organized into higher-order domains of edge sharing NiO₆ octahedra. As-deposited, Ni-B_i films display evidence for a Jahn–Teller distorted coordination geometry about the predominantly Ni(III) centers, reminiscent of the short-range structure of β -NiOOH. In contrast, anodized films possess short-range structural parameters akin to the mixed-valent γ -NiOOH phase. Thus, XAS spectra reveal that the short-range structure of anodized Ni-B_i is similar to γ -NiOOH and that of non-anodized Ni-B_i is similar to β -NiOOH. Electrochemical, XANES, and EXAFS data point to a conversion of local structure and nickel oxidation state in Ni-B_i films upon anodization that correlate to a dramatic enhancement in catalytic activity for O₂ evolution. By analogy of Ni-B_i to NiOOH, the results for Ni-B_i suggest

that active sites of γ -NiOOH may be *intrinsically* more active towards the OER than those of β -NiOOH. In particular, the vast majority of studies of alkaline water oxidation mediated by nickel oxides have been conducted using nickel metal anodes^{18,19,25–29} upon which an oxide coating is formed via electrochemical polarization. Since the surface oxide coating may grow substantially (up to 1.4 μm) during OER,^{18,25} the charge transport properties of the compact oxide layer are invariably convoluted with the kinetics of the OER at surface exposed active sites.^{30–33} Indeed, gradual deactivation of nickel anodes over time during alkaline OER, particularly when held at high overpotentials ($\eta \sim 600$ mV), has long been assigned to the formation of catalytically inert Ni(IV) centers within the surface oxide, leading to the contention that the all Ni(III) phase, β -NiOOH, is the most catalytically active nickel anode material for mediating the OER.^{18,19,25} In line with our observation for Ni-B_i, we propose the converse: that a predominantly Ni(IV) population, such as that found in the more highly oxidized γ -NiOOH-like structure is paramount to high OER activity. In our systems, Ni-B_i films are formed from solution precursors onto electrically conductive, oxidatively robust substrates, excluding interference from electron transport limitations, thus permitting isolation of the requirements for intrinsically efficient active site turnover. To this end, the results reported herein stand at odds with prevailing dogma concerning nickel oxide based OER in alkaline media.

2.5 Experimental Methods

Catalyst Electrodeposition, Anodization and Electrochemistry. Ni-B_i films were prepared on fluorine tin oxide (FTO) coated glass slides (Hartford Glass) by controlled potential electrolysis at 1.15 V (*vs.* NHE; all potentials hereafter are given *vs.* the normal hydrogen electrode) of a quiescent 0.1 M potassium borate electrolyte, pH 9.2, (0.1-B_i) containing 0.40 mM Ni²⁺. A total charge of 1.0 mC/cm² was passed during deposition. An Ag/AgCl reference electrode and Pt mesh counter electrode were used for all electrochemical experiments. Following deposition, films were anodized in stirred 1.0 M KB_i electrolyte, pH 9.2 (1.0-B_i), by application of 1.1 V to catalyst films (with correction for ohmic potential losses) for 2.5 h. This

preconditioning was also performed in 0.1-B_i on an independently deposited film. Non-anodized films were electrodeposited under identical conditions.

Cyclic voltammograms (CVs) were performed on electrodeposited films that were anodized in 1.0-B_i for times between 0 (non-anodized) and 4 h. The films were transferred immediately, without drying, to fresh 1.0-B_i. The electrode potential was maintained at 1.0 V for 30 s before scanning the CV from 1.0 V to lower potentials at a scan rate of 100 mV/s.

Film valency was determined coulometrically. Following electrodeposition and anodization, films were poised at 1.0 V for 300 s after which the potential was immediately swept from 1.0 V to 0.2 V and back to 1.2 V at 100 mV/s with compensation for ohmic potential losses. The cumulative charge passed during the scan was recorded; the amount of charge consumed in the reduction of nickel centers in the film was determined by subtracting the background charge passed by a 1 cm² FTO electrode (no catalyst coating) under identical conditions. Films were immediately removed from the electrolyte, allowed to dry in air, and subsequently dissolved in 5.00 mL of 2% aqueous nitric acid (Fluka Analytical, TraceSelect). Samples were analyzed for nickel content by Quadrupole Inductively Coupled Plasma Mass Spectrometry (Elemental Analysis, Inc., Lexington, KY).

Model Ni Compounds. NaNiO₂ was prepared by annealing NiO and Na₂O₂ (Aldrich) in a flow of O₂ according to a previously published procedure.³⁴ γ-NiOOH was prepared by treating NaNiO₂ with 5 mole equivalents of Br₂ in acetonitrile.³⁴ β-NiOOH was prepared by treating a suspension of Ni(OH)₂ in 3 M aqueous KOH with 0.7 mole equivalents of Br₂. The identity and purity of each compound were verified by powder X-ray diffraction. Ni(OH)₂, Br₂, and K₂Ni(H₂IO₆)₂ were purchased from Aldrich.

Catalyst Preparation for *in situ* XAS. A glass electrochemical cell consisting of two compartments separated by a porous frit was employed for *in situ* spectroscopic experiments. The working compartment possessed flat walls (~2.5 cm wide) with a single circular hole, 1.5 cm in diameter. A 3 cm × 2 cm slip of ITO-coated polyethylene terephthalate (Kintec Company)

was affixed with epoxy glue to the exterior of the wall of the cell, over the 1.5-cm hole, with the ITO layer ($\sim 0.15 \mu\text{m}$ thick) facing inwards. This ITO surface served as the substrate for electrodeposition of Ni-B_i films. The cell was connected to the potentiostat by making electrical contact to a portion of the ITO slip that protruded from the side of the working compartment. A Teflon cap containing a hole for the reference electrode was used to cover the working compartment and to ensure a fixed distance between working and reference electrodes between experiments.

Electrodeposition of catalyst for XAS experiments was terminated after passing 1.0 mC/cm^2 . The cell was emptied of electrolyte and rinsed twice with water (18 M Ω resistivity, EMD Millipore). For anodized films, the electrochemical cell was charged with 1.0-B_i, and anodization was carried out at 1.3 V with stirring and without compensation for ohmic potential losses over a period of 3 h, after which spectra were collected over a range of applied potentials between 1.0 and 1.15 V. For non-anodized films, the electrochemical cell was refilled with 0.1-B_i after deposition and spectra were acquired at 1.0 V.

XAS Data Collection and Analysis. XAS spectra were collected at the Stanford Synchrotron Radiation Lightsource (SSRL) on beamline 7-3 at an electron energy of 3.0 GeV with an average current of 300 mA and at the Advanced Light Source (ALS) on beamline 10.3.2 at an electron energy of 1.9 GeV with an average current of 500 mA. At beamline 7-3 (SSRL), the radiation was monochromatized by a Si(220) double-crystal monochromator. The intensity of the incident X-ray was monitored by an N₂-filled ion chamber (I₀) in front of the sample. Model compound solid samples were diluted in boron nitride (1% w/w) and placed in an aluminum sample holder sealed with kapton tape. Data were collected as fluorescence excitation spectra with a Ge 30 element detector (Canberra). For model compounds, energy was calibrated by the first peak maximum of the first derivative of a nickel foil (8333.0 eV). The standard was placed between two N₂-filled ionization chambers (I₁ and I₂) after the sample. At beamline 10.3.2 (ALS), the radiation was monochromatized by a

Si(111) double-crystal monochromator. Intensity of the incident X-ray was monitored by an N₂-filled ion chamber (I₀) in front of the sample. Fluorescence spectra were recorded by using a seven-element Ge detector array (Canberra). For electrochemical experiments, no transmission data could be collected. The energy was therefore calibrated using a glitch in the I₀ intensity. All data were collected at room temperature.

Data reduction of the EXAFS spectra was performed using EXAFSPAK (Drs. Graham George and Ingrid Pickering, SSRL). Pre-edge and post-edge backgrounds were subtracted from the XAS spectra, and the results were normalized with respect to edge height. Background removal in *k*-space was achieved through a five-domain cubic spline. Curve fitting was performed with Artemis and IFEFFIT software using *ab initio*-calculated phases and amplitudes from the program FEFF 8.2.^{35,36} These *ab initio* phases and amplitudes were used in the EXAFS equation:

$$\chi(k) = S_0^2 \sum_j \frac{N_j}{kR_j^2} f_{eff_j}(\pi, k, R_j) e^{-2\sigma_j^2 k^2} e^{-2R_j/\lambda_j(k)} \sin(2kR_j + \phi_{ij}(k)) \quad (1)$$

The neighboring atoms to the central atom(s) are divided into *j* shells, with all atoms with the same atomic number and distance from the central atom grouped into a single shell. Within each shell, the coordination number *N_j* denotes the number of neighboring atoms in shell *j* at a distance of *R_j* from the central atom. *f_{eff_j}*(*π, k, R_j*) is the *ab initio* amplitude function for shell *j*, and the Debye-Waller term *e^{-2σ_j²k²}* accounts for damping due to static and thermal disorder in absorber-backscatterer distances. The mean free path term *e^{-2R_j/λ_j(k)}* reflects losses due to inelastic scattering, where *λ_j(k)* is the electron mean free path. The oscillations in the EXAFS spectrum are reflected in the sinusoidal term, *sin(2kR_j + φ_{ij}(k))* where *φ_{ij}(k)* is the *ab initio* phase function for shell *j*. *S₀²* is an amplitude reduction factor due to shake-up/shake-off processes at the central atom(s). The EXAFS equation was used to fit the experimental data using *N*, *R*, and the EXAFS

Debye-Waller factor (σ^2) as variable parameters. For the energy (eV) to wave vector (k , \AA^{-1}) axis conversion, E_0 was defined as 8340 eV and the S_0^2 value was fixed to 0.83.³⁷

EXAFS Curve Fitting. The goodness of the fit was evaluated by the EXAFS R-factor (R_f) that represents the absolute difference (least-square fit) between theory and data.^{38,39} For evaluation among different models, the reduced χ^2 (c_n^2) was used:

$$\chi_v^2 = \chi^2 / (N_{\text{idp}} - N_{\text{var}})$$

where N_{idp} is the number of independent points in the measurement, and N_{var} is the number of variable parameters in the fit. χ^2 is defined by the following equation:

$$\chi^2 = \frac{N_{\text{idp}}}{N_{\text{pts}} \epsilon_k^2} \sum_i^{N_{\text{pts}}} [\chi_i^{\text{data}} - \chi_i^{\text{calc}}]^2$$

where ϵ_k is the measurement uncertainty in k -space, and N_{pts} is the number of points in the fitting range of the data. The measurement uncertainty was estimated by the root-mean-square (rms) average of $c(R)$ between 15 and 25 \AA as described in the literature.⁴⁰ The uncertainty in the variables, scaled by the square root of c_n^2 , are estimated by fitting parameters using a Fourier-filtered spectrum of a relevant R' range of absorber-backscatter distances.

Estimation of film thickness. We estimate the thickness of these films by noting that a Ni–O distance of $\sim 1.9 \text{ \AA}$ has been identified in the EXAFS studies described here, and we therefore approximate that the primary coordination sphere of each Ni center occupies a cube of volume $\sim 125 \text{ \AA}^3$. With this consideration, a monolayer of catalyst would constitute $\sim 0.7 \text{ nmol}$ of nickel centers per cm^2 of surface area, corresponding to a charge of $\sim 65 \text{ \mu C/cm}^2$. The ITO-coated substrates are not atomically smooth, and these films are expected to grow by nucleation. Therefore, the term “monolayer” in this case more aptly approximates a monolayer’s worth of material, and for such thin films, large regions of the ITO would be exposed. Bearing these qualifications in mind, we estimate a film thickness of 8 nm for a 1.0 mC/cm^2 film. A significant

amount of O₂ evolution is coincident with film deposition and, as such, the amount of Ni centers should be *less* than that expected for the passage of 1.0 mC/cm² with 100% faradaic efficiency for deposition. Indeed, we find that the amount of Ni is ~63% of the charge passed in deposition (Table 1). This analysis only accounts for a Ni–Ni interlayer distance of ~5 Å, even though the interlayer distance in γ -NiO(OH) is ~7.2 Å. Thus, 8 nm is a reasonable upper limit for the thickness of these films.

2.6 References

- (1) Dincă, M.; Surendranath, Y.; Nocera, D. G. *Proc. Natl. Acad. Sci. U.S.A.* **2010**, *107*, 10337.
- (2) Kanan, M. W.; Nocera, D. G. *Science* **2008**, *321*, 1072.
- (3) Surendranath, Y.; Dincă, M.; Nocera, D. G. *J. Am. Chem. Soc.* **2009**, *131*, 2615.
- (4) Lutterman, D. A.; Surendranath, Y.; Nocera, D. G. *J. Am. Chem. Soc.* **2009**, *131*, 3838.
- (5) Esswein, A. J.; Surendranath, Y.; Reece, S. R.; Nocera, D. G. *Energy Environ. Sci.* **2011**, *4*, 499.
- (6) Pijpers, J. J. H.; Winkler, M. T.; Surendranath, Y.; Buonassisi, T.; Nocera, D. G. *Proc. Natl. Acad. Sci. U.S.A.* **2011**, *108*, 10056.
- (7) Young, E. R.; Costi, R.; Nocera, D. G.; Bulović, V. *Energy Environ. Sci.* **2011**, *4*, 2058.
- (8) Reece, S. Y.; Hamel, J. A.; Sung, K.; Jarvi, T. D.; Esswein, A. J.; Pijpers, J. J. H.; Nocera, D. G. *Science* **2011**, *334*, 645.
- (9) Nocera, D. G. *Acc. Chem. Res.* **2012** *45*, 767.
- (10) Somorjai, G. A. *Introduction to Surface Chemistry & Catalysis*; Wiley: New York, 1994.
- (11) Thomas, J. M.; Thomas, W. J. *Principles and Practice of Heterogeneous Catalysis*; VCH: Weinheim, 1997.

- (12) Zambelli, T.; Wintterlin, J.; Trost, J.; Ertl, G. *Science* **1996**, *273*, 1688.
- (13) Jaramillo, T. F.; Jorgensen, K. P.; Bonde, J.; Nielsen, J. H.; Horch, S.; Chorkendorff, I. *Science* **2007**, *317*, 100.
- (14) Kanan, M. W.; Yano, J.; Surendranath, Y.; Dincă, M.; Yachandra, V. K.; Nocera, D. G. *J. Am. Chem. Soc.* **2010**, *132*, 13692.
- (15) Dau, H.; Limberg, C.; Reier, T.; Risch, M. Roggan, S.; Strasser, P. *ChemCatChem.* **2010**, *2*, 724.
- (16) Risch, M.; Klingan, K.; Heidkamp, J.; Ehrenberg, D.; Chernev, P.; Zaharieva, I.; Dau, H. *Chem. Commun.* **2011**, *47*, 11912.
- (17) Surendranath, Y.; Kanan, M. W.; Nocera, D. G. *J. Am. Chem. Soc.* **2010**, *132*, 16501.
- (18) Kinoshita, K. *Electrochemical Oxygen Technology*; Wiley-Interscience: New York, 1992; Ch. 2.
- (19) Lyons, M. E. G.; Brandon, M. P. *Int. J. Electrochem. Sci.* **2008**, *3*, 1386.
- (20) Bianconi, A. In *X-ray Absorption: Principles, Applications, Techniques of EXAFS, SEXAFS and XANES*; Koningsberger, D. C. and Prins, R., Eds.; Wiley: New York, 1988; pp 573–662.
- (21) Bartl, H.; Bode, H.; Sterr, G.; Witte, J. *Electrochim. Acta* **1971**, *16*, 615.
- (22) Dyer, L. D.; Borie, B. S.; Smith, G. P. *J. Am. Chem. Soc.* **1954**, *76*, 1499.
- (23) Demourgues, A.; Gautier, L.; Chadwick, A. V.; Delmas, C. *Nucl. Inst. Meth. B* **1997**, *133*, 39.
- (24) Oliva, P.; Leonardi, J.; Laurent, J. F. *J. Power Sources* **1982**, *8*, 229.
- (25) Lu, P. W. T.; Srinivasan, S. *J. Electrochem. Soc.* **1978**, *125*, 1416.

- (26) Conway, B. E.; Liu, T. *J. Chem. Soc., Faraday Trans. 1*, **1987**, 83, 1063.
- (27) Conway, B. E.; Liu, T. *C. Mater. Chem. Phys.* **1989**, 22, 163.
- (28) Lyons, M. E. G.; Brandon, M. P. *Int. J. Electrochem. Sci.* **2008**, 3, 1386.
- (29) Kinoshita, K. *Electrochemical Oxygen Technology*; Wiley-Interscience: New York, 1992; Ch. 2.
- (30) Surendranath, Y.; Nocera, D. G. *Prog. Inorg. Chem.* **2011**, 57, 505.
- (31) MacDonald, J. J.; Conway, B. E. *Proc R. Soc. London*, **1962**, 269, 419.
- (32) Damjanovic, A.; Jovanovic, B. *J. Electrochem. Soc.* **1976**, 123, 374.
- (33) Lyons, M. E. G.; Brandon, M. P. *Int. J. Electrochem. Sci.* **2008**, 3, 1425.
- (34) Yang, X.; Takada, K.; Itose, M.; Ebina, Y.; Ma, R.; Fukuda, K.; Sasaki T. *Chem. Mater.* **2008**, 20, 479.
- (35) Newville, M. *J. Synchrotron Rad.* **2001**, 8, 322.
- (36) Rehr, J. J.; Albers, R. C. *Rev. Mod. Phys.* **2000**, 72, 621.
- (37) Mansour, A. N.; McBreen J., Melendres, C. A. *J. Electrochem. Soc.* **1999**, 146, 2799.
- (38) Newville, M. *J. Synchrotron Rad.* **2001**, 8, 322.
- (39) Ravel, B.; Newville, M. *J. Synchrotron Rad.* **2005**, 12, 537.
- (40) Newville, M.; Boyanov, B. I.; Sayers, D. E. *J. Synchrotron Rad.* **1999**, 6, 264.

**Chapter 3 — Mechanistic Studies into Oxygen
Evolution Mediated by Nickel–Borate Electrocatalyst
Films**

3.1 Introduction

In Chapter 2 we discussed *in situ* extended X-ray absorption fine structure (EXAFS) studies that shed light on the structural connectivity of nickel and oxygen ions in the nickel-borate (Ni-B_i) oxygen evolving catalyst. Together with *in situ* X-ray absorption near edge structure (XANES) spectra of Ni-B_i films, cyclic voltammetry and coulometric titrations were helpful in uncovering the resting state nickel valency in these materials. These studies also revealed key aspects of the anodization-induced structural transformations that are correlated with drastic improvements in catalytic activity (ca. 3 orders of magnitude).¹

We now report the OER kinetic profile of Ni-B_i films over a wide pH range (8.5–14) and divulge mechanistic insights into the origin of the considerable activity enhancement that is attendant to anodization. The electrosynthesis of ultrathin OEC films (≤ 15 monolayers) enable us to avoid internal electronic or ionic transport barriers. Our studies have enabled us to uncover a unique OER mechanism that stands in contrast to frequently invoked OER mechanisms of nickel oxide anodes.^{2–10} Furthermore, we find that the apparent specific activity of Ni-B_i films is significantly greater than that found in Co-B_i systems of comparable catalyst loading for pH > 7. However, the same pH-dependent profiles cause Co-B_i to supersede Ni-B_i in activity for pH ≤ 7 . By defining the nature of the proton-coupled electron transfer (PCET) pre-equilibrium that occurs during turnover, we find that trends in catalyst activity may be completely reversed at intermediate pH as compared to those at pH extremes. The results presented herein highlight the need for a detailed mechanistic understanding of OER for the construction of direct solar-to-fuels devices that operate at high efficiencies.

3.2 Results

3.2.1 Catalyst Electrodeposition and Anodization

Catalyst films were prepared by controlled potential electrolysis of 100 mM KB(OH)₄/H₃BO₃ (B_i) electrolyte, pH 9.2 containing 0.4 mM Ni²⁺ at an applied potential of 1.15

V (vs. NHE) without stirring. Unless otherwise noted, a total charge of 1.0 mC cm^{-2} was passed during deposition over a period of 60–80 s using Fluorine–tin–oxide (FTO) coated glass slides as substrate. Following deposition, films were preconditioned with an anodization protocol that involved passage of 3.5 mA cm^{-2} for 1–2 h in stirred solutions of 1.0 M B_i electrolyte, pH 9.2.

3.2.2 Tafel slope determination.

The steady-state current density (j) for oxygen evolution from anodized films was evaluated as a function of the overpotential (η) in stirred Ni-free solutions of 0.5 M B_i pH 9.2 electrolyte (Figure 3.1). To avoid diffuse double layer effects,¹¹ a high ionic strength was maintained with 1.75 M KNO_3 supporting electrolyte. The applied voltage (E_{appl}) was varied in 7–20 mV increments in the region of water oxidation and maintained until j attained a steady-state value. Compensation of E_{appl} for Ohmic potential losses yielded the corrected potential (E), which was then converted to η by subtraction of the thermodynamic potential for water oxidation (E°) under the experimental conditions. Steady-state polarization data were acquired following anodization of films deposited by passage of 1.0, 0.40 and 0.083 mC cm^{-2} .

The amount of charge passed in oxidation or reduction of Ni– B_i films involves a net transfer of ca. 1.6 electrons per nickel center.¹ With this knowledge, the charge consumed upon reduction of films by cyclic voltammetry permits a reliable estimation of the number of nickel centers in catalyst films (see Section 3.5) and thickness of the films.¹ Film thicknesses of approximately 5, 3 and 1 nm correspond to 15, 9 and 3 monolayer's worth of catalyst, respectively. Although the overall activity of these catalyst films at a specified overpotential increases with thickness, plots of η (or E) as a function of $\log j$ (Tafel plots) display similar slopes, b , of 30 mV/decade ($2.3 \times RT/2F$), irrespective of loading.

These Tafel slopes are indicative of a two-electron transfer in minor equilibrium prior to a chemical turnover-limiting step (TLS), resulting in a transfer coefficient, α ($\alpha = 2.3RT/bF$) of 2.^{5,12} Tafel plots of films deposited onto a Pt rotating disk electrode (RDE) are identical irrespective of the rotation rates, ω of 2000 rpm or 600 rpm, or whether stirring is the sole source

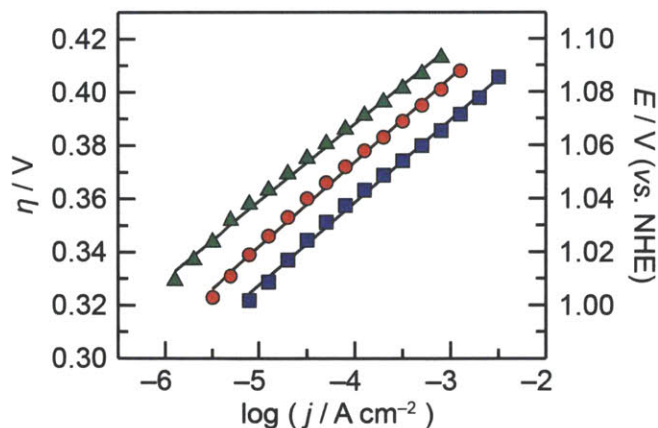


Figure 3.1. Tafel plots, $E = (E_{appl} - iR)$, $\eta = (E - E^\circ)$, for anodized catalyst films deposited onto FTO by passage of 1.0 (■), 0.40 (●), and 0.083 (▲) mC cm^{-2} and operated in 0.5 M KBi 1.75 M KNO_3 pH 9.2 electrolyte. Tafel slopes are 31, 32 and 29 mV/decade , respectively.

of convection (Figure 3.2a). These observations confirm that the Tafel slope is representative of activation-controlled OER over the potential range explored. Tafel slopes are also reproducible for sequential runs, and do not depend on the direction of potential change (Figure 3.2b), indicating that the films are not significantly altered over the course of data collection.

Although only a fraction of the nickel centers may be involved in catalysis, a lower-limit value for the oxygen evolution turnover frequency (TOF_{\min}) of Ni-Bi catalyst films at a specified overpotential can be estimated by determining the rate of turnover per nickel center in the film at that overpotential. At $\eta = 400$ mV in 0.5 M Bi pH 9.2 electrolyte, a TOF_{\min} was determined to be 0.9, 0.5 and 0.5 $\text{mol O}_2 (\text{mol Ni})^{-1} \text{s}^{-1}$ for films prepared by passage of 1.0, 0.40 and 0.083 mC cm^{-2} , respectively (see section 3.6).

Tafel slopes were also extracted from open circuit potential (E_{OC}) decay transients, following the interruption of a potential pulse. Catalyst films were poised at 1.1 V in 0.5 M Bi pH 9.2 electrolyte for 5 s. Upon switching to open circuit, the decay in E_{OC} was monitored as a function of time, t (Figure 3.3). The decrease in E_{OC} arises due to the discharge of the capacitance of the electrode, through the Faradaic resistance, mediated by the catalyst film (i.e. Ni centers in the film are reduced by water via the OER). Thus the characteristics of the

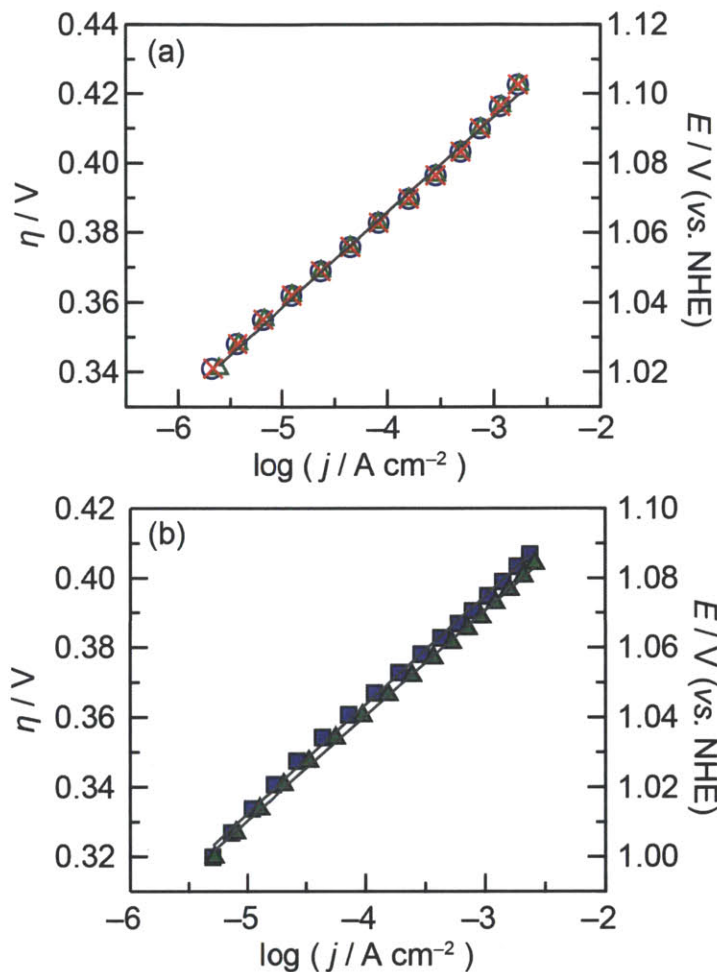


Figure 3.2. (a) Tafel plots, $E = (E_{\text{applied}} - iR)$, $\eta = (E - E^\circ)$, for a 1.0 mC cm^{-2} anodized catalyst film deposited onto a Pt RDE and operated in 0.5 M KB_i , 1.75 M KNO_3 , pH 9.2 electrolyte at 2000 (\blacktriangle), 600 (\bullet), and 0 rpm with a magnetic stirrer as the sole source of solution convection (\times). The Tafel slope of each plot is 28 mV/decade. (b) Tafel plots, $E = (E_{\text{applied}} - iR)$, $\eta = (E - E^\circ)$, for a 1.0 mC cm^{-2} anodized catalyst film deposited onto FTO and operated in 0.5 M KB_i , 1.75 M KNO_3 , pH 9.2 electrolyte in decreasing (\blacktriangle), followed immediately by increasing (\bullet) order of changing potentials. Tafel slopes are 30 and 31 mV/decade respectively.

overpotential of the electrode at open circuit ($\eta_{OC} = E_{OC} - E^\circ$) vs. time depends on the mechanism of O_2 evolution and therefore the Tafel slope, b :^{3,13,14}

$$\eta_{OC} = a - b \log(t + \tau) \quad (3.1)$$

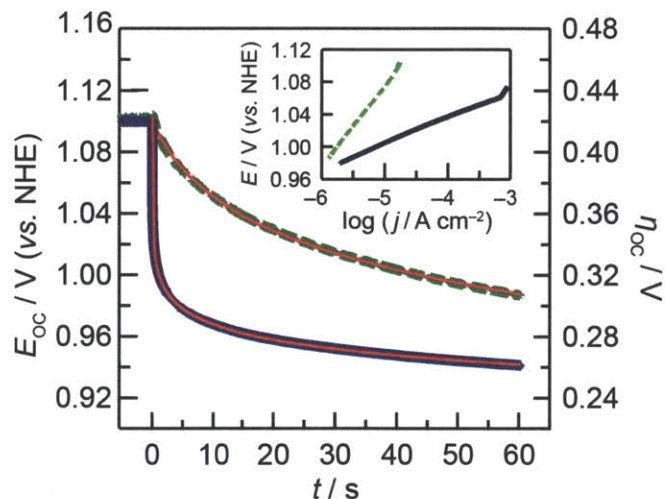


Figure 3.3. Open circuit potential, E_{OC} , and overpotential, $\eta_{OC} = (E_{OC} - E^\circ)$, transients for non-anodized (green $-\cdot-\cdot-$) and anodized (dark blue $-\cdot-$) 1.0 mC cm^{-2} NiB_i films immediately following a 10 s bias at 1.1 V in 0.5 M KB_i 1.75 M KNO₃ pH 9.2 electrolyte. The red lines represent fits to eq 1. Tafel slopes are 100 before anodization and 33 mV/decade after anodization. The inset shows the corresponding Tafel plots determined from the E_{OC} transients by calculating $\log j$ at each time point using eq 3.2.

with $a = b \log(bC/j_0)$ and $\tau = 10^{(-\eta'/b)} bC/j_0$. C is the capacitance of the electrode, j_0 is the exchange current density, and η' is the initial overpotential at $t = 0$. This open-circuit decay method assumes that any change in C during the experiment is negligible.

E_{OC} - t curves recorded for anodized and non-anodized films are shown in Figure 3.3. Owing to their considerably higher catalytic activity, the E_{OC} of anodized films decreases by almost 100 mV within the first 0.1 s after the potential is interrupted. In contrast, over the same duration a minimal decrease (< 10 mV) is observed in E_{OC} for non-anodized films. Fitting the decay trace of an anodized film to eq. 3.1 yields a Tafel slope of 33 mV/decade, which is in excellent agreement with the steady-state Tafel plot measurements of Figure 3.1. In contrast, a much higher Tafel slope of 100 mV/decade is extracted from the open circuit decay trace of non-anodized films. These transients permit the construction of Tafel plots of anodized and non-anodized films by recognizing that the instantaneous OER current density across the catalyst-electrolyte interface ($\log j_t$) can be expressed as a function of the time elapsed during the OCP

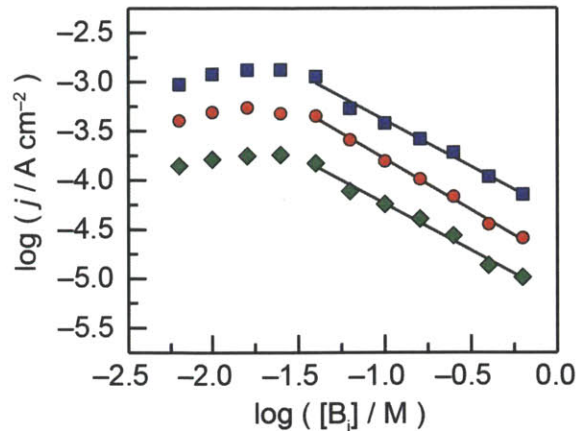


Figure 3.4. B_i concentration dependence of steady state catalytic current density at constant potential ($E = 1.04$ V (\blacklozenge), 1.05 V (\bullet), 1.06 V (\blacksquare)) for an anodized catalyst film deposited onto a Pt RDE by passage of 1.0 mC cm^{-2} and operated in B_i electrolyte, pH 9.2. Sufficient KNO_3 was added to maintain a constant total ionic strength of 2 M in all electrolytes. Koutecký–Levich analysis was used to extract activation-controlled current densities in weakly-buffered electrolyte, where the measured current was dependent on rotation rate. The experimental reaction orders (slopes of the linear fits) in B_i are (from top to bottom) -0.95 , -1.04 and -0.95 .

decay, t :¹³

$$\log j_t = \log j_{t=0} - \log(1 + t/\tau) \quad (3.2)$$

where $\log j_{t=0}$ is the initial current density before open circuit conditions. The resulting Tafel plots (Figure 3.3 inset) illustrate a significant difference in the activity of anodized versus non-anodized films. We note that the Tafel plot of the anodized film is concordant with that obtained by steady state polarization measurements of Figure 3.1.

3.2.3 Determination of reaction order in B_i .

The dependence of reaction rate on buffer strength was interrogated by controlled potential electrolysis of anodized catalyst films at 1.04, 1.05 and 1.06 V in Ni-free electrolyte, pH 9.2 with varying B_i concentrations $[B_i]$ from 630–6.3 mM (Figure 3.4). Sufficient KNO_3 was added to each solution to preserve a constant high ionic strength of 2 M. Diffuse double layer

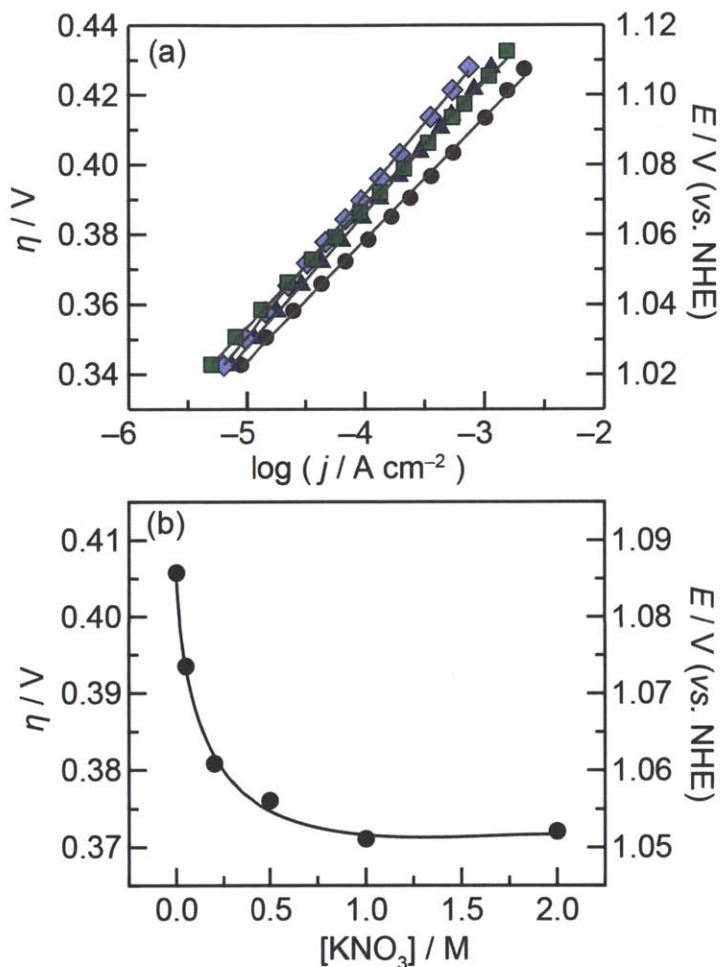


Figure 3.5. (a) Tafel plots, $E = (E_{\text{applied}} - iR)$, $\eta = (E - E^\circ)$, for a 1.0 mC cm^{-2} anodized catalyst film deposited onto FTO and operated in 1.0 (\bullet), 0.5 (\blacksquare), 0.2 (\blacktriangle), and 0.1 (\blacklozenge) M KBi without any added supporting electrolyte. Tafel Slopes are 34, 35, 38, and 41 mV/decade, respectively. (b) Dependence of steady state electrode potential, $E = (E_{\text{applied}} - iR)$ and overpotential, $\eta = (E - E^\circ)$ for a 1.0 mC cm^{-2} catalyst film operated at 0.4 mA cm^{-2} in 0.1 M KBi electrolyte with varying concentrations of KNO_3 as supporting electrolyte.

effects,¹¹ which lead to spuriously elevated Tafel slopes and distorted reaction orders (Figure 3.5a) can be eliminated by operating at constant ionic strength as well as maintaining a low concentration of buffering species relative to an inert supporting electrolyte (Figure 3.5b).¹⁵

Catalyst films were deposited onto a Pt RDE that had been pre-treated to render any current due to Pt oxide formation negligible (see section 3.5). For each electrolyte examined, the RDE was operated until a steady-state current value was attained at various ω . In instances

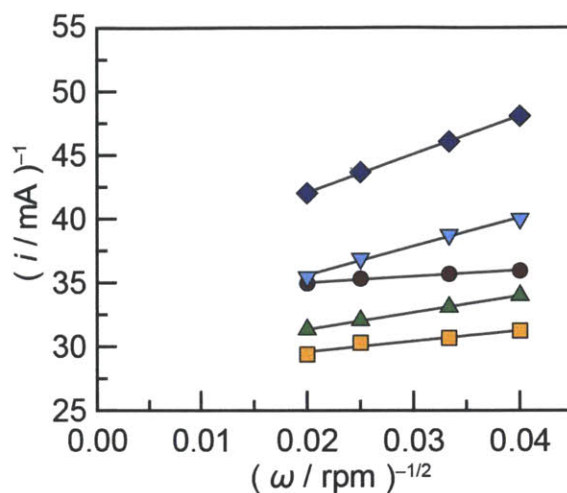


Figure 3.6. Steady state Koutecký–Levich plots of a 1.0 mC cm^{-2} catalyst film prepared onto a Pt RDE and operated at $E = 1.04 \text{ V}$ at 2500, 1600, 900, and 625 rpm in 40 (●), 25 (■), 16 (▲), 10 (▼), and 6.3 (◆) mM KB_i electrolyte, with added KNO_3 to preserve an ionic strength of 2 M.

where the $[\text{B}_i]$ was less than 100 mM, the observed currents were subject to mass transport limitations, as evidenced by the dependence of i on ω . In these cases, Koutecký–Levich (K–L) plots of $i^{-1/2}$ as a function of $\omega^{-1/2}$ were constructed (Figure 3.6) to extract the activation-controlled current values by linear extrapolation to the limit of infinitely high rotation rates (i.e. $\omega^{-1/2} \rightarrow 0$).^{16,17} In all cases, Ohmic potential losses amounted to less than 1 mV and therefore they were neglected. Figure 3.4 shows the logarithm of the activation-controlled current density plotted as a function of $\log[\text{B}_i]$. For $[\text{B}_i] \geq 40 \text{ mM}$, the slope of the plot establishes an inverse first order dependence of current density on B_i activity. In electrolytes of very low buffer strength ($[\text{B}_i] < 40 \text{ mM}$), film activity deviates from this reaction order, and an ostensibly zeroth order regime is observed.

3.2.4 Determination of reaction order in H^+ activity.

Given the explicit reaction order in B_i , any measurements of reaction rate dependence on pH will inevitably alter the activity of boric acid, borate anion, or both. To evaluate the reaction order in H^+ activity, anodized films were deposited onto a Pt RDE and steady-state data were collected as a function of pH. Initially, a galvanostatic titration at $10 \mu\text{A cm}^{-2}$ in an electrolyte

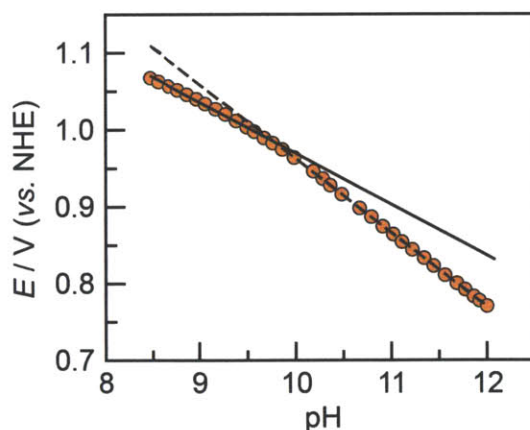


Figure 3.7. pH dependence of steady-state electrode potential at constant current density ($j_{\text{anodic}} = 10 \mu\text{A cm}^{-2}$) for an anodized 1.0 mC cm^{-2} catalyst film on FTO operated in 0.1 M B_i 2 M KNO_3 electrolyte. Slopes equal -64 (—) and -96 (---) mV/pH unit.

with a constant $[\text{B}_i]_{\text{total}} = 100 \text{ mM}$ was undertaken in the presence of 2 M KNO_3 . The titration was commenced at pH 8.5 and the potential required to sustain constant current density was measured as the pH of the solution was raised incrementally. At low current density, no local pH gradients arise, even when the pH is adjusted outside of the ideal B_i buffering regime. Additionally, Ohmic potential losses were less than 0.5 mV and they can be neglected. The plot of potential as a function of pH (Figure 3.7) shows two limiting slopes of -64 mV/pH unit and -96 mV/pH unit for pH ranges 8.5–9.8 and 10–12, respectively. The bifurcation observed at pH 10 indicates that either (1) there is a change in mechanism (such as a change in Tafel slope) at pH 10 or (2) there exists an inverse first order dependence of reaction rate on only borate anion (B_i^-), and not on boric acid, $\text{B}(\text{OH})_3$, such that as the pH is increased from 8.5–10, the corresponding exponential increase in the concentration of B_i^- serves to skew the true dependence on H^+ activity. In this case, the intrinsic proton order is observed for $\text{pH} > 10$ where $[\text{B}_i^-]$ reaches saturation.

A separate experiment was conducted to distinguish between scenarios (1) and (2). Films were deposited onto a Pt RDE, and Tafel data were collected using B_i solutions at pH 8.5, 9.2, 10.2, 11.2 and 12.0 (Figure 3.8a). In each electrolyte, the total buffer concentration $[\text{B}_i]$ was

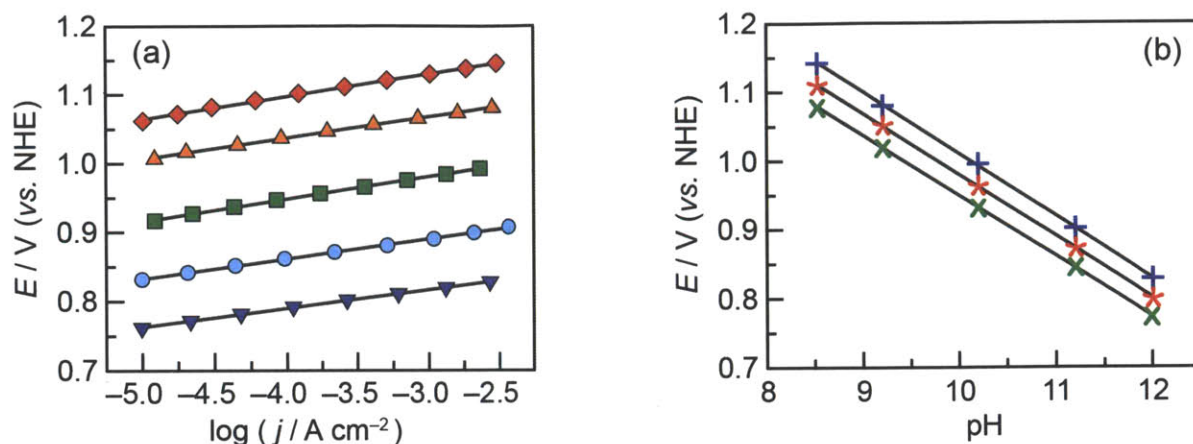


Figure 3.8. (a) Tafel plots, $E = (E_{appl} - iR)$ for anodized NiBi catalyst films deposited on a Pt rotating disk electrode by passing 1.0 mC cm^{-2} , and operated in 0.60 M B_i pH 8.5 (\blacklozenge), 0.20 M B_i pH 9.2 (\blacktriangle), 0.11 M B_i pH 10.2 (\blacksquare), 0.10 M B_i pH 11.2 (\bullet), and 0.10 M B_i pH 12.0 (\blacktriangledown). Each electrolyte contained an additional 0.9 M KNO_3 as supporting electrolyte to maintain an ionic strength of about 1 M . Koutecký–Levich plots were constructed to extract activation-controlled current densities where necessary. (b) Interpolation of Tafel plots at 2.5 mA cm^{-2} ($+$), 0.25 mA cm^{-2} ($*$), and 0.025 mA cm^{-2} (\times). Slopes are -90 , -89 , and -88 mV/pH unit respectively.

varied such that the concentration of borate anion $[\text{B}_i^-]$ was maintained at 100 mM ; 0.9 M KNO_3 was added to each solution to preserve a constant ionic strength of 1 M . Where necessary, the activation-controlled current densities were obtained from K–L analysis. There is no mechanistic change over the pH range explored; all Tafel slopes lie between 28 and 32 mV/decade . This suggests that scenario (2) is at the root of the change observed for $\text{pH} > 10$. Interpolation of each Tafel plot at 2.5 , 0.25 and 0.025 mA cm^{-2} yields the potential dependence on pH (Figure 3.8b). The single observed slope $(\partial E / \partial \text{pH})_j = -90 \text{ mV/pH}$ over the pH range 8.5 – 12.0 is a convolution of the pH dependence of the current density $(\partial \log j / \partial \text{pH})_E$ and the potential dependence of the current density $(\partial E / \partial \log j)_{\text{pH}}$. That is:¹⁸

$$\left(\frac{\partial E}{\partial \text{pH}}\right)_j = -\left(\frac{\partial \log j}{\partial \text{pH}}\right)_E \left(\frac{\partial E}{\partial \log j}\right)_{\text{pH}} \quad (3.3)$$

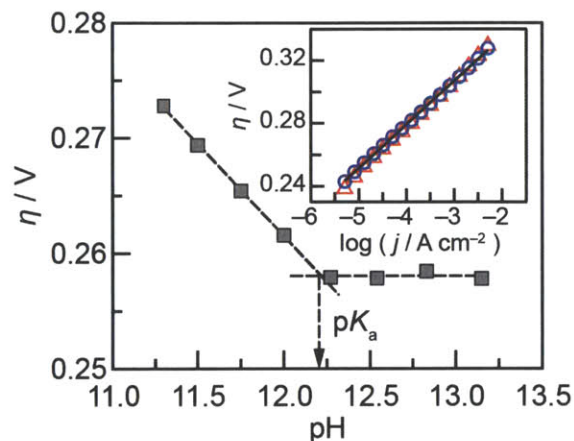


Figure 3.9. Plot of the pH dependence of steady-state electrode overpotential (■), at constant current density ($j_{anodic} = 10 > \mu\text{A cm}^{-2}$) for an anodized 1.0 mC cm^{-2} catalyst film deposited onto FTO and operated in 0.1 M B_i 2 M KNO_3 electrolyte. The change in slope at pH 12.2 is consistent with the elevation of the bulk pH above the pK_a of an active site moiety. The inset shows Tafel plots, $\eta = (E - iR - E^\circ)$, for anodized catalyst films deposited onto a Pt RDE by passage of 1.0 mC cm^{-2} and operated at 2000 rpm in $0.1 \text{ M KOH } 1.9 \text{ M KNO}_3$ pH 12.9 (○) and $1.0 \text{ M KOH } 1.0 \text{ M KNO}_3$ pH 13.8 (Δ) electrolyte. Tafel slopes are 28 and 30 mV/decade, respectively.

Substituting $(\partial E/\partial \text{pH})_j = -90 \text{ mV/pH}$ (from Figure 3.8b) and $(\partial E/\partial \log j)_{\text{pH}} = 30 \text{ mV/decade}$ (the Tafel slope) into eq. 3.3 gives $(\partial \log j/\partial \text{pH})_E = +3$. The reaction order in H^+ activity $(\partial \log j/\partial \log a_{\text{H}^+})_E$ may thus be determined as:

$$\left(\frac{\partial \log j}{\partial \log a_{\text{H}^+}}\right)_E = -\left(\frac{\partial \log j}{\partial \text{pH}}\right)_E \quad (3.4)$$

which yields a reaction order in proton activity a_{H^+} of -3 . We therefore deduce that the reaction rate is zeroth order in boric acid activity, inverse first order in borate anion activity, and inverse third order in proton activity between pH 8.5 and pH 12 for $[\text{B}_i^-]$ in excess of 20 mM.

A galvanostatic titration in 100 mM B_i from pH 11–13 was used to investigate a change in the pH dependence under alkaline conditions, which might be expected to arise when the pH is elevated beyond the pK_a of an active site species. As shown in Figure 3.9, a plateau in the plot of η vs. pH is observed at pH ~ 12.2 . However, since Tafel data acquired in 0.1 and 1.0 M KOH (Figure 3.9 inset) continue to exhibit slopes close to 29 mV/decade, the mechanistic change that

results in this plateau in the η vs. pH plot does not arise from changes in Tafel slope. Instead, this behavior must arise exclusively from changes in the H^+ reaction order.

According to Figure 3.9, for $pH > 12.2$ there is no dependence of the current density on pH at constant overpotential. This parameter, $(\partial \log j / \partial pH)_\eta$, is related to the pH dependence of the current density at constant potential, $(\partial \log j / \partial pH)_E$ through the transfer coefficient, α ($\alpha = 2.3RT/bF$, where b is the Tafel slope):¹⁸

$$\left(\frac{\partial \log j}{\partial pH}\right)_E = \left(\frac{\partial \log j}{\partial pH}\right)_\eta + \alpha \quad (3.5)$$

Both Tafel slopes are close to 29 mV/decade, and therefore $\alpha = 2.3RT/0.029F = 2$. By substituting $(\partial \log j / \partial pH)_\eta = 0$ and $\alpha = 2$ into eq. 3.5 we find $(\partial \log j / \partial pH)_E = 2$, indicating a reaction order in H^+ activity of -2 (eq. 3.4). Therefore the reaction order in H^+ activity transitions from a value of -3 over the range pH 8.5 to 12 (Figures 3.8a and 3.8b) to -2 at $pH \geq 12.2$ (Figure 3.9). These results indicate that one of the three kinetically relevant protic centers of Ni-B_i active sites possesses a pK_a of 12.2. In strongly alkaline electrolytes, this species is deprotonated in the resting state of the catalyst and ceases to contribute to the electrochemical rate law.

3.2.5 Tafel data in B_i-free electrolyte.

To explore OER kinetics in the absence of a weak base, steady state polarization data were collected in 1 M NaClO₄ pH 8.5 solution. Films were deposited onto a Pt RDE by passage of 1.0 mC cm⁻² and anodized in B_i buffered solutions. Tafel data were obtained in NaClO₄ electrolyte by extrapolation of K-L plots at each potential considered in order to eliminate mass transport limitations through the bulk electrolyte. Over the course of the experiment, small aliquots (1–5 μ L) of 1 M NaOH were added periodically to preserve the bulk pH at 8.50(1). Tafel data are the average of three runs.

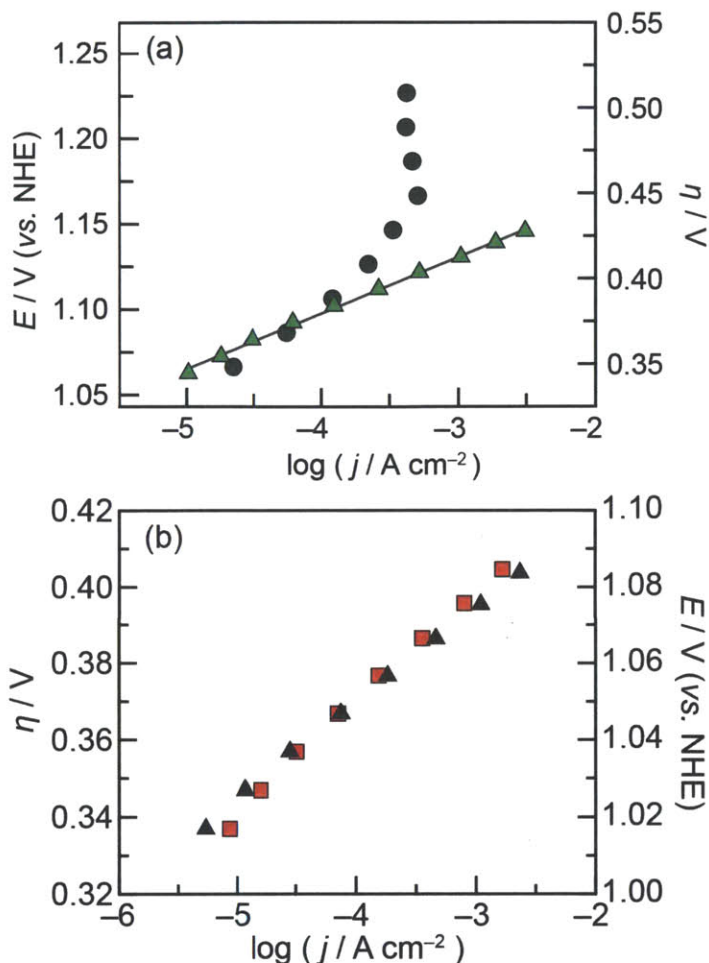


Figure 3.10. (a) Tafel plots, $E = (E_{\text{appl}} - iR)$, $\eta = (E - E^\circ)$, for anodized catalyst films deposited onto a Pt RDE by passage of 1.0 mC cm^{-2} and operated in 1 M NaClO_4 pH 8.5 electrolyte (●). Koutecký–Levich analysis of steady state current densities at various rotation rates was used to eliminate mass transport limitations through solution. The data shown is the average of three consecutive runs. A Tafel plot of an identical catalyst film in 0.6 M KB_i 0.9 M KNO_3 pH 8.5 (0.1 M B_i^- , total ionic strength = 1 M) electrolyte (▲), displaying a 32 mV/decade Tafel slope (—), is shown for comparison. (b) Activity profile of a 1.0 mC cm^{-2} catalyst film deposited onto a Pt RDE and operated in 0.5 M KB_i 1.75 M KNO_3 pH 9.2 electrolyte after operation in 1.0 M NaClO_4 , pH 8.5 electrolyte (▲), compared to the activity profile of a freshly prepared catalyst film (■).

The resulting Tafel plot displays a greatly elevated slope compared to Tafel data acquired in B_i electrolyte, pH 8.5 (Figure 3.10a). The kinetic profile of catalyst films in B_i buffered media following operation in B_i -free electrolyte was comparable to the activity of a freshly prepared

film (Figure 3.10b), indicating that the Tafel behavior obtained in the absence of B_i cannot be attributed to the corrosion of catalyst films in buffer-free electrolyte.

3.3 DISCUSSION

3.3.1 Steady-state Tafel data.

Tafel behavior describing the effect of potential, E , or overpotential, η , on steady-state current density, along with experimentally determined reaction orders form the basis of the mechanistic analysis of oxygen evolution by Ni- B_i catalyst films. Steady-state current densities are proportional to the activation-controlled velocity of the OER if the reaction is not subject to mass-transport limitations. This requirement is true of the electrokinetic studies described herein, since in well-buffered electrolytes Tafel data collected using a RDE is identical irrespective of rotation rate or whether stirring was the sole means of mass transport with the electrode stationary (Figure 3.2a), resulting in Tafel slopes, b , (where $b = \partial E / \partial \log j$)_{pH} of 28 mV/decade in each case. In cases where mass transport limitations were encountered (poorly-buffered media, or electrolytes completely lacking a weak base electrolyte), Koutecký-Levich analysis was employed to extract activation-controlled current densities. Furthermore, the Tafel plots are the same for sequential runs and independent of the direction of potential change during data acquisition (Figure 3.2b), verifying that catalyst films are not altered appreciably over the course of experiments. Precise control of catalyst film thickness was accomplished by managing the total charge passed during deposition. Although the resultant film thicknesses ranged from 1 to 5 nm (equivalent to 3–15 monolayer's of catalyst), Tafel plots collected for each film gave similar slopes, close to 30 mV/decade (Figure 3.1). Since activated transport through the film can impose additional potential barriers to electronic/ionic conductivity,^{19–21} consistent slopes over a range of film thicknesses (particularly at almost monolayer coverage) demonstrates the absence of non-Ohmic potential losses between the potential applied at the electrode and that experienced by active sites. For anodized catalyst films, Tafel plots (Figure 3.1) yield 30

mV/decade slopes that are consistent with a mechanism involving a chemical turnover-limiting step (TLS) that follows a two-electron pre-equilibrium. The reciprocal of the Tafel slope in dimensionless form is known as the transfer coefficient, $\alpha = 2.3RT/bF = 2$ for $b = 29.5$ mV/decade at 25 °C.¹⁸ Although the Tafel slopes are independent of film thickness, the apparent exchange current densities and hence the overall activity of films does increase with loading. This would be expected to occur, as anodes with thicker catalyst layers should possess more active sites per unit geometric area in these porous films. Lower-limit TOFs of 0.9 mol O₂ (mol Ni)⁻¹ s⁻¹ are observed at $\eta = 400$ V in pH 9.2 electrolyte and 1.7 mol O₂ (mol Ni)⁻¹ s⁻¹ at $\eta = 325$ mV in 1 M KOH. Lower-limit TOF for these catalysts may be calculated at any η by recognizing that the TOF decreases by an order of magnitude per 30 mV increment. Thus, these catalyst films rival the most active OER anodes reported to date.²²

3.3.2 OER of non-anodized Ni-B_i.

Monitoring the decay in open circuit potential after interrupting an applied potential bias offers a complementary means of determining the Tafel slope of an electrokinetic reaction.^{3,13,14} This method is the most appropriate means of extracting electrokinetic information on the OER at the less catalytically active non-anodized films, since polarization of the electrode for an extended period of time leads to anodization.¹ The higher activity of anodized films is immediately evident in the very rapid decay at early times due to more efficient O₂ evolution as compared to the less catalytically active non-anodized films (Figure 3.3). Indeed, since the Tafel slope for anodized films is found to be 33 mV/decade (in agreement with Figure 3.1), the corresponding OCP-decay transient indicates that the surface concentration of catalytic intermediates in anodized NiB_i decreases by over three orders of magnitude in the first 100 ms after the potential is removed. In contrast, the Tafel slope of non-anodized films is considerably higher, approaching 100 mV/decade. Tafel slopes of 120 (± 20) mV/decade are expected for mechanisms involving a turnover-limiting electron transfer (ET) from the resting state:¹⁸



The turnover velocity for such a reaction will be given by:

$$v = k_{ET}\theta_A \quad (3.7)$$

where k_{ET} is the rate constant for the turnover limiting electron transfer, and θ_A is the surface coverage of the resting state species, A.²³

$$\frac{\Gamma_A}{\Gamma_{\max}} \quad (3.8)$$

Γ_A is the surface concentration of active sites that exist in state A (expressed in mol/cm²), and Γ_{\max} is the total surface concentration of active sites. It is important to note that Γ_{\max} need not equal the surface concentration of solvent-exposed metal centers, or even the concentration of electroactive Ni centers, since the number of active sites may actually represent a very small proportion of these centers. Under Langmuir conditions, since A is the resting state, θ_A may be assumed to be a constant equal to 1.²³ The rate constant k_{ET} is given by:

$$k_{ET} = k_{ET}^0 \exp\left(\frac{\beta\eta F}{RT}\right) \quad (3.9)$$

The parameter k_{ET}^0 is the ET rate constant at $\eta = 0$, and β is the symmetry factor for the microscopic (irreversible) ET step, which determines the amount of the total driving force due to η (i.e. $\Delta G = -\eta F$), that causes a decrease in the activation energy barrier (i.e. $\Delta(\Delta G^\ddagger) = -\beta\eta F$).¹² Thus the electrochemical rate law for a reaction that proceeds by eq. 3.6 will be:

$$j = 4Fk_{ET}^0 \exp\left(\frac{\beta\eta F}{RT}\right) \quad (3.10)$$

This will lead to a Tafel slope ($\partial\eta/\partial\log j$) of $2.3 \times RT/\beta F$. β is usually close to 0.5 (± 0.1),¹² resulting in a Tafel slope of around 120 mV/decade at 298 K. Importantly, in this case, the

symmetry factor, β , and the transfer coefficient for the overall OER, α , are numerically identical, since the kinetics of the overall multi-electron reaction are governed entirely by the microscopic rate-limiting ET step.¹² In cases where one or more electron transfers exist in equilibrium, β and α are distinct.

It is unclear whether the suppression of the Tafel slope of non-anodized films from 120 mV/decade to 100 mV/decade arises due to the existence of a marginally altered β -value of 0.6, or is a result of the unavoidable partial anodization of the film during deposition.¹ However, the existence of a turnover-limiting electron transfer in non-anodized films is reasonable. The resting state nickel valency in non-anodized films is predominantly +3, and the local coordination environment of Ni centers in such films exhibits the Jahn-Teller (J-T) distortion that is expected for low-spin d^7 ions.¹ Thus the first oxidation process during turnover should be kinetically sluggish, as it would incur a large reorganizational energy penalty associated with a low-spin $d^7 \rightarrow d^6$ transformation. We conclude therefore that this high reorganizational energy associated with Ni^{3+} oxidation contributes to very low catalytic activity of non-anodized $Ni-B_i$ films.

3.3.3 OER of anodized $Ni-B_i$.

XAS shows that anodization of $Ni-B_i$ films leads to a gradual phase change (involving changes in both local structure and resting state nickel valency) that eliminates the J-T distortion present in non-anodized films.¹ In the absence of structural distortion in local geometry, the oxidation of Ni centers in anodized films should be more facile. Indeed, the 30 mV/decade Tafel slope obtained by steady state Tafel plots (Figures 3.1 and 3.2) and open-circuit decay transients (Figure 3.3) indicates that the turnover-limiting step is a chemical in nature and does not involve ET.

Before evaluating the dependence of activity on pH and therefore the existence of proton-transfer (PT) equilibria prior to the TLS, it was necessary to establish the dependence of reaction rate on buffer strength, since any $[B_i]$ dependence would have to be accommodated

during pH changes. The resulting inverse first order dependence of current density on $[B_i]$ over almost 1.5 decades (Figure 3.4) is consistent with the reversible dissociation of a B_i species from an active site over this range in buffer strength. Boric acid and borate species are known to adsorb to oxide surfaces in aqueous media by coordination to the metal centers.²⁴⁻²⁷ The -1.0 reaction order in borate (Figure 3.4) establishes that the ligation of the buffer species is governed by the Langmuir isotherm with a high surface coverage of the adsorbate.²³ Accordingly, the B_i -free active sites necessarily exist in minor equilibrium with a B_i -bound resting state. We note that our data cannot distinguish adsorption of poly-borate species²⁸⁻³⁰ as opposed to $B(OH)_4^-$. Decreasing the concentration of B_i in the electrolyte gives rise to an increase in activation-controlled current density until a point where there appears to be no dependence of reaction velocity on B_i (< 40 mM B_i).

While demonstrating an association between buffering species and active sites, B_i dependence studies alone could not distinguish which B_i species (boric acid, borate anion (B_i^-), or both) must dissociate from active sites during turnover for oxygen to be evolved. The pH dependence of the steady-state electrode potential at a constant high ionic strength changes from about -60 mV/pH over the B_i buffering range to about -90 mV/pH at B_i^- saturation (Figure 3.7). In contrast, Tafel data collected between pH 8.5 and pH 12 at a constant concentration of borate anion exhibit Tafel slopes of approximately 30 mV/decade (Figure 3.8a). The pH dependence of the steady-state electrode potential was determined to be about -90 mV/pH by interpolating the Tafel plots at constant current density (Figure 3.8b). These results identify that the observed desorption step involves the liberation of one borate anion into bulk electrolyte per active site, and confirms a three-proton equilibrium prior to the TLS. Were both species to be liberated from active sites, the activity of boric acid *and* borate in solution should appreciably modulate OER kinetics on NiB_i films, and an experiment in which the total B_i (boric acid + borate) concentration is held constant as the pH is varied (Figure 3.7) should yield a single slope and the genuine reaction order in H^+ activity. However, if the desorption equilibrium applies to only one species of the conjugate pair, the pH dependence of reaction rate will inevitably be convoluted

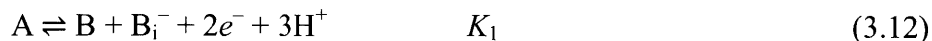
with the reaction order in that species unless the total B_i concentration is adjusted to maintain a constant activity in the coordinated species alone (Figures 3.8a and 3.8b), or the pH regime is such that B_i speciation does not change appreciably with pH (pH > 10 in Figure 3.7).

Electrokinetic data should be acquired in an excess of supporting electrolyte. If not, the potential dependence of anion migration and the effects on local pH and specific adsorption of borate will skew Tafel data and lead to slopes that are dependent on B_i concentration, and apparent fractional reaction orders (Figure 3.5a). These effects are eliminated by maintaining a constant, high ionic strength ($I \geq 1$ M) using an inert supporting electrolyte such as KNO_3 , which when present at an appreciable concentration, serves to reduce the transference number of borate anion (the fraction of the total ionic current that is carried by borate anions) (Figure 3.5b).

Taken together, the results of Figures 3.1–3.8 reveal the electrochemical rate law for oxygen evolution in moderate to high borate ion concentrations (20–300 mM) at anodized Ni– B_i films to be:

$$j = k_0 (a_{B_i^-})^{-1} (a_{H^+})^{-3} \exp\left(\frac{2EF}{RT}\right) \quad (3.11)$$

where k_0 is proportional to the exchange current density and independent of potential. This rate expression contains the inverse first order dependence on borate activity as shown in Figure 3.4, the inverse third order dependence on proton activity (Figures 3.7 and 3.8), as well as the factor of 2 (transfer coefficient) in the exponential term in the applied potential, E . At constant borate activity, pH and $T = 25$ °C, the partial derivative of E with respect to $\log j$, $(\partial E / \partial \log j)$ yields a Tafel slope of 30 mV/decade, consistent with Figure 3.1. The experimental rate law in eq. 3.11 is consistent with the mechanistic sequence,:



which involves reversible borate dissociation from the resting state, and a two–electron, three–proton equilibrium followed by a chemical TLS. K_1 is the equilibrium constant at $E_{appl} = 0$, and k_2 is the rate constant for the chemical TLS. Eq. 3.11 may indeed proceed in a number of discrete steps, however these would all exist as quasi-equilibria and such a sequence is kinetically indistinguishable from a single step. In addition, there may be any number of distinct chemical equilibrium steps prior to the TLS, but these cannot be resolved kinetically.

According to eq. 3.13, the steady state velocity of oxygen evolution can be expressed as,

$$v = k_2 \theta_B \quad (3.14)$$

θ_B represents the partial surface coverage of intermediate B. θ_B can be defined in terms of the surface coverage of the resting state A (θ_A) as follows:

$$\theta_B = K_1 \theta_A (a_{Bi^-})^{-1} (a_{H^+})^{-3} \exp\left(\frac{2EF}{RT}\right) \quad (3.15)$$

which involves the application of the Nernst equation to eq. 3.12. Substituting for θ_B in eq. 3.14 gives:

$$v = k_2 K_1 \theta_A (a_{Bi^-})^{-1} (a_{H^+})^{-3} \exp\left(\frac{2EF}{RT}\right) \quad (3.16)$$

If Langmuir conditions are assumed, the surface coverage of the resting state is high, θ_A would not be expected to change appreciably over the potential range, and may be considered a potential-independent constant equal to 1. In this case, eq. 3.16 approximates the experimental rate law (eq. 3.11) with

$$k_0 = 4Fk_2K_1\theta_A \quad (3.17)$$

In situ XAS studies of anodized Ni–B_i films¹ show that there is no systematic shift in the nickel K–edge position with E_{appl} over the potential range used for Tafel data acquisition. This result is

consistent with the assumption that the speciation of the resting state, A, is invariant over the potential range explored and therefore permits θ_A to be taken as a constant (eq. 3.17 above). XANES spectra and coulometric studies also established that the average oxidation state of Ni in anodized catalyst films was +3.6 to +3.8, thereby indicating a substantial amount of formal Ni^{IV} valency in the catalyst resting state.^{1,31} In fact, there appears to be even more formal +4 valency in Ni–B_i compared to Co–OEC. Computational studies of Ni^{IV}–containing extended solid nickelates have demonstrated significant covalency in Ni–O bonding, and extensive delocalization of hole-density onto oxygen centers upon oxidation of the parent Ni^{III} compounds.^{34–36} In addition, EPR studies of a tetracobalt cubane model compound possessing one formally Co^{IV} center as a molecular model of our cobalt-based catalyst revealed a radical distributed almost equally over all Co and O ions, effectively leading to a formal oxidation number of [Co₄^{+3.125}O₄].³⁷ Thus, it is reasonable to expect that this Ni^{IV} valency in the catalyst resting state is distributed extensively over multiple Ni and O centers in the nickel–oxido clusters that form the ordered domains.

Figure 3.9 is effectively a Pourbaix diagram of the catalyst active sites, indicating that one of the protic species possesses a pK_a of about 12.2. At the pH regimes considered in this study, a Ni^{III/IV}–OH₂ resting state is unlikely, given the Pourbaix diagram for nickel.³⁸ In addition, the point of zero charge (pH_z) for nickel oxides, which defines the average of the pK_a values of surface-bound water (M–OH₂) and surface-bound hydroxyl (M–OH) groups³⁹ have been found to be about 8 and 9.75 for Ni(OH)₂ and NiO respectively.^{40–42} Thus we can anticipate the pK_a of a Ni^{III/IV}–OH₂ intermediate would be less than 8. The moiety possessing a pK_a of 12.2 can therefore be more reasonably rationalized as a terminal or bridging Ni–OH. Under highly alkaline conditions (specifically pH > 12.2), this species is deprotonated in the resting state resulting in an overall two–electron, two–proton PCET transformation prior to a chemical turnover-limiting step. This gives rise to a 30 mV/decade Tafel slope and –60 mV/pH unit shift of E (Figure 3.9). Previous EPR studies³⁷ have pointed to the importance of proton loss in PCET steps for generating localized reactive intermediates. In the Co–OECs and Ni–OECs, the ensuing

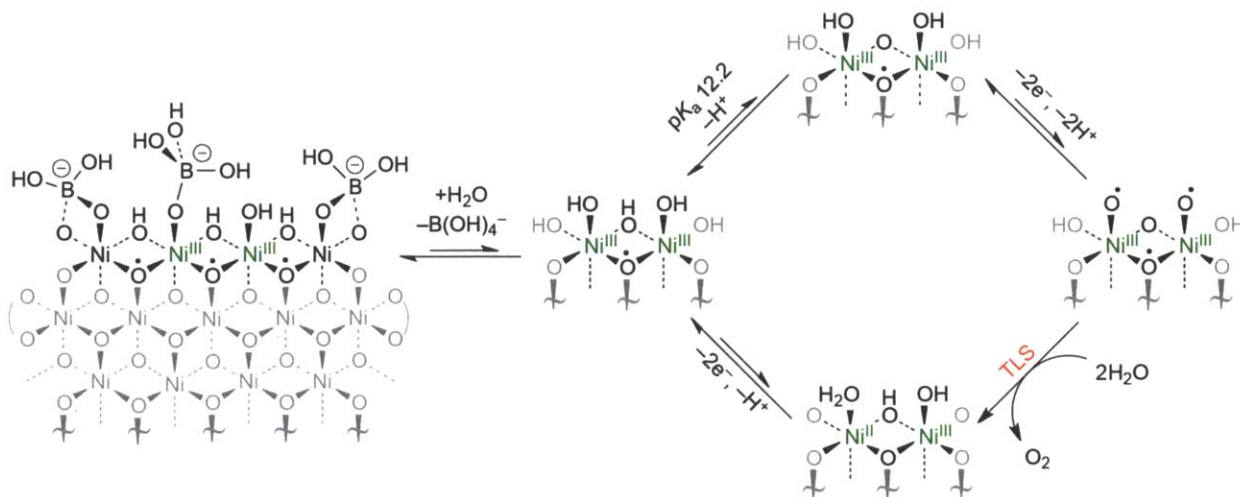


Figure 3.11. Proposed pathway for O_2 evolution by NiBi in Bi ($[\text{B}(\text{OH})_4^-] > 20 \text{ mM}$) electrolyte, pH 8.5–14. The reversible dissociation of borate anion and an overall two-electron, three-proton equilibrium followed by a rate limiting chemical step, is consistent with the experimental electrochemical rate law. A $\mu\text{-OH}$ site possessing a $\text{p}K_{\text{a}}$ of 12.2 is fully deprotonated in the resting state under highly alkaline conditions. Oxidation state assignments are approximate; oxidizing equivalents are likely extracted from orbitals with predominantly O 2p character, particularly for the pre-TLS intermediate.

change in ligand field strength upon deprotonation could localize the unpaired spin density on specific centers leading to their subsequent reactivity towards O–O bond formation. This concept is validated by computational studies of cobalt oxido clusters as Co–OEC models.⁴³ Hence while the resting state valency would be delocalized over the entire cluster, the catalytic intermediates are likely to possess spin density that is more localized due to proton loss.

A mechanistic scheme for oxygen evolution in Bi -buffered electrolyte that is consistent with the interfacial properties of the oxidic surface as well as the electrokinetic data presented herein is shown in Figure 3.11. For convenience, eq. 3.12 has been described as a sequence of several steps in equilibrium. We assign the two-electron minor equilibrium step to the double oxidation of a dinickel active site, which proceeds with the overall deprotonation of a bridging and two terminal hydroxyl groups. These PCET processes are proposed to lead to a highly oxidized intermediate that may be tentatively described as $[\text{Ni}_2^{\text{IV/V}}]$ or $[\text{Ni}_2^{+4.6}]$. Since this

intermediate exists in minor equilibrium at a very low surface coverage, its formal potential must lie well above the potential supplied at the electrode. Nevertheless, this formal $[\text{Ni}_2^{\text{IV/V}}]$ designation is likely not an accurate description of the true electronic structure of the intermediate; we expect that the electron-transfer pre-equilibria arise from orbitals with predominant O 2p contributions, resulting in oxyl radical character. The loss of three protons must contribute significantly to the accessibility of such highly oxidized intermediates by virtue of the PCET redox-potential leveling effect.⁴⁴⁻⁴⁶ One hydroxyl group was found to possess a $\text{p}K_{\text{a}}$ of 12.2, and hence its corresponding deprotonation step must occur prior to the remaining two-electron, two-proton PCET transformations. Since the turnover-limiting step is chemical in nature and unlikely to involve proton transfer to the electrolyte, we find it reasonable to propose that this step involves O–O bond formation and/or Ni–O bond scission. Computational studies on our Co-based system suggests that direct coupling of two terminal $\text{Co}^{\text{IV}}(\text{O})$ groups to form an O–O bond is thermodynamically favorable and proceeds with a low kinetic barrier,⁴³ signifying that it may in fact be the breaking of the metal–oxygen bond that is the turnover-limiting step in these late transition metal oxide catalysts. Spectroscopic studies as well as extensive synthetic and computational modeling will be employed to shed light on the electronic structure of catalytic intermediates and the details of the turnover-limiting process. Further electrochemical studies, particularly on molecular models are also needed to shed light on the details of the coupled multi-proton, multi-electron sequences.

3.3.4 OER in B_i -free electrolyte.

Certainly, one important role of B_i is to preserve the local and bulk pH during O_2 evolution. However, the inverse first order dependence of reaction velocity on borate anion activity in eq. 3.15 implicates a deleterious role of borate on OER kinetics. Despite this ostensibly “inhibitory” effect, the crucial importance of borate to the kinetics of water oxidation on Ni– B_i films is evident in Tafel plots acquired in B_i -free electrolyte (Figure 3.10a). In the absence of B_i , very high Tafel slopes are observed and high current densities cannot be achieved.

Since Koutecký–Levich analysis was used to eliminate effects associated with solution mass transport, and the bulk pH was preserved by constant addition of aqueous NaOH, the elevated Tafel slope in B_i -free electrolyte cannot be attributed to pH gradients at the film–solution interface. In addition, following operation in B_i -free electrolyte, films display no loss in activity in B_i electrolyte (Figure 3.10b), excluding the possibility of catalyst corrosion over the period of polarization in B_i -free electrolyte. The observed Tafel behavior may result from the transition to a turnover-limiting chemical step from the resting state; the absence of any preceding electrochemical steps results in a potential-independent kinetic profile, and therefore an extremely high (“infinite”) Tafel slope. We observed a similar result for phosphate-free electrolytes of Co-based catalyst films. These preliminary electrokinetic data suggest that proton transfer processes may become turnover-limiting in the absence of a good proton acceptor, at low hydroxide ion concentrations. Additional studies are ongoing to shed more light on the details of OER under such conditions, but these results underscore the critical importance of borate to facilitating proton transfers, thereby expediting the PCET sequences necessary for rapid O_2 evolution.

3.3.5 Differences in mechanism and activity of Co–OECs and Ni–OECs.

Differences in activity between oxido Co–OECs and Ni–OECs are governed to a large extent by the characteristics of the PCET pre-equilibrium. A two-electron oxidation is required before the chemical turnover-limiting step in anodized Ni– B_i OEC films (30 mV/decade Tafel slope), whereas turnover at Co–OEC films involves a one-electron pre-equilibrium (60 mV/decade Tafel slope).

We propose that this difference arises because O–O bond formation in both systems proceeds by radical coupling of two active site oxygen centers.⁴³ In Co–OEC, this oxygen-centered unpaired spin density arises upon generation of somewhat localized, low-spin formally d^5 Co^{4+} centers^{32,37,43} Realization of a similar electronic structure would require more substantial oxidation for a nickel catalyst than for a cobalt-based system. As such, it would be expected to

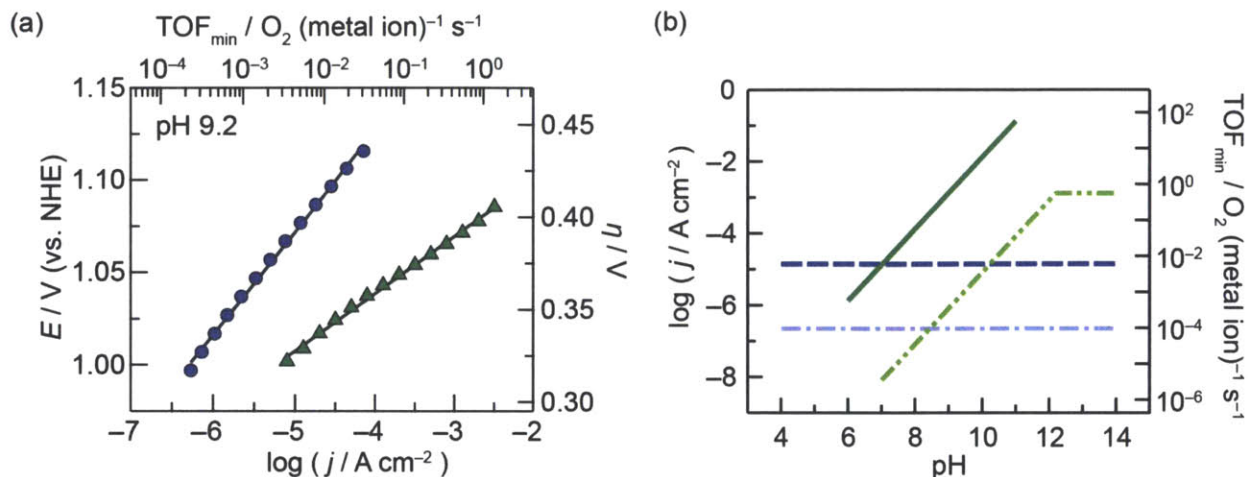


Figure 3.12. Comparison of ultrathin Co-B_i and Ni-B_i OEC films with identical catalyst loadings of 6 nmol metal ions/cm². (a) Tafel plots of Co-B_i (●) and Ni-B_i (▲) in 0.5 M KBi 1.75 M KNO₃ pH 9.2 electrolyte. Tafel slopes equal 55 and 31 mV/decade, respectively (b) Schematic of the pH dependence of the current density and lower-limit turnover frequency of Co-B_i at a constant overpotential of 400 mV (blue —) and 300 mV (light blue — · —) compared to that of Ni-B_i at 400 mV (light green —) and 300 mV (green — · —) overpotential. Curves were calculated using the appropriate experimentally-determined electrochemical rate laws. Ni-based films display a much higher *apparent* specific activity (since the true number of active sites cannot be known) than Co-based films above pH 8. However, due to their disparate electrochemical rate laws, a crossover is expected to occur around neutral pH, at which point Co-based films would yield higher activity anodes. The precise pH at which crossover occurs depends on the overpotential applied due to the different Tafel slopes.

lead to a lower exchange current density, but also a lower Tafel slope, provided the ET steps remain kinetically facile. This is indeed what is observed when one compares Co-B_i with Ni-B_i at comparable catalyst loadings at pH 9.2 (Figure 3.12a). Additionally, the more extensive oxidation would also demand greater accompanying H⁺ loss, leading to disparate pH dependences.

Because of the differences in pH dependence for the two catalysts, Ni-B_i increasingly outperforms Co-OEC as elevated pH (Figure 3.12b). However, at neutral pH and slightly acidic conditions, Co-OEC surpasses Ni-B_i in activity. The majority of studies on the OER have been conducted in highly alkaline media,^{48–50} and these have led to useful trends in correlating specific thermodynamic parameters (such as M–O bond strengths, enthalpies of formation of the

metal(III) hydroxide compound, and adsorption enthalpies of proposed intermediates) with catalytic activity, resulting in the general consensus that for first row transition metal oxides, OER activity increases in the order: $\text{MnO}_x < \text{FeO}_x < \text{CoO}_x < \text{NiO}_x$.^{5,51-54} However, as evident from Figure 3.12b, activity trends in concentrated base may not hold in intermediate pH electrolytes because of disparate PCET pre-equilibria involved in the mechanism of the OER at different catalysts.

3.4 Conclusion

Electrodeposited ultrathin anodized Ni-B_i catalyst films exhibit a Tafel slope of 30 mV/decade in well-buffered electrolytes between pH 8.5 and 14. Electrokinetic studies demonstrate that oxygen evolution in B_i-buffered electrolyte entails the reversible dissociation of borate anion from the resting state and a two-electron, three-proton equilibrium followed by a chemical turnover-limiting step. Under highly alkaline conditions, a change in reaction order in proton activity is observed that is attributed to the full deprotonation of a protic center with a pK_a of 12.2. On the basis of previous in situ XAS, a mixed valence Ni^{III/IV} resting state is invoked, although radical character on oxygen ions in this resting state as well as the subsequent catalytic intermediate states is anticipated. These studies highlight the contradicting roles of borate as both an inhibiting adsorbate and a proton acceptor for PCET at intermediate pH. The much lower catalytic activity of non-anodized films appears to arise, in part, from the large reorganizational energy involved in electron transfer from the Jahn–Teller distorted Ni^{III} resting state found in non-anodized films, which makes this electron transfer rate-limiting. The low Tafel slope of anodized Ni-B_i films makes this catalyst ideal for integration with buried-junction semiconductors.

3.5 Experimental Methods

Materials. Ni(NO₃)₂•6H₂O 99.9985% was used as received from Strem. KOH 88%, KNO₃ 99.0–100.5% and H₃BO₃ 99.9% were reagent grade and used as received from Macron.

NaClO₄ hydrate (99.99% metals basis) was used as received from Aldrich. All electrolyte solutions were prepared with type I water (EMD Millipore, 18 MΩ cm resistivity). Fluorine–tin–oxide (FTO) coated glass (TEC-7) was purchased as pre-cut 1 cm × 2.5 cm glass pieces from Hartford Glass. Unless stated otherwise, all experiments used FTO with 7 Ω/sq surface resistivity.

General Electrochemical Methods. Potentiometric and voltammetric measurements were undertaken with a CH Instruments 760C or 760D bipotentiostat, a BASi Ag/AgCl reference electrode, and a Pt-mesh counter electrode. Rotating disk electrode (RDE) measurements were conducted using a Pine Instruments MSR rotator and a 5 mm diameter Pt-disk rotating electrode. All electrochemical experiments were performed at 23 ± 1 °C using a three-electrode compartment cell with a porous glass frit separating the working and auxiliary compartments. Electrode potentials were converted to the NHE scale using $E(\text{NHE}) = E(\text{Ag}/\text{AgCl}) + 0.197 \text{ V}$. Overpotentials were computed using $\eta = E(\text{NHE}) - 0.68 \text{ V}$ at pH 9.2. Unless stated otherwise, the electrolyte comprised 0.5 M potassium borate (KB_i), 1.75 M potassium nitrate, pH 9.2 (henceforth referred to as KB_i/KNO₃ electrolyte).

Film Preparation. Catalyst films were prepared via controlled-potential electrolysis of 0.1 M KB_i, pH 9.2 electrolyte solutions containing 0.4 mM Ni²⁺. To minimize precipitation of Ni(OH)₂ from these solutions, 25 mL of 0.2 M KB_i was added to 25 mL of 0.8 mM Ni²⁺ solution. The deposition solutions were subsequently filtered through a 0.2 μm syringe filter (Pall) to remove any Ni(OH)₂ that formed. The solutions thus prepared remained clear over the course of deposition, which was carried out onto an FTO-coated glass piece. These FTO working electrodes were rinsed with acetone and water prior to use. A ~0.6 cm wide strip of Scotch tape was applied to the FTO coated side such that a 1 cm² area was exposed to solution. Unless stated otherwise, deposition by controlled potential electrolysis was carried out on quiescent solutions at 1.15 V without *i*R compensation and with passage of 1 mC cm⁻². A typical deposition lasted 70 s. Following deposition, films were rinsed by dipping briefly in 0.1 M KB_i, pH 9.2 solution to remove any adventitious Ni²⁺. Anodized films were subsequently electrochemically treated in 1

M KB_i, pH 9.2 electrolyte by passing an anodic current of 3.5 mA cm⁻² with stirring. A steady potential was obtained after about 30 min of anodization. Unless stated otherwise, films were anodized for 1 h.

Potentiostatic Tafel Data Collection. Current–potential data were obtained by conducting controlled potential electrolysis in KB_i/KNO₃ electrolyte pH 9.2 at a variety of applied potentials (E_{app}). Prior to film deposition and anodization, the solution resistance of the electrolyte to be used for Tafel data collection was measured using the iR test function. The electrolysis solution was exchanged for Ni²⁺–containing KB_i electrolyte, without disturbing the relative positions of the working and reference electrodes and films were deposited. Following film preparation, the working electrode was rinsed in fresh Ni–free KB_i electrolyte and transferred, without drying, to the same electrolysis bath in which the solution resistance was measured. The electrode was allowed to equilibrate with the electrolyte solution for 5 min while being held at the open circuit potential. The solution was stirred and steady–state currents were then measured at applied potentials that descended from 1.13 V to 1.00 V in 7–20 mV steps. For currents greater than 10 $\mu\text{A cm}^{-2}$, a steady state was reached at a particular potential in less than 400 s. For currents lower than 10 $\mu\text{A cm}^{-2}$, longer electrolysis times (15–20 min) were utilized to ensure that steady state had been achieved. The solution resistance measured prior to the data collection was used to correct the Tafel plot for Ohmic potential losses.

Cyclic Voltammetry. CVs of anodized catalyst films were recorded in KB_i/KNO₃, pH 9.2 electrolyte. After 2 min at open circuit, catalyst films were held at 1.0 V for 60 s, immediately after which CV scans were initiated from 1.0 V. The potential was decreased at a scan rate of 100 mV s⁻¹ with stirring, and with correction for Ohmic potential losses (measured prior to film deposition). At a switching potential of 0.2 V, the direction of scan was reversed, and CVs were terminated at 1.1 V.

Dependence of Tafel data on film thickness and calculation of lower-limit TOF. Steady–state polarization data were acquired following anodization of films deposited by passage of 1.0, 0.4 and 0.083 mC cm⁻². Deposition durations were about 67, 25 and 11 s,

respectively. We note that the charge passed cannot be used as a simple measure of the Ni loading because: (1) non-Faradaic double-layer charging currents for short deposition times (and particularly for the thinnest of these films) accounts for a non-trivial proportion of the total charge passed; and (2) oxygen evolution accompanies deposition, and so a fraction of the charge passed is consumed for OER and not solely for film deposition. Thus, in order to evaluate film loadings, CVs of each film were acquired as described in subheading E and the charge consumed upon film reduction was determined by integration of the cathodic surface wave. Charges of 0.91, 0.53 and 0.21 mC cm⁻² were obtained from analysis of the CVs. We have established that the charge passed upon film oxidation or reduction involves the net transfer of 1.6 electrons per nickel center for films of comparable thickness.¹ Thus, the charges correspond to loadings of about 5.9, 3.4 and 1.4 nmol/cm² of Ni centers, corresponding to films of approximate thicknesses of 5, 3 and 1.0 nm.

Knowing the amount of nickel on each electrode, and by interpolating Tafel data for each film at $\eta = 400$ mV, respective currents at this overpotential can be converted into turnover frequency per nickel center, given that each turnover requires the removal of four electrons. Since the number of active sites is expected to be only a fraction of the number of nickel centers, this calculation returns a lower-limit for the TOF of each active site. The calculated lower-limit on the TOFs at $\eta = 400$ mV in 0.5 M KB_i 1.75 M KNO₃, pH 9.2 are 0.92, 0.51 and 0.49 mol O₂ (mol Ni)⁻¹ s⁻¹ for films deposited by passage of 1.0, 0.4 and 0.08 mC cm⁻² respectively. Similarly, in the case of a 1.0 mC cm⁻² catalyst film operated in 1 M KOH 1 M KNO₃ pH 13.85 electrolyte, we calculate a lower-limit on the TOF of 1.7 mol O₂ (mol Ni)⁻¹ s⁻¹ at $\eta = 325$ mV.

Mass transport dependence studies. To verify that Tafel data were not subject to mass transport limitations, RDE was used to collect steady state data. A Pt-disk rotating electrode was polished to a mirror finish with 0.05 μ m α -alumina (CH Instruments). Prior to film deposition, the Pt disk was electrolyzed at 1.4 V (vs NHE) in 1 M KB_i, pH 9.2 electrolyte for 30 min to anodize the Pt surface exhaustively as to minimize current arising from platinum oxide formation upon application of a potential step. Following this pre-treatment, catalyst films were deposited

onto the Pt RDE in an otherwise identical manner to that described above. Tafel data were collected in KB_i/KNO_3 electrolyte with E_{appl} stepped from 1.13 to 1.00 V in 7–20 mV increments. At each potential step, steady-state data were collected at rotation rates (ω) of 2000 and 600 rpm; data were also collected in the absence of disk rotation, but in a well-stirred solution. Background currents arising from the OER at the Pt RDE itself are insignificant compared to currents due to the OER mediated by NiB_i . The excellent agreement among Tafel slopes (28 mV/decade) under these disparate conditions reveal that Tafel data are not limited by mass transport over the current/potential range explored. In addition, these experiments demonstrate that the kinetic profile of the catalyst does not depend on the nature of the underlying substrate.

Tafel data in the absence of excess supporting electrolyte. Tafel data were acquired as in subheading B, with the exception that electrolytes contained only KB_i and no KNO_3 . Tafel data were collected in 0.1, 0.2, 0.5 and 1.0 M KB_i , pH 9.2 electrolyte. Apparent Tafel slopes decrease from 40 to 35 mV/decade as the borate concentration (and ionic strength of the electrolyte) increases.

Supporting electrolyte effect. The surface of a 0.2 cm^2 FTO-coated glass electrode was exposed by application a 1 cm wide piece of scotch tape to isolate a $2.0 \text{ mm} \times 1.0 \text{ cm}$ strip. The solution resistances of six electrolytes, each containing 0.1 M KB_i at pH 9.2, with varying concentrations of KNO_3 from 0–2 M were measured using the iR test function. Without disturbing the relative positions of the working and reference electrodes, a 1.0 mC cm^{-2} catalyst film was deposited and anodized. Following anodization, the catalyst film was operated in each solution at a fixed current density of 0.4 mA cm^{-2} . In this galvanostatic experiment, the potential required to sustain this current density was recorded after at least 300 s had elapsed. Potential values were then corrected for iR drop using the measured solution resistances. Prior to operation in each electrolyte, the catalyst film was briefly rinsed in fresh electrolyte of identical composition, to avoid cross-contamination. KNO_3 concentrations $\geq 1 \text{ M}$ were found to be

sufficient to eliminate any diffuse double layer effects and attendant complications arising from elevated local concentrations of borate anions.

Open circuit decay transients. NiB_i films were prepared as described in subheading C. Following deposition, the films were immersed in KB_i/KNO₃ pH 9.2 electrolyte and held at 1.1 V (vs. NHE) for 10 s, after which E_{appl} was removed. This short duration was sufficient for the current to plateau without the onset of anodization. A second potentiostat, which was connected in parallel, was used to measure the voltage across the working and reference electrodes throughout the potential bias and for 2 min subsequent to the removal of E_{appl} (open circuit). The sampling interval was 5 ms. The open circuit potential (OCP) was plotted as a function of time. The electrode was then rinsed in water and anodized in 1 M KB_i pH 9.2 electrolyte. Following anodization, films were immersed in KB_i/KNO₃ pH 9.2 electrolyte and the open circuit decay experiment was repeated, this time with a sampling interval of 2.5 ms. The open circuit potential was plotted as a function of time. These transients were fit to eq. 3.1 to extract the Tafel slopes for OER for anodized and non-anodized films. The OCP transients were also converted into Tafel plots using eq. 3.2.

Borate Dependence Studies. To determine the reaction order in borate, solutions were prepared with B_i concentrations in the range of 0.63–6.3 mM. An appropriate amount of KNO₃ was added to ensure an ionic strength of 2 M. The solution resistance of each electrolyte was recorded without disturbing the relative positions of the working and reference electrodes, and then a 1.0 mC cm⁻² catalyst film was deposited onto a Pt RDE. Following anodization, the catalyst film was operated at 1.05 V in each solution at $\omega = 2500, 1600, 900$ and 625 rpm. At each rotation rate, the current was allowed to reach its steady-state value before proceeding to the next rate. Prior to operation in each electrolyte, catalyst was rinsed in fresh electrolyte of identical composition to avoid cross-contamination. The experiment was then repeated at 1.04 V and 1.06 V. Ohmic losses due to solution resistance accounted for <1 mV and they were therefore neglected. Appreciable changes in current values with ω were observed for electrolytes of low buffer strength ($[B_i] < 40$ mM), implying that the reaction was not purely activation controlled.

As such, Koutecký–Levich (K–L) plots (i^{-1} as a function of $\omega^{-1/2}$) were constructed to allow for extraction of activation–controlled currents by linear extrapolation to the limit of an infinitely high rotation rate. $\log j$ was plotted as a function of $\log [B_i]$ over the $[B_i]$ range 0.63 M–40 mM. In electrolytes of very low buffer strength ($[B_i] < 40$ mM), a slope of ca. zero is observed.

pH dependence studies in B_i electrolyte. A 0.2 cm^2 ($1 \text{ cm} \times 2 \text{ mm}$) area of an FTO–coated glass electrode was isolated with scotch tape and a 1 mC cm^{-2} catalyst film was deposited. The electrode was operated at a current of $2 \text{ }\mu\text{A}$ (equivalent to $10 \text{ }\mu\text{A cm}^{-2}$) in 100 mM KB_i 2 M KNO_3 , pH 8.5 electrolyte. The steady state electrode potential (measured after operation for ≥ 2 min at each pH) was recorded as the pH of the solution was raised up to pH 12.0 in increments of about 0.1 pH units using μL aliquots of 10% KOH solution. Ohmic potential losses amounted to <0.1 mV and they were ignored. Additionally, at these very low current densities, no local pH gradients arise even when the pH is adjusted outside of the ideal B_i buffering regime. The steady-state electrode potential was plotted as a function of pH.

A 1.0 mC cm^{-2} catalyst film was prepared onto a Pt RDE. Tafel data were collected in electrolytes with B_i concentrations equal to 0.601, 0.200, 0.110, 0.101, and 0.100 M at pH 8.5, 9.2, 10.2, 11.2 and 12.0, respectively, to ensure that each electrolyte contained ~ 0.1 M borate anion, considering the $\text{p}K_a$ of 9.2 for B_i buffer. Sufficient KNO_3 was added to each solution to yield a concentration of 0.9 M, and therefore to maintain an ionic strength of 1 M. In each solution, steady state data were collected without iR compensation at 2500, 1600, 900, and 625 rpm, and where necessary, K–L analysis was used to extract activation–controlled current values. Although the measured current, and for that matter the iR drop, varied with rotation rate, the difference in these Ohmic losses due to solution resistance between different rotation rates at the same applied potential was negligible (<1 mV). The product of the previously measured solution resistance and the average current value over the rotation rate range analyzed was subtracted from the applied potential to yield the iR -corrected potential. The upper and lower limits for applied potentials were chosen such that current densities would fall between 3.5 mA cm^{-2} and $10 \text{ }\mu\text{A cm}^{-2}$. Data were recorded at potential intervals of 10 mV to yield Tafel slopes. Tafel plots

were interpolated at 2.5, 0.25 and 0.025 mA cm⁻² to furnish the potential dependence on pH at constant current density.

pK_a titrations. A 1.0 mC cm⁻² catalyst film was prepared onto an FTO-coated glass electrode (0.2 cm²), and operated at a current of 2 μA (equivalent to 10 μA cm⁻²) in 100 mM KBi, 2 M KNO₃, pH 11.3 electrolyte. The steady-state electrode potential was recorded using a Hg/HgO (1 molal NaOH) reference electrode as the pH of the solution was raised in increments of 0.2–0.25 pH units up to pH 12, with μL aliquots of 50% KOH solution. The experiment was continued in separate electrolytes of identical composition (100 mM KBi, 2 M KNO₃) whose pH had been previously adjusted to pH 12.25, 12.5, 12.8 and 13.15, respectively. Ohmic potential losses amounted to <0.1 mV in each electrolyte and could be safely ignored. The measured potentials (vs Hg/HgO) were converted to the NHE scale using $E(\text{NHE}) = E(\text{Hg/HgO}, 1 \text{ molal NaOH}) + 0.108$.⁵⁵ The corresponding overpotentials were calculated by subtracting the thermodynamic potential for the OER at each pH from the $E(\text{NHE})$ values. The steady state electrode overpotential was plotted as a function of pH at 10 μA cm⁻².

Tafel data in Bi-free electrolyte, pH 12.9, 13.8. A 1.0 mC cm⁻² catalyst film was deposited onto a Pt RDE and Tafel data were acquired in 0.1 M KOH 1.9 M KNO₃ and 1.0 M KOH 1.0 M KNO₃ solutions (pH 12.9 and 13.8, respectively). For these solutions, no mass transport limitations were encountered over the accessible overpotential range ($\eta = 220\text{--}330$ mV), and activation-controlled steady state Tafel data were acquired at a single rotation rate of 2000 rpm.

Tafel data in Bi-free electrolyte, pH 8.5. A 1.0 mC cm⁻² catalyst film was deposited onto a Pt RDE as described above. The activation-controlled steady state current density was measured with *i*R compensation as a function of applied potential by K–L analysis (see Figure S6 for a representative example) at 20 mV intervals in 1.0 M NaClO₄, pH 8.50 electrolyte. 1–5 μL aliquots of 1 M NaOH were added periodically to ensure minimal drift (± 0.01 pH units) in bulk pH over the course of the experiment. Three consecutive runs were acquired and the Tafel data were averaged. The activity of films in Bi electrolyte (0.5 M KBi, 1.75 M KNO₃, pH 9.2

electrolyte) after operation in 1 M NaClO₄ pH 8.5 were compared with Tafel data acquired using a fresh catalyst film. Since the activity of a catalyst film after operation in B_i-free electrolyte is comparable to that of a fresh film, the possibility of film corrosion causing the Tafel behavior observed in buffer-free electrolytes is excluded.

Deposition and Tafel plots of CoB_i films. CoB_i catalyst films were prepared via controlled-potential electrolysis of 0.1 M KB_i, pH 9.2 electrolyte solutions containing 0.5 mM Co²⁺. Depositions were carried out using an FTO-coated glass piece as the working electrode. These FTO-coated glass electrodes were rinsed with acetone and water prior to use in all experiments and a ~0.6 cm wide strip of Scotch tape was applied to the FTO coated side such that a 1 cm² area was exposed to solution. Deposition by controlled potential electrolysis was carried out on quiescent solutions at 0.9 V (vs. NHE) without *i*R compensation and with passage of 0.6 mC cm⁻² (equivalent to 6 nmol cm⁻² Co). A typical deposition lasted 12 s.

Current-potential data were obtained for this 0.6 mC cm⁻² CoB_i film by conducting controlled potential electrolysis in KB_i/KNO₃ pH 9.2 electrolyte at a variety of applied potentials. Prior to film deposition, the solution resistance of the electrolyte to be used for collection of Tafel data was measured using the *i*R test function. The electrolysis solution was exchanged for Co²⁺-containing KB_i electrolyte, without disturbing the relative positions of the working and reference electrodes. The film was prepared by controlled-potential electrolysis. Following film preparation, the working electrode was rinsed in fresh Co-free KB_i electrolyte and transferred, without drying, to the same electrolysis bath in which the solution resistance was measured. The electrode was allowed to equilibrate with the electrolysis solution for 5 min while being held at the open circuit potential. The solution was stirred and steady-state currents were then measured at applied potentials that descended from 1.13 V to 1.00 V in 10 mV steps. At each potential, 400 s to 600 s were allowed for the film to reach steady state. The solution resistance measured prior to the data collection was used to correct the Tafel plot for Ohmic potential losses.

3.6 References

- (1) Bediako, D. K.; Lassalle, B.; Surendranath, Y.; Yano, J.; Yachandra, V. K.; Nocera, D. G. *J. Am. Chem. Soc.* **2012**, *134*, 6801.
- (2) Gras, J. M.; Pernot, M. In *Proceedings of the Symposium on Electrode Materials and Processes for Energy Conversion and Storage*; McIntyre, J. D. E., Srinivasan, S., Will, F. G., Eds.; The Electrochemical Society: Pennington, NJ, 1977; Vol. 77–6, pp 425–440.
- (3) Conway, B. E.; Bourgault, P. L. *Can. J. Chem.* **1959**, *37*, 292.
- (4) Lu P. W.; Srinivasan, S. *J. Electrochem. Soc.* **1978**, *125*, 1416.
- (5) Bockris, J. O'M.; Otagawa, T. *J. Phys. Chem.* **1983**, *87*, 2960.
- (6) Conway, B. E.; Liu, T. *J. Chem. Soc., Faraday Trans. 1*, **1987**, *83*, 1063.
- (7) Ferreira, A. C.; Gonzalez, E. R.; Ticianelli, E. A.; Avaca, L. A.; Matvienko, B. *J. Appl. Electrochem.* **1988**, *18*, 894.
- (8) Raj, I. A.; Trivdei, D. C.; Venkatesan, V. K. *Bull. Electrochem.* **1988**, *4*, 55.
- (9) Lyons, M. E. G.; Brandon, M. P. *Int. J. Electrochem. Sci.* **2008**, *3*, 1386.
- (10) Conway, B. E.; Liu, T. C. *Mater. Chem. Phys.* **1989**, *22*, 163.
- (11) Parsons, R. In *Advances in Electrochemistry and Engineering*; Delahay, P., Tobias, C. W., Eds.; Interscience: New York, 1961; Vol. 1, pp 29–64.
- (12) Gileadi, E. *Electrode Kinetics for Chemists, Chemical Engineers, and Materials Scientists*; Wiley-VCH: New York, 1993; Ch. 13–14.
- (13) Corrigan, D. A. *J. Electrochem. Soc.* **1987**, *134*, 377.
- (14) Gileadi, E. *Electrode Kinetics for Chemists, Chemical Engineers, and Materials Scientists*; Wiley-VCH: New York, 1993; Chapter 24.

- (15) Gileadi, E. *Electrode Kinetics for Chemists, Chemical Engineers, and Materials Scientists*; Wiley-VCH: New York, 1993; Chapter 23.
- (16) Gileadi, E. *Electrode Kinetics for Chemists, Chemical Engineers, and Materials Scientists*; Wiley-VCH: New York, 1993; Chapter 10.
- (17) Bard, A. J.; Faulkner, L. R. *Electrochemical Methods: Fundamentals and Applications*, 2nd ed.; John Wiley and Sons: New York, 2001; pp 340–344.
- (18) Gileadi, E. *Electrode Kinetics for Chemists, Chemical Engineers, and Materials Scientists*; Wiley-VCH: New York, 1993; Chapter 14.
- (19) MacDonald, J. J.; Conway, B. E. *Proc. R. Soc. London* **1962**, 269, 419.
- (20) Damjanovic, A.; Jovanovic, B. *J. Electrochem. Soc.* **1976**, 123, 374.
- (21) Lyons, M. E. G.; Brandon, M. P. *Int. J. Electrochem. Sci.* **2008**, 3, 1425.
- (22) Trotochaud, L.; Ranney, J. K.; Williams, K. N.; Boettcher, S. W. *J. Am. Chem. Soc.* **2012**, 134, 17253.
- (23) Gileadi, E. *Electrode Kinetics for Chemists, Chemical Engineers, and Materials Scientists*; Wiley-VCH: New York, 1993; Ch. 17 & 19.
- (24) Goldberg, S.; Criscenti, L. J.; Turner, D. J.; Davis, J. A.; Cantrell, K. J.; *Vadose Zone J.* **2007**, 6, 407.
- (25) Peak, D.; Luther, G. W.; Sparks, D. L. *Geochem. Cosmochim. Acta* **2003**, 67, 2551.
- (26) Scharifker, B. R.; Habib, M. A.; Carbajal, J. L.; Bockris, J. O'M. *Surface Sci.* **1986**, 173, 97.
- (27) El-Shafei, A. A.; Aramata, A. *J. Solid State Electrochem.* **2007**, 11, 430–433.

- (28) Cotton F. A.; Wilkinson G.; Murillo, C.; Bochmann, M. *Advanced Inorganic Chemistry*, 6th ed.; Wiley: New York, 1999; pp 171–173.
- (29) Farmer, J. B. In *Advances in Inorganic Chemistry and Radiochemistry* Emeléus, H. J., Sharpe, A. G., Eds.; Academic Press: New York, 1982; Vol. 25, pp 187–237.
- (30) Salentine, C. G. *Inorg. Chem.* **1983**, 22, 3920.
- (31) Risch, M.; Klingan, K.; Heidkamp, J.; Ehrenberg, D.; Chernev, P.; Zaharieva, I.; Dau, H. *Chem. Commun.* **2011**, 47, 11912.
- (32) McAlpin, J. G.; Surendranath, Y.; Dincă, M.; Stich, T. A.; Stoian, S. A.; Casey, W. H.; Nocera, D. G.; Britt, R. D. *J. Am. Chem. Soc.* **2010**, 132, 6882.
- (33) Kanan, M. W.; Yano, J.; Surendranath, Y.; Dincă, M.; Yachandra, V. K.; Nocera, D. G. *J. Am. Chem. Soc.* **2010**, 132, 13692.
- (34) Choisnet, J.; Evarestov, R. A.; Tupitsyn, I. I.; Veryazov, V. A. *J. Phys. Chem. Solids* **1996**, 57, 1839.
- (35) Koyama, Y.; Kim, Y.-S.; Tanaka, I.; Adachi, H. *Jpn. J. Appl. Phys.* **1999**, 38, 2024.
- (36) Koyama, Y.; Yabuuchi, N.; Tanaka, I.; Adachi, H.; Ohzuku, T. *J. Electrochem. Soc.* **2004**, 151, A1545.
- (37) McAlpin, J. G.; Stich, T. A.; Ohlin, C. A.; Surendranath, Y.; Nocera, D. G.; Casey, W. H.; Britt, R. D. *J. Am. Chem. Soc.* **2011**, 133, 15444.
- (38) Beverskog, B.; Puigdomenech, I. *Corr. Sci.* **1997**, 39, 969.
- (39) Daggetti, A.; Lodi, G.; Trasatti, S. *Mater. Chem. Phys.* **1983**, 8, 1.
- (40) Trasatti, S. In *Electrochemistry of Novel Materials*; Lipkowski, J., Ross, P. N., Eds.; VCH: New York, 1994; Ch. 5.

- (41) Tewari, P. H.; Campbell, A.B. *J. Coll. Int. Sci.* **1976**, *55*, 531.
- (42) Faria, L.A.; Prestat, M.; Koenig, J.-F.; Chartier, P.; Trasatti, S. *Electrochim. Acta* **1998**, *44*, 1481.
- (43) Wang, L.-P.; Van Voorhis, T. *J. Phys. Chem. Lett.* **2011**, *2*, 2200.
- (44) Huynh, M. H. V.; Meyer, T. J. *Chem. Rev.* **2007**, *107*, 5004.
- (45) Constantin, C. *Chem. Rev.* **2008**, *108*, 2145.
- (46) Reece, S. Y.; Nocera, D. G. *Annu. Rev. Biochem.* **2009**, *78*, 673.
- (47) Surendranath, Y.; Kanan, M. W.; Nocera, D. G. *J. Am. Chem. Soc.* **2010**, *132*, 16501.
- (48) Tarasevich, M. R.; Efremov, B. N. In *Electrodes of Conductive Metal Oxides, Part A*; Trasatti, S., Ed.; Elsevier: Amsterdam, 1980; Ch. 5.
- (49) Trasatti, S. In *Electrochemistry of Novel Materials*; Lipkowsky, J., Ross, P. N., Eds.; VCH: New York, 1994; Ch. 5.
- (50) Kinoshita, K. *Electrochemical Oxygen Technology*; Wiley-Interscience: New York, 1992; Ch. 2.
- (51) Lyons, M. E. G.; Brandon, M. P. *Int. J. Electrochem. Sci.* **2008**, *3*, 1425.
- (52) Man, I. C.; Su, H.-Y.; Calle-Vallejo, F.; Hansen, H. A.; Martínez, J. I.; Inoglu, N. G.; Kitchin, J.; Jaramillo, T. F.; Nørskov, J. K.; Rossmeisl, J. *ChemCatChem* **2011**, *3*, 1159.
- (53) Suntivich, J.; May, K. J.; Gasteiger, H. A.; Goodenough, J. B.; Shao-Horn, Y. *Science* **2011**, *334*, 1383.
- (54) Subbaraman, R.; Tripkovic, D.; Chang, K.-C.; Strmcnik, D.; Paulikas, A. P.; Hirunsit, P.; Chan, M.; Greenley, J.; Stamenkovic, V.; Markovic, N. M. *Nat. Mater.* **2012**, *11*, 550.

- (55) Nickell, R. A.; Zhu, W. H.; Payne, R. U.; Cahela, D. R.; Tatarchuk, B. J. *J. Power Sources* **2006**, *161*, 1217.

Chapter 4 — Interplay of oxygen evolution kinetics and photovoltaic power curves on the construction of artificial leaves

Portions of this chapter have been published:

Surendranath, Y.; Bediako, D. K.; Nocera, D. G. *Proc. Natl. Acad. Sci. U.S.A.*, [Online early access]. DOI: 10.1073/pnas.1118341109. Published Online: June 11, 2012. <http://www.pnas.org> (accessed January 5, 2013). – Reproduced by permission of the National Academy of Sciences, USA

large enough to drive water splitting. Thin-film ohmic contacts are at the termini of this stack to both protect the semiconductor from the chemistries occurring in solution and to enable efficient charge transfer to catalyst overlayers, which execute the oxygen evolution reaction (OER) and hydrogen evolution reaction (HER).

Whereas water splitting catalysis is combined with charge separation, current rectification, and photovoltage generation in a solution junction PEC device, in a buried junction device, catalysis is separated from the current rectification, charge separation, and photovoltage generation, which occur at the internal junction. In contrast to a solution junction, the photovoltages produced at buried junctions are free to float and are not fixed relative to a material-specific flatband potential.² Thus, for buried junction devices, there is no requirement that the flatband potentials of the semiconductors result in band edges that straddle the thermodynamic potentials of the OER and HER under the conditions of operation. This fact dramatically expands the number of light-absorbing materials available for buried junction PEC water splitting. Additionally, as the buried junction device represents a photovoltaic power source in series with an electrochemical load, the OER and HER catalysts may be optimized independently such that maximum power transfer occurs to drive water splitting. We elaborate here on this latter issue and show that the kinetic profile of the catalyst is a key determinant of the overall solar-to-fuels efficiency (SFE).

We interrogate here the interplay of OER catalysis and photovoltaic performance in defining SFE of the artificial leaves based on Ni-B_i and Co-B_i catalysts. Building on the theoretical work of Hanna and Nozik⁶ and adapting the engineering loss analysis model of Rocheleau and Miller,⁷ we use Ni-B_i and Co-B_i electrokinetic data as a basis for modeling the electrochemical load of water splitting in a PEC cell. We show that Ni-B_i and Co-B_i exhibit markedly different Tafel slopes pointing to different mechanisms of oxygen evolution, which translate into disparate electrochemical loads for water splitting. By assembling the electrochemical profiles of Ni-B_i and Co-B_i systems with multi-junction PV components of similar power conversion efficiency but disparate open-circuit voltages, V_{oc} , we show that OER

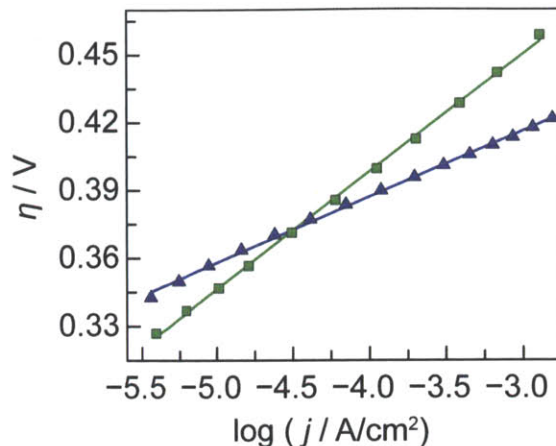


Figure 4.2. Tafel plot, $\eta = (V_{\text{appl}} - iR - E^0)$, of a Ni-B_i catalyst film operated in 0.5 M B_i, pH 9.2 (▲), and a Co-B_i catalyst film operated in 1 M B_i, pH 9.2 (■). E^0 is the thermodynamic potential water splitting under the conditions of the experiment, η is the overpotential, iR accounts for the uncompensated cell resistance. The slopes of the linear fits to the data are 52 mV/decade and 29 mV/decade for Co-B_i and Ni-B_i, respectively.

catalyst kinetics is a key determinant of SFE when water splitting is performed near its thermodynamic limit (i.e. low V_{oc}). This observation has not broadly been appreciated previously because most PEC cells have employed semiconducting materials with large bandgaps that provide high voltages that are energetically far removed from the thermodynamic limit of water splitting.

4.2 Results

4.2.1 Catalyst Film Electrosynthesis

Water splitting catalysts were deposited as thin films by controlled potential electrolysis of Co^{2+} and Ni^{2+} solutions in 0.1 M potassium borate electrolyte, pH 9.2 (B_i) at a potential of 0.92 and 1.15 V (vs. the normal hydrogen electrode, NHE), respectively.⁸⁻¹¹ Following electrodeposition, Co films were rinsed and placed in electrolyte containing no additional Co to yield steady state current density values that are unchanged over time. The log of the steady state current density of Co-B_i films versus the applied overpotential exhibited good linearity over ~2.5 decade range in current density and yielded a Tafel slope of 52 mV/decade (Figure 4.2). This

Tafel slope is similar to those previously observed for films grown from phosphate electrolyte at pH 7,¹² and it is diagnostic of a mechanism involving an equilibrium of a one electron reaction that precedes a rate limiting chemical step for oxygen evolution.

In contrast to Co-B_i films, which exhibit high initial OER activity that is sustained indefinitely, Ni-B_i requires preconditioning by anodic polarization in order to obtain steady state current densities that are high and remain unchanged over time.¹¹ Over the course of this anodic preconditioning, Ni-B_i films exhibit a dramatic rise in activity and undergo structural changes reminiscent of a β-NiOOH to γ-NiOOH phase conversion.¹¹ The logarithm of the steady state current density of preconditioned Ni-B_i films *versus* the applied overpotential exhibits good linearity over ~2.5 decade range in current density and yields a Tafel slope of 29 mV/decade (Figure 4.2), in contrast to the value observed for Co-B_i under similar conditions. A thorough mechanistic investigation of thin Ni-B_i films (Chapter 3) reveals that the low Tafel slope for Ni implies a mechanism involving a two electron equilibrium prior to the rate limiting step of oxygen evolution, as opposed to the one-electron pre-equilibrium observed for the Co-B_i catalyst.¹³

4.2.2 *j*-*V* Modeling of Buried-Junction Semiconductor-Catalyst Assemblies

The disparate Tafel behaviors of Ni and Co films are paramount to determining the anodic electrochemical load in an artificial leaf. Specifically, the electrochemical load of water splitting is described by the following equation:⁷

$$V_{\text{op}}(j) = E^0 + \eta_{\text{OER}}(j) + \eta_{\text{HER}}(j) + \eta_{\Omega}(j) \quad (4.1)$$

where V_{op} is the overall operational voltage necessary for water splitting at a given current density j , E^0 is the thermodynamic potential stored in water splitting, 1.23 V under standard conditions, and η_{Ω} represents the voltage required to overcome resistive losses in the device including contact resistance between the components and ion transport resistance arising from the electrolyte solution. Typically these resistances are ohmic and therefore can be represented by the simple product of the net current and an aggregate cell resistance, R . The η_{OER} and η_{HER}

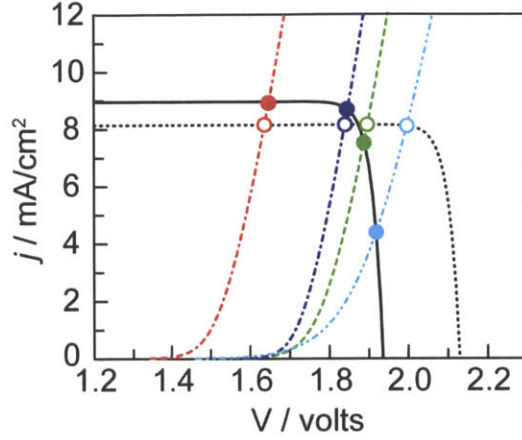


Figure 4.3. Electrochemical load of water splitting utilizing Co-B_i (green — — —), Ni-B_i (blue — — —), RuO₂ (red — — —), and LaMnO₃ (light blue — — —) oxygen evolution catalysts and the j - V curve of an idealized model of an a-Si|nc-Si|nc-Si triple junction photovoltaic displaying $V_{oc} = 1.94$ V, $j_{sc} = 8.96$ mA cm⁻² (black —) and an idealized hypothetical cell possessing $V_{oc} = 2.13$ V, $j_{sc} = 8.15$ mA cm⁻² (black — — —). Open circles indicate operating current densities for the high V_{oc} cell and correspond to 10% SFE for all catalysts. Close circles indicate operating current densities for the low V_{oc} cell for which SFE is sensitive to catalyst performance.

terms represent the overpotential losses accompanying the oxygen evolution and proton reduction half reactions, respectively, and they are illustrated in Figure 4.1. Both overpotential terms are functions of the current density as given by the Tafel law,

$$\eta = b \log\left(\frac{j}{j_0}\right) \quad (4.2)$$

in which b is the Tafel slope and j_0 is the exchange current density, representing the extrapolated rate at which the forward and back reactions occur under conditions of zero driving force, $\eta = 0$.

Combining eqs. 4.1 and 4.2 with consideration of the ohmic nature of the cell resistance term engenders the following expression for the electrochemical load of water splitting,

$$V_{op}(j) = 1.23 + b_{OER} \log\left(\frac{j}{j_{0,OER}}\right) + b_{HER} \log\left(\frac{j}{j_{0,HER}}\right) + jR \quad (4.3)$$

In this expression, b_{OER} , $j_{0,OER}$, b_{HER} and $j_{0,HER}$ represent the Tafel slopes and exchange current densities of the oxygen evolution and proton reduction catalysts, respectively. In order to isolate the impact of disparate OER catalyst kinetics, we chose to model the hydrogen evolution catalyst using values typical of the HER on high surface area Ni electrodes^{14,15} and similar to those used in the artificial leaf,^{16,17} $j_{0,HER} = 10$ μ A cm⁻² and $b_{HER} = 30$ mV/decade,¹⁴ and to assume a

conservative value of $R = 10 \ \Omega$. Extrapolation of the Tafel data in Figure 4.2 yields exchange current densities for Co-B_i and Ni-B_i of 2.1×10^{-12} and 5.0×10^{-18} A cm⁻², respectively. These values, taken together with the Tafel slopes of the two catalysts yields the current density–voltage curves shown in Figure 4.3 for water splitting by Co-B_i and Ni-B_i. Consistent with the larger exchange current density for Co-B_i, the onset of appreciable water splitting occurs at a lower potential relative to Ni-B_i. However, the lower Tafel slope of Ni-B_i causes its j – V curve to rise far more steeply, requiring a lower voltage at high current density. In this treatment, we assume that the Tafel behavior shown in Figure 4.2 is retained over the entire overpotential range and acknowledge that mass transport limitations and/or changes in OER mechanism at high overpotential may perturb the theoretical j – V behavior in Figure 4.3.

As further points of comparison, published Tafel data for RuO₂¹⁸ and LaMnO₃¹⁹ in 1 M NaOH are also overlaid on the graph to model the electrochemical load of water splitting using these catalysts. The reported Tafel data for RuO₂ and LaMnO₃ correspond to materials prepared by high temperature calcination of metal salt precursors at >350 °C. As such, these materials may not be suitable for integration into PV–PEC architectures, and we therefore include them in Figure 4.3 as exemplars of high and low performance OER catalysts and thus they provide a benchmark for the impact of catalyst performance on SFE.

4.3 Discussion

In the artificial leaf, the operating current density is given by the intersection of the j – V curve for the PV and the j – V curve representing the electrochemical load for water splitting. This operating current density multiplied by the thermodynamic potential of water splitting, 1.23 V, defines the power stored in water splitting and the ratio of this power to the incident power of the solar flux, 100 mW/cm², defines the SFE. For the purposes of illustration, we model in Figure 4.3 the idealized PV behavior of a triple junction amorphous Si(a-Si) | nanocrystalline Si(nc-Si) | nanocrystalline Si(nc-Si) triple junction cell stack²⁰ exhibiting $V_{oc} = 1.94$ V and $j_{sc} = 8.96$ mA cm⁻², and a hypothetical multi-junction cell with a $V_{oc} = 2.13$ V and $j_{sc} = 8.15$ mA cm⁻².

Idealized behavior of the PV is modeled by ignoring efficiency losses due to high series or low shunt resistances and assuming a diode ideality factor of 1 (details of PV modeling provided in the Section 4.5). Both idealized cells exhibit a power conversion efficiency of 16%, but display dramatically different SFEs when paired with the various OER catalysts.

For the cell possessing the lower V_{oc} , the electrochemical load curves for water splitting using Ni-B_i and Co-B_i intersect the j - V curve of the PV at 1.85 and 1.89 V (Figure 4.3), respectively, which is beyond the maximum power point ($V_{mp} = 1.83$ V) of the PV. As the PV current density declines sharply beyond V_{mp} , an artificial leaf utilizing Co-B_i is expected to exhibit a lower hydrogen production current density (7.6 mA cm^{-2}) than one utilizing Ni-B_i (8.7 mA cm^{-2}). Water splitting stores 1.23 V and, thus, these current densities translate to SFE = 9.3% and 10.7% for Co-B_i and Ni-B_i, respectively. The SFE declines further for the case of LaMnO₃, which displays an overall water splitting current density of 4.4 mA cm^{-2} and a SFE = 5.4%. In contrast, RuO₂, despite displaying greater OER catalytic activity than thin film Co-B_i and Ni-B_i, exhibits only a marginally larger SFE = 11.1%. The artificial leaf becomes even more insensitive to OER catalytic activity if the V_{oc} of the PV can be increased (Figure 3). For the higher V_{oc} cell, all of the catalysts exhibit SFE = 10.0%, highlighting the fact that good catalyst performance and high SFE is only mandated if a suitable PV with a V_{mp} matched to the electrochemical load can be designed near the thermodynamic potential of water splitting.

The forgoing analysis assumes that the PV exhibits ideal diode behavior with minimal series and maximal shunt resistances. In practice, multi-junction Si devices suffer from poor fill factors symptomatic of non-ideal diode behavior and parasitic resistance losses.²⁰ Thus, we stress that the trends observed here are purely theoretical and that a more rigorous analysis performed on a specific PV/catalyst pairing would be necessary for device optimization. We do note however, in a practical artificial leaf with minimized ohmic losses, an overall SFE = 5.2% has been observed for a PV cell of 7.7% efficiency.¹⁶

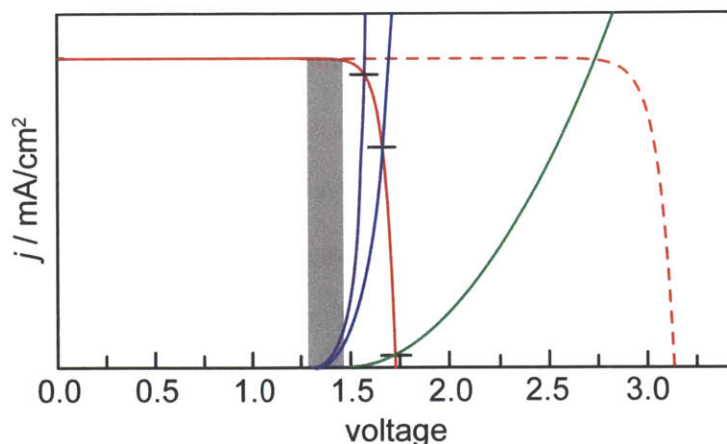


Figure 4.4. Low SFE (red, — — with green, —) and high SFE PEC cells (red, — with blue, — or purple, —). The j - V curves of a PV (red, — —) for a typical metal oxide semiconductor operating ($V_{oc} > 3.0$ V) and a PV (red, —) operating near the region of thermodynamic potential (gray bar) at arbitrary current density j overlaid with Tafel curves of catalysts exhibiting increasing slope, i.e. increasing catalyst performance (green, — to blue, — to purple, —). Note the sensitivity of the overall SFE to catalyst performance for PVs operating near thermodynamic potential.

4.4 Conclusion

In summary, we illustrate here that a key determinant of high SFE for artificial leaves, and more generally, photoelectrochemical cells, is the OER kinetic profile. In particular, thin Ni-B_i catalyst films exhibit a 29 mV/decade Tafel slope as compared to a 52 mV/decade slopes observed for Co-B_i under similar electrolyte conditions. The disparate kinetics of Co-B_i and Ni-B_i translate into improved SFE of an artificial leaf utilizing the latter, suggesting that Ni-B_i is particularly well-suited to direct solar-to-fuels generation.

We note that the critical role of catalysis in SFE has generally been under-appreciated because PEC cells to date have generally relied on semiconducting materials with large bandgaps (e.g., SrTiO₃, TiO₂, WO₃ display bandgaps, $E_g > 2.5$ V) which supply very high voltages to drive water splitting.²¹ These materials have typically been used as components of solution junction PEC devices rather than buried junction devices complicating their analysis using the simple power matching model presented here.²² Notwithstanding, extremely poor catalytic activity of semiconducting oxides such as SrTiO₃, TiO₂ and WO₃ can be masked by the large voltages they

deliver to drive water splitting via high overpotential pathways (e.g. hydroxyl radical formation).^{21,23} As illustrated in Figure 4.4, qualitatively, large band gap oxide PEC devices can be viewed as exaggerated cases of the high V_{oc} PV we model in Figure 4.3, wherein, load curves for poor catalysts still intersect the j - V curve of the semiconductor at or below the V_{mp} . The maximum SFE of such cells, however is intrinsically limited owing to inefficient utilization of the solar spectrum. High SFEs can only be achieved for PVs operating near the thermodynamic potential of water splitting so that the absorption of the solar spectrum can be maximized. In this case, as illustrated in Figures 4.3 and 4.4, the overall SFE becomes extremely sensitive to catalyst performance.

These results show that the construction of efficient PEC devices such as the artificial leaf reduces to a problem of catalyst design. To this end, Co-B_i and Ni-B_i are ideal water splitting catalysts when integrated to well-designed Si-junctions or other PV cells operating near the thermodynamic potential for water splitting. The results herein show that SFEs = 10% are easily within reach if Co-B_i and Ni-B_i catalysts are integrated with PV cells operating at 15% efficiency thus highlighting the promise of artificial leaves as a low cost method for direct solar-to-fuels production.

4.5 Experimental Methods

Materials. Ni(NO₃)₂•6H₂O 99.9985% was used as received from Strem. H₃BO₃ (99.5%), and KOH (85%) were used as received from Sigma-Aldrich. NaOH (99%) and KNO₃ (99%) were used as received from Mallinckrodt. All buffers were prepared with reagent grade water (Ricca Chemical, 18 MΩ-cm resistivity) or Millipore Type-I. Fluorine-tin-oxide (FTO) coated glass slides (TEC-7) were purchased as pre-cut pieces from Hartford Glass.

Electrochemical methods. All electrochemical experiments were performed at ambient temperature with a CH Instruments 760D potentiostat and a BASi Ag/AgCl reference electrode. All electrode potentials were converted to the NHE scale using $E(\text{NHE}) = E(\text{Ag/AgCl}) + 0.197$ V. Unless otherwise stated, the electrolyte was 0.1 M potassium borate at pH 9.2 (B_i).

Co-B_i catalyst film formation and Tafel data collection. Bulk electrolyses were performed in a two-compartment electrochemical cell with a glass frit junction of fine porosity. For catalyst electrodeposition, the auxiliary compartment was charged with ~50 mL of 0.1 M B_i electrolyte and the working compartment was charged with ~50 mL of solution comprising 25 mL of 0.2 M B_i electrolyte and 25 mL of 1 mM Co²⁺ solution. The working electrode was a 1 cm × 2.5 cm piece of FTO-coated glass. The FTO coated side was masked so as to expose a 1 cm² area of the electrode to the solution. Pt mesh was used as the auxiliary electrode. Electrolysis was carried out at 0.92 V on quiescent solutions without *iR* compensation and with the reference electrode situated 2–3 mm from the ITO surface. Electrolysis was continued until 24 mC of charge were passed.

Tafel data were obtained by conducting controlled-potential electrolysis in 1 M B_i electrolyte at a variety of applied potentials. Prior to film deposition, the solution resistance of the 1 M KB_i electrolyte to be used for Tafel data collection was measured using the *iR* test function. The electrolysis solution was exchanged with Co²⁺-containing 0.1 M B_i electrolyte, without disturbing the relative positions of the working and reference electrodes. The film was prepared by controlled-potential electrolysis as described above. Following film preparation, the working electrode was rinsed in reagent grade water, and transferred without drying, to the same electrolysis bath in which the solution resistance was measured. The electrode was allowed to equilibrate with the electrolysis solution for 5 min while being held at the open circuit potential. The solution was stirred and steady-state currents were then measured at applied potentials that descended from 1.17 V to 0.96 V in 10–30 mV steps. For currents greater than 10 μA cm⁻², a steady state was reached at a particular potential in 400–600 s. For currents lower than 10 μA cm⁻², longer electrolysis times (15–20 min) were utilized to ensure that steady state conditions had been achieved. The solution resistance measured prior to the data collection was used to correct the Tafel plot for ohmic potential losses.

Ni-B_i catalyst film formation, anodization, and Tafel data collection. Ni-B_i catalyst films were prepared by controlled-potential electrolysis of 0.1 M B_i electrolyte solutions

containing 0.4 mM Ni²⁺. To minimize precipitation of Ni(OH)₂ from these solutions, 25 mL of 0.2 M B_i was added to 25 mL of 0.8 mM Ni²⁺ solution. The deposition solutions were subsequently filtered through a 0.2 μm syringe filter (Pall Inc.) to remove any precipitated Ni(OH)₂ that formed. The solutions thus prepared remained clear over the course of all depositions, which were carried out using an FTO-coated glass piece as the working electrode. These FTO-coated glass electrodes were rinsed with acetone and water prior to use in all experiments and the FTO-coated side was masked so as to expose a 1 cm² area of the electrode to the solution. Deposition by controlled-potential electrolysis was carried out on quiescent solutions at 1.15 V without *i*R compensation and with passage of 1 mC cm⁻². A typical deposition lasted 70 s. Following deposition, films were rinsed with 0.1 M B_i and subsequently anodized in 1 M B_i electrolyte by passage of 3.5 mA cm⁻² for 1 h with stirring.

Current–potential data were obtained by conducting controlled potential electrolysis in 0.5 M B_i 1.75 M KNO₃ electrolyte at a variety of applied potentials. Prior to film deposition and anodization, the solution resistance of the electrolyte to be used for Tafel data collection was measured using the *i*R test function. The electrolysis solution was exchanged for Ni²⁺–containing B_i electrolyte, without disturbing the relative positions of the working and reference electrodes. The film was prepared by controlled-potential electrolysis and anodized as described above. Following film preparation, the working electrode was rinsed in fresh Ni–free B_i electrolyte and transferred, without drying, to the same electrolysis bath in which the solution resistance was measured. The electrode was allowed to equilibrate with the electrolysis solution for 5 min while being held at the open circuit potential. The solution was stirred and steady–state currents were then measured at applied potentials that descended from 1.1 V to 1.00 V in 7–20 mV steps. For currents greater than 10 μA cm⁻², a steady state was reached at a particular potential in less than 400 sec. For currents lower than 10 μA cm⁻², longer electrolysis times (15–20 min) were utilized to ensure that steady state conditions had been achieved. The solution resistance measured prior to the data collection was used to correct the Tafel plot for ohmic potential losses.

j - V curve modeling. The j - V curve representing the electrochemical load of water splitting was calculated using eq. 3 over a current density range from 10^{-5} A cm $^{-2}$ to 10^{-1} A cm $^{-2}$. A 10 Ω cell resistance was assumed along with $j_{0,HER} = 10 \mu\text{A cm}^{-2}$ and $b_{HER} = 30$ mV/decade. The Tafel slopes and exchange current density values for Co-B $_i$ and Ni-B $_i$ were taken from linear fits to the data in Figure 2 whereas Tafel slopes and exchange current density values were taken published data for RuO $_2$ ¹⁸ and LaMnO $_3$.¹⁹

The j - V curve representing idealized power output from a triple junction Si photovoltaic stack was modeling using reported data for a a-Si|nc-Si|nc-Si cell²⁰ which exhibits $V_{oc} = 1.94$ V and $j_{sc} = 8.96$ mA cm $^{-2}$ (Figure 3). These two experimental parameters were used to calculate the dark saturation current of an idealized cell, j_0 , using the following equation:

$$j_0 = \frac{j_{sc}}{\exp\left(\frac{qV_{oc}}{nkT}\right) - 1} \quad (4)$$

where q is the fundamental charge of an electron, k is the Boltzmann factor, T is the temperature, taken as 300 K, and n is the diode ideality factor, taken as 1. Using the calculated value of j_0 , the ideal j - V curve is calculated using

$$j = j_{sc} - j_0 \left(\exp\left(\frac{qV}{nkT}\right) - 1 \right) \quad (5)$$

The same analysis was applied to a hypothetical idealized cell with a 10% increase in V_{oc} and a concomitant 10% decrease in j_{sc} so to preserve the same overall power conversion efficiency of 16%. We note that the above equations produce upper limit ideal behavior because they do not account for parasitic resistances that may exist within or between the individual p-n junction components of the triple junction stack.

4.6 References

- (1) Weber, M. F.; Dignam, M. J. *Int. J. Hydrogen Energy* **1986**, *11*, 225.

- (2) Walter, M. G.; Warren, E. L.; McKone, J. R.; Boettcher S. W.; Mi, Q.; Santori, E. A.; Lewis, N. S. *Chem. Rev.* **2010**, *110*, 6446.
- (3) Miller, E. L.; Marsen, B.; Paluselli, D.; Rocheleau, R. *Electrochem. Sol. State Lett.* **2005**, *8*, A247.
- (4) Miller, E. L.; Rocheleau, R. E.; Deng, X. M *Int. J. Hydrogen Energy* **2003**, *28*, 615.
- (5) Rocheleau, R. E.; Miller, E. L.; Misra, A. *Energy Fuels* **1998**, *12*, 3.
- (6) Hanna, M. C.; Nozik, A. J. *J. Appl. Phys.* **2006**, *100*, 074510.
- (7) Rocheleau, R. E.; Miller, E. L. *Int. J. Hydrogen Energy* **1997**, *22*, 771.
- (8) Kanan, M. W; Nocera, D. G. *Science* **2008**, *321*, 1072.
- (9) Surendranath, Y.; Dincă, M.; Nocera, D. G. *J. Am. Chem. Soc.* **2009**, *131*, 2615.
- (10) Dincă, M.; Surendranath, Y.; Nocera, D. G *Proc. Natl. Acad. Sci. USA* **2010**, *107*, 10337.
- (11) Bediako, D. K.; Lassalle, B.; Surendranath, Y.; Yano, J.; Yachandra, V. K.; Nocera, D. G. *J. Am. Chem. Soc.* **2012**, *134*, 6801.
- (12) Surendranath, Y.; Kanan, M. W.; Nocera, D. G. *J. Am. Chem. Soc.* **2010**, *132*, 16501.
- (13) Surendranath, Y.; Nocera, D. G. *Prog. Inorg. Chem.* **2011**, *57*, 505.
- (14) Conway, B. E.; Bai, L. *Int. J. Hydrogen Energy* **1986**, *11*, 533.
- (15) Conway, B. E.; Tilak, B. V. *Electrochim. Acta* **2002**, *47*, 3571.
- (16) Reece, S. Y.; Hamel, J. A.; Sung, K.; Jarvi, T. D.; Esswein, A. J.; Pijpers, J. J. H.; Nocera, D. G. *Science* **2011**, *334*, 645.
- (17) Nocera, D. G. *Acc. Chem. Res.* **2012**, *45*, 767.

- (18) Burke, L. D.; Murphy, O. J.; O'Neill, J. F.; Venkatesan, S. *J. Chem. Soc. Faraday Trans. 1* **1977**, *73*, 1659.
- (19) Bockris, J. O.; Otagawa, T. *J. Electrochem. Soc.* **1984**, *131*, 290.
- (20) Green, M. A., Emery, K., Hishikawa, Y., Warta, W., Dunlop, E. D. *Prog. Photovol.* **2011**, *19*, 565.
- (21) Grimes, C.A.; Varghese, O. K.; Ranjan, S. *Light, Water, Hydrogen: The Solar Generation of Hydrogen by Water Photoelectrolysis*; Springer: New York, 2008, Ch 4.
- (22) Bockris, J. O. M.; Szklarczyk, M.; Contractor, A. Q.; Khan, S. U. M. *Int. J. Hydrogen Energy* **1984**, *9*, 741.
- (23) Boddy, P. J. *J. Electrochem. Soc.* **1968**, *115*, 199.

The author was born Daniel Kwabena Ogyam Dakwa Bediako to Kwame Manasseh Bediako and Gillian Mary Bediako midday Tuesday, June 3, 1986 at the Family Clinic, Adabraka, Ghana. His primary school education was begun at the Okuapeman School in Akropong-Akuapem and completed at the Akosombo International School (AIS), both in the Eastern Region of Ghana. He attended AIS throughout his high school years, and it was there that he gained an appreciation for, and love of, chemistry, in no small part due to the tutelage of Mr. Charles Karikari. Kwabena continued his interest in chemistry in 2004 when he began undergraduate studies at Calvin College in Grand Rapids, MI, USA. In these formative years of his scientific scholarship, he was drawn to the colorful world of inorganic chemistry and researched the coordination chemistry of aqueous nickel(II) pyridyl complexes in the laboratory of Professor Douglas Vander Griend. In the summer of 2007 he interned with UOP, a Honeywell company, in Des Plaines, IL, USA, where he explored the catalytic dehydrogenation of propane in the Oleflex™ process. After receiving his B.S. with Honors in Chemistry, he returned to UOP in 2008 as an intern to study catalysis of the methanol-to-olefin (MTO) process mediated by silico-alumino-phosphate (SAPO) molecular sieves and the selective hydrogenation of phenols using carbon-supported palladium catalysts. In 2009, he began his graduate studies at the Massachusetts Institute of Technology, Cambridge, MA in the laboratory of Professor Daniel G. Nocera. His Master's thesis work has focused on exploring the structure and catalytic mechanism of nickel-based thin-film oxygen evolution catalysts. Kwabena is continuing his graduate studies in solar-driven water splitting and is currently pursuing a PhD in inorganic chemistry with Professor Nocera at Harvard University.

D. KWABENA BEDIAKO

Massachusetts Institute of Technology
 Department of Chemistry
 77 Massachusetts Ave., Rm. 18-252
 Cambridge, MA 02139

Email: bediako@mit.edu
 Phone: (617) 258-8120

Education

Master of Science *Massachusetts Institute of Technology*
 Advisor: Professor Daniel G. Nocera expected February **2013**
Thesis Title: Structural and Mechanistic Studies of Nickel–Borate Thin-Film Oxygen Evolving
 Electrocatalysts
 GPA: 4.90/5.0

B.S. with Honors Chemistry Calvin College
 Advisor: Professor Douglas Vander Griend May **2008**
Thesis Title: Self-assembly of nickel(II) pyridyl complexes into supramolecular motifs
 GPA: 3.914/4.0

Awards and Fellowships

Fellow, Martin Family Society of Fellows for Sustainability, <i>MIT</i>	2012–2013
Saudi Aramco-MIT Energy Fellowship, <i>MIT</i>	2009–2010
Outstanding Teaching by a Graduate Student Award, <i>MIT</i>	2010
Chesonis Family Foundation Solar Revolution Project Fellow	2011–2012
The Karen J. Carlson Muyskens Outstanding Senior in Chemistry Award, <i>Calvin College</i>	2009
Presidential Scholarship, <i>Calvin College</i>	2004–2008
The Dr. Enno and Mrs. Lucile Wolthuis Chemistry Scholarship, <i>Calvin College</i>	2005, 2007
The James and Beatrice Harkema Family Scholarship, <i>Calvin College</i>	2007
The John and Lillian Van Oosten Scholarship, <i>Calvin College</i>	2006
ACS Analytical Chemistry Undergraduate Award,	2006
McGregor Sophomore Scholar, <i>Calvin College</i>	2005
Department of Chemistry and Biochemistry Outstanding Freshman Award, <i>Calvin College</i>	2004
Best Senior Secondary School Certificate Exam Results, <i>Akosombo International School</i> ,	2003
Best Results in the Cambridge GCE O-Level Examinations, <i>British Council Ghana</i>	2002

Scientific Publications

- (6) Surendranath, Y.; **Bediako, D. K.**; Nocera, D. G. *Proc. Natl. Acad. Sci. U.S.A.* **2013**, *in press* (DOI: 10.1073/pnas.11183411109).
 “Interplay of oxygen evolution kinetics and photovoltaic power curves on the construction of artificial leaves”
- (5) **Bediako, D. K.**; Lassalle-Kaiser, B.; Surendranath, Y.; Yano, J.; Yachandra, V. K.; Nocera, D. G. *J. Am. Chem. Soc.* **2012**, *134*, 6801–6809.
 “Structure–activity correlations in a nickel–borate oxygen evolution catalyst”

- (4) Roubelakis, M. M.; **Bediako, D. K.**; Dogutan, D. K.; Nocera, D. G. *Energy Environ. Sci.* **2012**, *5*, 7737–7740.
“Proton-coupled electron transfer kinetics for the hydrogen evolution reaction of hangman porphyrins”
- (3) Dogutan, D. K.; **Bediako, D. K.**; Teets, T. S.; Schwalbe, M.; Nocera, D. G. *Org. Lett.* **2010**, *12*, 1036–1039.
“Efficient microwave assisted synthesis of hangman porphyrins”
- (2) McNitt, K. A.; Parimal, K.; Share, A. I.; Fahrenbach, A. C.; Witlicki, E. H.; Pink, M.; **Bediako, D. K.**; Plaisier, C. L.; Le, N.; Heeringa, L. P.; Vander Griend, D. A.; Flood, A. H. *J. Am. Chem. Soc.* **2009**, *131*, 1305–1313.
“Reduction of a redox-active ligand drives switching in a Cu(I) pseudorotaxane by a bimolecular mechanism”
- (1) Vander Griend, D. A.; **Bediako, D. K.**; DeVries, M. J.; DeJong, N.A.; Heeringa, L. P.; *Inorg. Chem.* **2008**, *47*, 656–662.
“Detailed spectroscopic, thermodynamic and kinetic characterization of nickel(II) complexes with 2,2'-bipyridine and 1,10-phenanthroline attained via equilibrium-restricted factor analysis”

Oral Presentations

- (1) “Stepwise and Concerted Proton Coupled Electron Transfer During Water Oxidation at Cobalt-based Thin-Film Electrocatalysts” Gordon Research Seminar on Renewable Energy: Solar Fuels, Lucca (Barga), Italy, May 2012.
- (2) “Oxygen Evolution Mediated by a Nickel–Borate Thin-Film Electrocatalyst” American Chemical Society 242nd National Meeting, Denver, CO, USA, August 2011.
- (3) “Oxygen Evolution Mediated by a Nickel–Borate Thin-Film Electrocatalyst” Addressing Challenges in Solar Energy Utilization towards Water Splitting, International Symposium on Advancing the Chemical Sciences–Challenges in Renewable Energy (ISACS 4), Cambridge MA, USA, July 2011.

I am greatly indebted to all Nocera group members and MIT faculty members with whom I crossed paths at MIT over these past three and a half years. Each has played some role in shaping the person I am today. While some have certainly had a larger impact than others, none has influenced my way of thinking about chemistry more than my advisor, Dan Nocera. I am grateful for the freedom he has afforded me in exploring my own ideas and determining the direction of this project, while challenging me to think critically about my work within its broader context, so as to avoid the danger of focusing my work too narrowly at the expense of tackling the next big frontier in our field. I look forward to our continued interactions over the next couple of years.

I am also grateful to Professor Mircea Dincă for his guidance, both while he was a post-doc in the Nocera group and I had just joined the lab, and later as my thesis committee chair. Our meetings have always been stimulating, and he has provided a much-needed, fresh perspective on my research and ideas. I am also grateful to Professors Dick Schrock, Steve Lippard, and Kit Cummins for their enthusiasm for science, and their dedication to developing and teaching the excellent inorganic chemistry courses at MIT. I am also particularly thankful to them for their willingness to engage in informal conversations about all aspects of inorganic chemistry with graduate students like myself.

It is safe to say that of all the graduate students I interacted with over these last few years, Yogi has played the most significant role in my scientific development. I deeply appreciate his mentorship over the first year of this project, and his eagerness to listen and discuss ideas thereafter. I thoroughly enjoyed the many hours we spent discussing electrochemical minutiae in front of the blackboard at the cornucopia bay! I am grateful for his friendship, and I am sure he will do exceptionally well in his own scientific career.

To all other friends from the Nocera group, including, but not limited to Dilek, Tim Cook, Tom Teets, Mike Huynh, Matt, Danna, Danny, Changhoon, Andrew Ullman, Chris Lemon, Yi, Manos, Evan, Lisa, Christina, Bonjun, Casandra, Emily, Arturo, Dino, Elizabeth,

Bryce, Graham and Maher, I would like to say thank you very much for all the good times. For most of you, we shall continue to see each other until I graduate from Harvard, so I'll save a more personal "thank you" until then.

I am very grateful to Allison Kelsey and Janet MacLaughlin for their help in managing the affairs of our large group and ensuring that our research could proceed with little interruption. They served as an integral part of our group, and without them, so many logistical tasks would have been infinitely more difficult to accomplish.

My mom has been a constant source of wisdom for me, and her advice in challenging times has been invaluable. Somehow, she has managed to always, unfailingly, present herself as a wellspring of love and encouragement over the course of my graduate studies. My dear dad never got to see me attend MIT, but his life left an indelible mark on me during the first 22 years of my life that will never cease to impact me. I have found that it is supremely rare to find an intellectual of his stature, who is also so humble, selfless and exhibits so much love and compassion for others. His life—as a husband, father, and scholar—stands as an example to me, and one I shall endeavor to emulate. My brother, Yaw, was one of my earliest role models and I continue to look up to him to this day. I have deeply appreciated his counsel and encouragement over these years, and I could not have asked for a better brother.

None of this would have been possible without the unwavering support of my dear wife, Lisseth. Notwithstanding the demands of graduate school on my time, she has been more than understanding, and so much more supportive than I could have asked. She has always kept me grounded, and helped me to keep everything in the right perspective. On a more practical note, I think I would have become severely emaciated were it not for her resolve to take proper care of me. I cannot imagine my life without her and I so look forward to sharing the rest of it with her. Thank you.